Electronic Properties of Oxide and Semiconductor Heterostructures

A DISSERTATION
SUBMITTED TO THE FACULTY OF THE GRADUATE SCHOOL
OF THE UNIVERSITY OF MINNESOTA
BY

Michael Joseph Sammon

IN PARTIAL FULFILLMENT OF THE REQUIREMENTS
FOR THE DEGREE OF
Doctor of Philosophy

BORIS I. SHKLOVSKII

August, 2019

Acknowledgements

My time in graduate school has been the most difficult and rewarding time in my young life. I am confident to say that I would not have succeeded in my time here if it were not for the dedication and support of those around me.

I owe a tremendous debt to my advisor Boris Shklovskii. He has been a mentor to me both in science and in life. Though we have had our share of frustrations, his determination to my success as his student is the main reason for the completion of this thesis.

I must also thank the collaborators of the various chapters of this thesis. Chapter 2 was a collaboration with Michael Zudov. He has provided much insight into the mind of an experimental physicist. I must also thank Tianran Chen, with whom the numerical simulations of Chapter 2 were conducted. Chapters 3, 4, and 5 were done in collaboration with Han Fu, who taught me much in my first years in graduate school. I must also thank my friend and office mate Xuzhe Ying who has tolerated my endless questions. Our conversations aided me much throughout the years.

Finally I must thank my family and friends for their support over the years. I must especially thank my girlfriend Kabao Vang for always giving me something to look forward to at the end of my day.

Abstract

The modern world's dependency on electronics provides a constant need to discover new materials and devices. A promising technique to fabricate a new device is to create a heterostructure; a device consisting of two bulk crystals joined at an interface. These materials often support a low dimensional electron gas confined to the interface, which exhibits properties different than both the parent materials. These materials have led to the creation of MOSfets, the discovery of the quantum Hall effect, and in recent years the discovery of Majorana edge modes in nanowires.

In this thesis, we study several different heterostructures. We begin with one of the most famous heterostructures, AlGaAs/GaAs. Modern AlGaAs/GaAs heterostructures support a high mobility two-dimensional electron gas (2DEG) in a quantum well. The 2DEG is provided by two remote donor δ-layers placed on both sides of the well. Each δ-layer is located in the midplane of a narrow GaAs well, flanked by narrow AlAs layers which capture excess electrons from donors. We show that each excess electron is localized in a compact dipole atom with the nearest donor. The excess electrons screen both the remote donors and background impurities, and are responsible for the observed high mobility. Still, we find that the mobility is substantially lower than theoretical estimates, which may be due to significant disorder in the donor layers, most likely roughness of the interfaces or spreading of the donors out of the midplane of the layer. Thus one should take care to make sure that the donor layers are as ideal as possible.

We next move on to oxide heterostructures involving $SrTiO_3$ (STO). More specifically, we study the electron gas in accumulation layers of these heterostructures characterized by a density profile $n(x)$, where x is the distance from the STO surface. $SrTiO_3$ at liquid helium temperatures has the highest dielectric constant which strongly enhances the role of nonlinear dielectric effects. It was recently shown that the nonlinear dielectric response results in an electron density profile $n(x)$ that slowly decays as $1/x^{12/7}$. We show that such a long tail of $n(x)$ causes the magnetization and the specific heat of the accumulation layer to diverge at large x. We explore the truncation of the tail by the finite sample width W, the transition from the nonlinear to linear

dielectric response with dielectric constant κ, and the use of a back gate with a negative voltage $-|V|$. We find that as a result both the magnetization and specific heat are anomalously large and obey nontrivial power law dependences on W, κ, or $|V|$.

In the linear dielectric regime under a strong magnetic field, the large dielectric constant of STO makes it easy to reach a quasi-one-dimensional state known as the extreme quantum limit (EQL) in which all electrons occupy the lowest Landau level. We present a theory of the EQL phase in STO accumulation layers. We find a phase diagram of the electron gas in the plane of the magnetic field strength and the electron surface concentration for different orientations of the magnetic field. In addition to the quasi-classical metallic phase (M), there is a metallic EQL phase, as well as an insulating Wigner crystal state (WC). Remarkably, the insulating Wigner crystal phase depends on the orientation of the magnetic field. We show that these effects can be measured through quantum capacitance measurements of the STO accumulation layer.

The third material we study is semiconducting quantum wires. Though it is not a heterostructure, it supports a low dimensional electron gas which is often tuned with an external gate, making it similar to many of the devices we have studied. We have theoretically investigated the influence of interface roughness scattering on the low temperature mobility of electrons in quantum wires when electrons fill one or many subbands. We find the Drude conductance of the wire as a function of the linear concentration η has a sharp peak. The height of this peak grows as a large power of the wire radius R, so that at large R the conductance G_{max} exceeds e^2/h and a window of concentrations with delocalized states (which we call the metallic window) opens around the peak. Thus, we predict an insulator-metal-insulator transition with increasing concentration for large enough R. Furthermore, we show that the metallic domain can be sub-divided into three smaller domains: 1) single-subband ballistic conductor, 2) many-subband ballistic conductor 3) diffusive metal, and use our results to estimate the conductance in these domains. Finally we estimate the critical value of $R_c(\mathcal{L})$ at which the metallic window opens for a given length $\mathcal{L}$.

We conclude the thesis with a discussion of a newer class of materials known as transition metal dichalcogenides (TMDs). We study a capacitor made of three monolayers TMD separated by hexagonal boron nitride (hBN). We assume that the structure

is symmetric with respect to the central layer plane. The symmetry includes the contacts: if the central layer is contacted by the negative electrode, both external layers are contacted by the positive one. As a result a strong enough voltage V induces electron-hole dipoles (indirect excitons) pointing towards one of the external layers. Antiparallel dipoles attract each other at large distances. Thus, the dipoles alternate in the central plane forming a 2D antiferroelectric with negative binding energy per dipole. The charging of a three-layer device is a first order transition, and we show that if V_1 is the critical voltage required to create a single electron-hole pair and charge this capacitor by e, the macroscopic charge $Q_c = eSn_c$ (S is the device area) enters the three-layer capacitor at a smaller critical voltage $V_c < V_1$. In other words, the differential capacitance $C(V)$ is infinite at $V = V_c$. We also show that in a contact-less three-layer device, where the chemically different central layer has lower conduction and valence bands, optical excitation creates indirect excitons which attract each other, and therefore form antiferroelectric exciton droplets. Thus, the indirect exciton luminescence is red shifted compared to a two-layer device.

Contents

List of Tables

List of Figures

Chapter 1

Introduction

1.1 Excess Electron Screening in modern AlGaAs/GaAs heterostructures

We begin our discussion with one of the most well known heterostructures: the AlGaAs/GaAs heterostructure. Modern $Al_xGa_{1-x}As$/GaAs heterostructures with an ultra-high mobility two-dimensional electron gas (2DEG) are the result of spectacular progress in molecular beam epitaxy[1, 2, 3, 4, 5, 6, 7, 8, 9]. An increase of the electron mobility by nearly 4 orders of magnitude over the last several decades lead to important discoveries, including odd- and even- denominator fractional quantum Hall effects and stripe and bubble phases[10, 11, 12, 13, 14].

The modern $Al_xGa_{1-x}As$/GaAs heterostructure under consideration is schematically shown in Fig. 1.1(a). It consists of a GaAs quantum well of width $w = 30$ nm, which supports a 2DEG with a typical concentration $n_e \simeq 3 \times 10^{11}$ cm^{-2}. The 2DEG is provided to this well by two remote donor layers symmetrically positioned at distances $d \simeq 70 - 85$ nm from the edge of the well. It has a low-temperature mobility $\mu \simeq 3 \times 10^7$ cm^{2}V^{-1}s^{-1} and a quantum mobility $\mu_q \equiv e\tau_q/m^\star \sim 1 \times 10^6$ cm^{2}V^{-1}s^{-1},[5, 15, 16, 17] where τ_q is the quantum lifetime and $m^\star \approx 0.067m_e$ is the electron effective mass in GaAs. The quantum mobility governs the amplitude of low-field quantum oscillations, which increases exponentially with μ_q[18, 19, 20, 21].

The donor layers in modern devices have a sophisticated design which substantially

reduces electron scattering[6, 7]. As shown in Fig. 1.1(b), each remote donor layer consists of a narrow 3 nm GaAs quantum well, which is doped in the middle by a δ-layer of Si donors with a typical concentration $n \sim 10^{12}$ cm^{-2}. This layer is surrounded by two AlAs layers of width of 2 nm. Because the donor concentration n is significantly larger than the 2DEG concentration, a large fraction fn of excess electrons remain in the donor layer, where f is the filling fraction of excess electrons in a single donor layer. For these widths of the AlAs and GaAs layers, these excess electrons are stored in the AlAs side wells because the relevant effective mass in AlAs is much larger than in GaAs[22]. Each excess electron pairs with a donor in a compact dipole atom and is localized (see Fig. 1.1(b)), so that its low-temperature parallel-to-2DEG conductance is activated[23]. Furthermore, the excess electrons hop between donors, minimizing their Coulomb energy; this leads to significant correlations in the positions of charged donors [24, 25, 26].

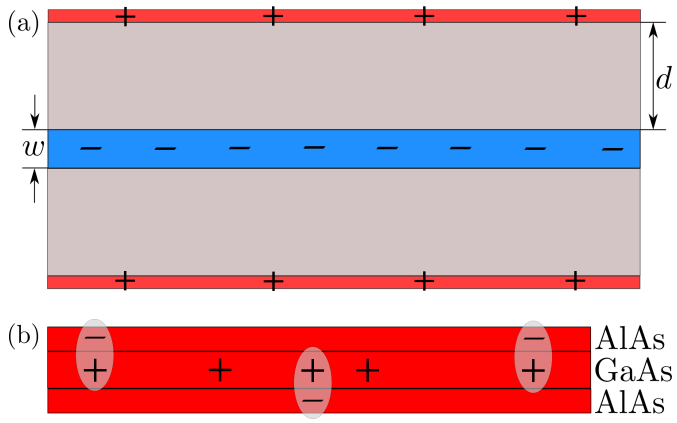

Figure 1.1: (Color online) (a) A schematic view of a modern $Al_xGa_{1-x}As$/GaAs heterostructure. The 2DEG (shown in blue) resides in a GaAs well of thickness w and is provided by two remote donor layers (shown in red) separated by $Al_xGa_{1-x}As$ barriers of thickness d (shown in gray). Here, $-$ and $+$ represent negative and positive charges in the 2DEG and the remote donor layers, respectively. (b) An enlarged view of a small section of the remote donor layer at a filling fraction $f \simeq 0.6$. Excess electrons $(-)$ in AlAs form compact dipoles (ellipses) with the nearest donors $(+)$ in GaAs. Empty donors (also shown by $+$) alternate with compact dipoles due to Coulomb repulsion between the excess electrons. Only empty donors are shown in Fig. 1(a).

In Ch.2 we investigate the correlations of these charged donors, which we call excess electron screening (EES), and summarize its effect on the scattering of the 2DEG electrons by charged impurities in the device. Let us first consider the scattering of the remote impurities (RI) with concentration n. For simplicity we focus on scattering by a single remote donor layer. We find that the RI mobilities can be written as

$$\mu_R = F(f)\frac{e}{\hbar}k_F^3 d_w^5, \tag{1.1}$$

$$\mu_{q,R} = F_q(f)\frac{e}{\hbar}k_F d_w^3, \tag{1.2}$$

where $k_F = (2\pi n_e)^{1/2}$ is the Fermi wavenumber of the 2DEG, and the subscript R refers to the RI scattering. The dimensionless mobilities $F(f)$ and $F_q(f)$ account for the effects of EES. Their asymptotic expressions at $f \ll 1$ and $1-f \ll 1$ are

$$F(f) = \begin{cases} 24f^3 & f \ll 1 \\ 7.7(1-f)^{-1} & 1-f \ll 1, \end{cases} \tag{1.3}$$

$$F_q(f) = \begin{cases} 24f^3 & f \ll 1 \\ 6.5(1-f)^{-1} & 1-f \ll 1. \end{cases} \tag{1.4}$$

Let us consider Eqs. (1.3) and (1.4) at $f \ll 1$, so that the concentration of excess electrons is small relative the total concentration of donors. In this limit, the excess electrons act as an independent electron gas which screens the fluctuations of the uncorrelated random donors with a screening radius r_s. Here we find that EES enhances both μ_R and $\mu_{q,R}$ by the factor $(d_w/r_s)^2$, where $d_w = d + w/2$ is the distance between the midplane of the 2DEG and the remote donor layer. We calculate r_s in this asymptotic limit $f \ll 1$, and find

$$r_s \simeq \frac{0.18}{n^{1/2} f^{3/2}}\,. \tag{1.5}$$

As a result, both μ_R and $\mu_{q,R}$ increase very strongly as f^3. It is worth noting that $F(f) \simeq F_q(f)$ for all f, indicating that the main difference between μ_R and $\mu_{q,R}$ is determined by the $(k_F d_w)^2$ difference of the prefactors in Eqs. (1.1) and (1.2).

Our analytic results for the RI limited mobilities are verified by numerical calculations[27]. We find that EES can enhance these mobilities by more than three orders of magnitude above their values in the absence of EES. However, in experiment we rarely see values

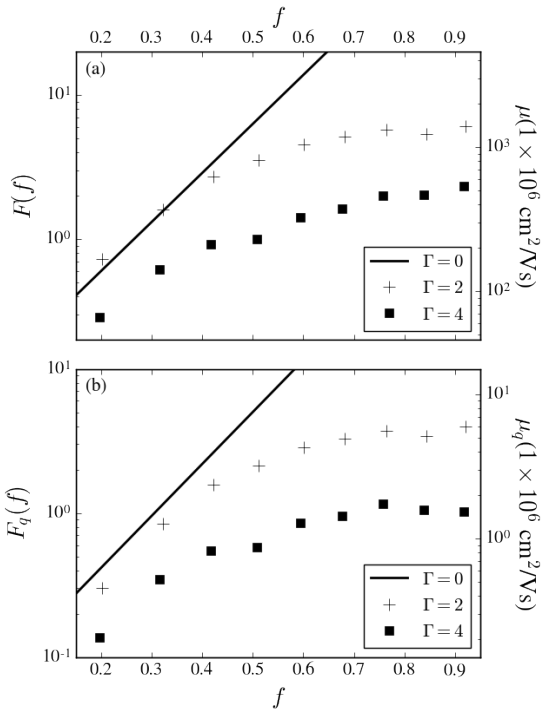

Figure 1.2: The universal functions $F(f)$ and $F_q(f)$ obtained from numerical simulations in the presence of additional Gaussian disorder in the energy levels of donors of width Γ are shown for $\Gamma = 2$ and $\Gamma = 4$ in units of $e^2 n^{1/2}/\kappa$. The best fit lines for $\Gamma = 0$ are given by the solid lines. Corresponding values of μ and μ_q are shown on the right vertical axis for a typical sample.

this large. One potential reason is that EES can be limited by additional disorder in the SPSL layer beyond the random positions of donors. Additional disorder (such as roughness of the AlAs/GaAs interface and spreading of the donors out of the midplane of the GaAs well) can suppress the density of states and weaken the EES. This leads to a saturation of the mobilities as a function of the filling fraction f, as shown in Fig. 1.2. If one wants to see record values of the mobilities (especially the quantum mobility), they should take care to reduce Γ.

Another possible reason that the mobilities do not reach the theoretical limit is that they can be limited by the background impurities[23]. The second half of Ch. 2 is devoted to the discussion of the background impurity scattering in the presence of EES. We arrive at the conclusion that the impurities nearest to the 2DEG which determine

the mobilities are unaffected by EES. Thus to improve the mobilities one should work hard to eliminate them.

1.2 Thermodynamic Properties of $SrTiO_3$ Accumulation Layers

The next type of heterostructures studied are the oxide based heterostructures made from the ABO_3 perovskites. We focus on the heterostructures involving $SrTiO_3$ (STO), which is a semiconductor with a band gap $E_g \simeq 3.2$ eV and a large dielectric constant $\kappa = 2 \cdot 10^4$ at liquid helium temperatures[28]. These heterostructures support a 2DEG with a reasonably large mobility, and exhibit a number of interesting properties including superconductivity, ferromagnetism, and multiferroicity[29, 30]. The origin of these effects is still unclear, and necessitates a deeper understanding of its electronic structure.

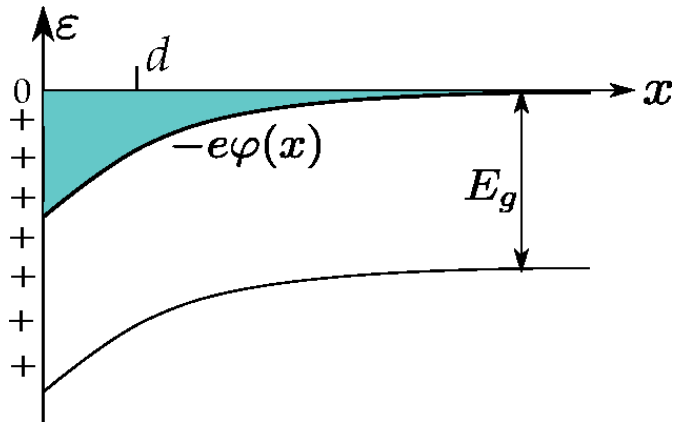

Figure 1.3: (Color online) Schematic electron potential energy $-e\varphi(x)$ diagram of an accumulation layer in a moderately n-doped STO where x is the distance from the surface. The electron (blue) is attracted by the positive charges (pluses) at $x = 0$. The characteristic width of the gas is d. In the bulk of STO the Fermi level ε_F is near the bottom of the conduction band.

Our focus is directed at the properties of the accumulation layer formed at the STO heterostructure interface. As an example we consider the $GdTiO_3/SrTiO_3$ (GTO/STO) heterostructure, where the accumulation layer is induced by the electric field resulting from the "polar catastrophe" (see Fig. 1.3)[31]. The role of GTO can also be played by

other perovskites such as $LaAlO_3$ [29, 30, 32], $NdAlO_3$, $LaVO_3$ [33], $SmTiO_3$, $PrAlO_3$, $NdGaO_3$ [34], $LaGaO_3$ [35], and $LaTiO_3$ [36]. Another possible example is the use of ionic liquid gating, which allows one to accumulate up to 10^{14} cm^{-2} electrons on the surface of STO[37, 38, 39, 40, 41]. Regardless of the origin, we can imagine that the effect of the gate or polar catastrophe is to bring a concentration N of positive charge that lies at the STO surface. This charge attracts electrons to the surface, creating the accumulation layer illustrated in Fig. 1.3.

The properties of accumulation layers in STO based heterostructures are significantly altered at liquid helium temperatures due to the large dielectric constant. In Ref. [42], the authors calculated the three-dimensional (3D) electron density profile $n(x)$ of the accumulation layer with a large 2D density N as a function of the distance x from the surface. To account for the nonlinear dielectric response in STO they used the Landau-Ginzburg free energy expansion [43, 44] while describing the degenerate electron gas with the Thomas-Fermi approximation[45]. They found that the electron density profile decays as

$$n(x) \propto (x+d)^{-12/7}, \tag{1.6}$$

illustrated by the shaded region in Fig. 1.3. The characteristic length d decreases with increasing density N as $d \propto N^{-7/5}$.

The slow decay of the density profile in samples whose mobility is limited by scattering at the heterostructure interface leads to a divergence of the mobility, Hall factor, magnetoresistance, and thermopower[46]. Such a tail was called the "run-away tail"(RAT)[46]. These divergences are truncated by some mechanism which results in a large but finite value of the kinetic coefficients. In Ch. 3 we study the thermodynamic properties of the RAT. We show that similar to the kinetic coefficients, both the magnetization and the specific heat of the RAT are anomalously large[47]. Indeed, it is well known that both the magnetization and the specific heat are proportional to the density of states

$$g(n) = \frac{m^*}{\pi^2\hbar^2}(3\pi^2 n)^{1/3}. \tag{1.7}$$

In each quantity, the spatial dependence is determined entirely by the density of states, i.e. both the magnetization and the specific heat go as $n(x)^{1/3} \propto (x+d)^{-4/7}$. When averaged over the accumulation layer with $n(x)$ given by Eq. (1.6), both these quantities

diverge, and must be truncated at some large $x = L$, where we have introduced the truncation length L. As a result, we can write the magnetization as

$$M_s(L) = C_4 \tilde{M}_s \left(\frac{L}{d}\right)^{3/7}, \tag{1.8}$$

where $\tilde{M}_s$ is the magnetization in a surface layer of size d and C_4 is a numerical constant. Similar expressions can be written for the specific heat. We see from Eq. (1.8) that the magnetization is strongly enhanced by the ratio of the cutoff length L to the accumulation length d, which can be very large. Indeed, if we consider the truncation by the sample length $W \sim 1000$ nm for an accumulation layer of size $d \sim 1$ nm, the magnetization is enhanced above its surface value by nearly 20 times. We explore several possible mechanisms for the truncation in detail in Ch. 3.

The remaining part of Ch. 3 describes the capacitor formed between the accumulation layer and a back gate located at the $x = W$ edge of the sample. At large voltage V the electrons are confined to a region of thickness L_V as measured from the $x = 0$ surface, leaving a fully depleted region of size $W - L_V$ near the back gate, where $L_V \propto |V|^{7/15}$ is the back gate truncation length. We show that the inverse capacitance in this limit has a positive correction term

$$C^{-1}(V) \propto \frac{L_V}{\kappa(V)}, \tag{1.9}$$

where

$$\kappa(V) \propto |V|^{-2/3} \tag{1.10}$$

is the effective dielectric constant when the accumulation layer is fully depleted. What is surprising is that the correction is positive, leading to an effective width larger than the width of the sample. We explain the origin of this bizarre phenomenon in Ch. 3.

1.3 Extreme Quantum Limit in $SrTiO_3$ Accumulation Layers

We continue with our discussion of the exotic properties of the accumulation layers formed in heterostructures involving $SrTiO_3$ at liquid helium where the dielectric constant is $\kappa = 2 \times 10^4$. Here we consider accumulation layers with lower density in which the dielectric response is linear. We consider the structure of the accumulation layer

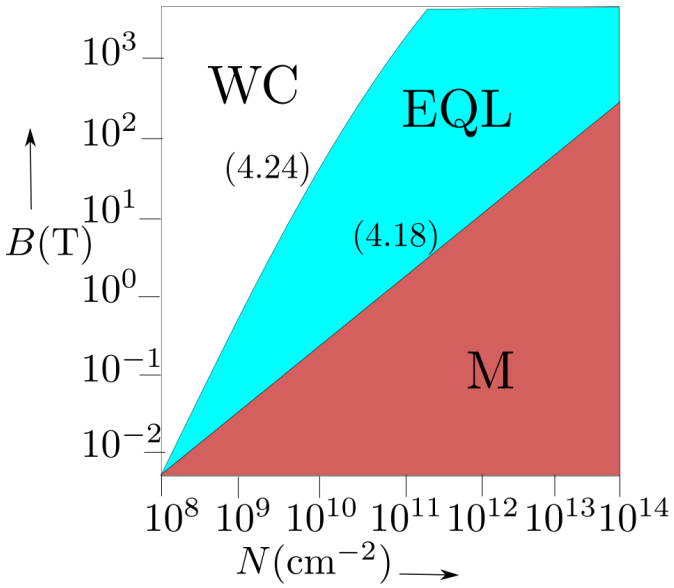

Figure 1.4: Phase diagram for $\boldsymbol{B} \perp \boldsymbol{E}$ in STO at liquid helium temperatures. The axes are $B(\mathrm{T})$ and $N(\mathrm{cm}^{-2})$ and the diagram is presented in a log-log scale. The regions are the quasi-classical metal (M), the metallic EQL phase (EQL), and the insulating Wigner crystal state (WC).

under the application of a strong external magnetic field B and at low temperatures T. Particularly, when the external field B is so strong such that

$$\hbar\omega_c \gg E_F \gg k_B T, \frac{e^2 n^{1/3}}{\kappa}. \tag{1.11}$$

Here $\omega_c = eB/m^*c$ is the cyclotron frequency, m^* is the effective mass, $E_F \approx \hbar^2 n^{2/3}/2m^*$ is the Fermi energy at $B = 0$, $k_B T$ is the thermal energy, κ is the dielectric constant, and n is the three dimensional concentration of electrons. When Eq. (4.1) is satisfied and the cyclotron energy becomes the dominant energy scale in the system., we say that the system is in the "extreme quantum limit" (EQL).

Before we discuss properties of the EQL, let us rephrase the conditions under which it can be reached, simultaneously explaining why STO is an ideal system to study this phase. From Eq. (4.1), it follows that in order for the gas to remain metallic, one must have $na_B^3 \gg 1$. Here $a_B = \kappa\hbar^2/m^*e^2$ is the effective Bohr radius of the material. In addition to the metallic condition, the strong magnetic field condition, $\hbar\omega_c \gg E_F$, requires $n\lambda^3 \ll 1$, where we have introduced $\lambda = \sqrt{\hbar c/eB}$ as the magnetic length.

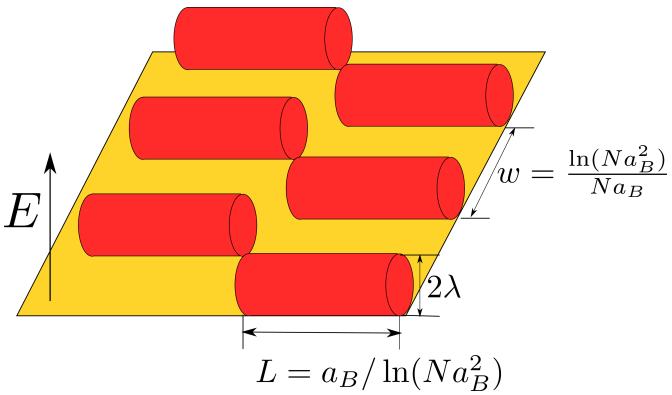

Figure 1.5: (Color Online) Schematic of the electron structure in the WC phase for $\mathbf{B} \perp \mathbf{E}$. Each electron (red/dark grey) forms a cylinder of radius λ oriented along the direction of the magnetic field on the surface (yellow/light grey) inside the semiconductor.

Combining $na_B^3 \gg 1$ and $n\lambda^3 \ll 1$, we find that in order to reach the EQL, we require $\lambda \ll a_B$. Due to the large dielectric constant, STO has the largest effective Bohr radius. Indeed, assuming the isotropic mass of $m^* = 1.5m_e$ we find $a_B = 700$ nm in STO. This allows the EQL to be reached at $B \simeq 10^{-3}$ T, making STO an ideal candidate to study the EQL.

In Ch. 4 we study the EQL phase of STO accumulation layers[48]. Our results are summarized in Fig. 1.4 as a phase diagram of the magnetic field B vs. the total 2 dimensional electron concentration N. We consider concentrations $N < 10^{14}$ cm^{-2}, so that the dielectric response remains linear. Fig. 1.4 assumes that the magnetic field B is applied perpendicular to the surface electric field E which creates the accumulation layer.The diagram consists of 3 phases. The first phase is the quasi-classical metal phase (region M), which occurs at small magnetic fields. In this phase, the density profile $n(x)$ is unaltered by the magnetic field, and obeys the well known Frenkel distribution in which $n(x) \propto (x + d_0)^{-6}$[49], where x is the distance from the heterostructure interface and $d_0 \propto N^{-1/5}$ is the characteristic length of the accumulation layer in the linear dielectric regime. When the magnetic field is sufficiently strong, the kinetic energy in the direction perpendicular to the field is quantized and electrons occupy the lowest Landau level so that we reach the EQL. This alters the density profile to be

$$n(x) \propto (x - d_\lambda)^2, \tag{1.12}$$

where the cutoff length

$$d_\lambda = C_6(Na_B\lambda^4)^{1/3}, \tag{1.13}$$

and $C_6 =\simeq 8.23$ is a numerical coefficient. The cutoff length d_λ is magnetic field dependent and shrinks with the magnetic field. Indeed, while the density of electrons in the plane perpendicular to the magnetic field is fixed at the Landau level density $1/(2\pi\lambda^2)$, the remaining direction acts as a free electron gas. This electron gas is quantized into 1D subbands, the number of which decreases with increasing magnetic field. At a large enough magnetic field, the electrons are confined into a single subband and the system enters an insulating Wigner crystal phase, illustrated in Figs 1.5.

The effects of the EQL on the accumulation layer can most easily be observed through measurements of the quantum capacitance. We consider the capacitor formed between an STO accumulation layer and a metallic gate, separated by an insulating barrier. We assume for simplicity that the metallic gate is used to create the accumulation layer. We show in Ch. 4 that the accumulation layer increases the thickness of the capacitor by a small amount d_q beyond the geometrical thickness. This extra distance can be thought of a second capacitor in series with the geometrical capacitor, and is commonly referred to as the "quantum capacitance". The thickness d_q is proportional to the characteristic length of the accumulation layer, and thus can be used as a direct probe of its electronic structure.

1.4 Surface Roughness Scattering in Quantum Wells and Semiconducting Nanowires

The next low dimensional systems studied in this thesis are the semiconductor nanowires made from InAs and InSb. They support a low dimensional electron gas and thus are similar to the devices we have already discussed. In recent years these nanowires have attracted lots of attention due to their potential applications, such as field-effect transistors, elementary logic circuits, resonant tunneling diodes, light-emitting diodes, lasers, and biochemical sensors [50, 51]. Advances in the nanowire growth have also led to the development of novel quantum devices [52, 53, 54, 55, 56]. They allow the exploration of mesoscopic transport in a highly confined system. Recently, hybrid superconductor-semiconductor nanowire devices have been identified [57, 58] as a platform to study

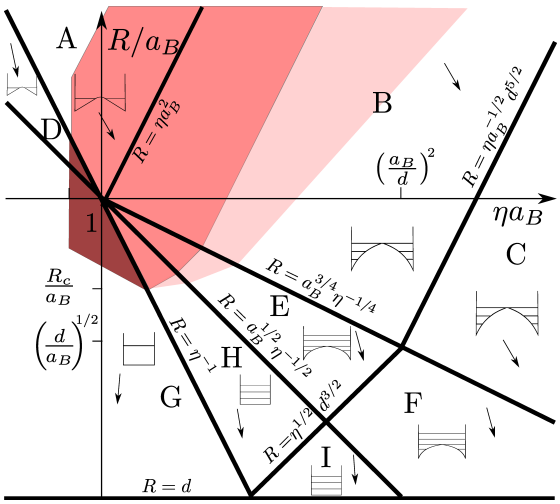

Figure 1.6: The scaling "phase diagram" of roughness limited electron Drude mobility of a long quantum wire plotted as a function of radius R and linear electron concentration η for $d < a_B$ in the log-log scale. Different "phases" or regions are denoted by capital letters. Drude mobility expressions corresponding to these regions are given in Tab. 1.1. Region boundaries are given by the equations next to them. The schematic self-consistent electron potential energy profile along the wire diameter is shown for each region. Small arrows show the direction of mobility decrease in each region. The dark red, light red, and pink regions correspond to the single-subband ballistic conductor, many-subband ballistic conductor, and diffusive metal regions for $R_c(\mathcal{L}) < a_B$. Electrons are localized in all the colorless regions.

Majorana end modes [59], which exhibit topological properties [60, 61, 62]. To further improve this topological system, a reduction of the disorder in the nanowire is essential [63, 64].

In many of these devices, the scattering of electrons on surface roughness is the leading type of disorder[65, 66, 67, 68, 69, 70]. In Ch. 5 we develop a theory of roughness scattering limited mobility of nanowires as a function of their radius R and linear electron concentration η controlled by a back gate, filling a much needed gap in the literature[71, 72, 73]. We study a model of roughness in which the roughness consists of local atomic defects at the wire surface. These defects can be thought of as small islands or ditches on the surface of the nanowire, of characteristic diameter d and height $\Delta \sim a$, where a is the lattice constant. The small shift in the wire radius introduces fluctuations in the kinetic energy of the electron which induces scattering. This model

Table 1.1: Mobility μ in units of $(e/\hbar)\left(d^4/\Delta^2\right)$ as a function of the linear electron concentration η at $d < a_B$ for different regions.

A	B	C
$a_B^2 R^2/\eta^2 d^6$	$a_B^{8/5} R^{11/5}/d^6 \eta^{11/5}$	$a_B R/\eta d^3$
D	E	F
$a_B^2 R^3/\eta d^6$	$a_B^{1/2} R^{11/3}/\eta^{11/6} d^6$	$a_B^{1/2} R^{5/3}/\eta^{5/6} d^3$
G	H	I
$R^7 \eta/d^6$	$R^{14/3}/\eta^{4/3} d^6$	$R^{8/3}/\eta^{1/3} d^3$

was used to study the roughness limited mobility in quantum wells of width L and 2D concentration N.

We use a scaling theory to find the roughness limited Drude mobility for a wire of radius R and linear concentration of electrons η [74]. Our results are determined by the four dimensionless lengths Δ, d, η^{-1}, and R all in units of the effective Bohr radius $a_B = \kappa\hbar^2/m^* e^2$. We find that depending on these 4 lengths, there are several different functional forms of the Drude limited mobility, leading a complex and rich phase diagram shown in Fig. 1.6. The corresponding values of the Drude mobility are given in Ch. 5. There are three colored regions of Fig. 1.6 (dark red, light red, and pink), which illustrate the regions in which the semiconducting wire of length $\mathcal{L} \sim 1$ μm is metallic. Most important is the dark red region which represents the single subband ballistic regime necessary for the observation of the Majorana zero modes.

The theory of the roughness limited Drude mobility of the semiconducting nanowire and the quantum well has a distinct difference. It was previously shown that despite conjectures, there is no reentrant metal-insulator transition with growing electron concentration in quantum wells limited by surface roughness scattering[75, 76]. The situation is quite different in nanowires, mainly due to the 1D nature of the wire which strongly enhances localization effects[77, 78]. As shown in Fig. 1.6, for certain values of R and $\mathcal{L}$ the wire conductance G tends to decrease at large concentrations. This leads to the possibility that $G < (e^2/h)$ at large concentrations, similar to the metal-insulator transition proposed for the quantum wells[76]. Of course, if the wire radius is too small it is also possible that the wire is always insulating. Thus there is a critical radius $R_c(\mathcal{L})$

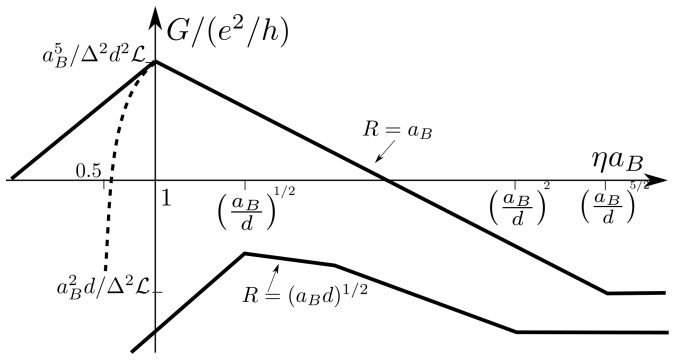

Figure 1.7: The scaling behavior of the dimensionless Drude conductance of a quantum wire with length $\mathcal{L}$ and radius R as a function of the linear electron concentration η at different wire radii for $d \ll a_B$ in the log-log scale (full lines). The upper curve corresponds to $R = a_B$ and the lower one is $R = (a_B d)^{1/2}$. They are obtained from cross-sections of the "phase diagram" in Fig. 1.6 and the mobilities in Tab. 1.1. The dashed line on the upper curve shows the metal-insulator crossover near $\eta a_B = 0.5$ induced by electron-electron interactions. We see that for $R = a_B$ the metallic window is open, while for $R = (a_B d)^{1/2}$ the window is closed. $\mathcal{L} = a_B^{7/2}\Delta^{-2}d^{-1/2}$ was chosen.

at which a "metallic window" is open and the insulator-metal-insulator transition can be observed. For a wire with $R \leq a_B$, we find

$$R_c(\mathcal{L}) = (\Delta^2 d^2 \mathcal{L})^{1/5}. \tag{1.14}$$

The metallic window is illustrated in Fig. 1.7 by regions in which the dimensionless conductance $G/(e^2/h) > 1$.

1.5 Attractive Interaction of Interlayer excitons in Transition Metal Dichalcogenide heterostructures

In the last chapter, we discuss a newer type of semiconductors: transition metal dichalcogenides (TMDs). Ever since the exfoliation of graphene single layer films[79], there has been an explosion of interest in isolating similar flakes of Van der Waal materials[80, 81, 82, 83, 84, 85, 86]. Particular interest has been paid to the 2D exciton properties of flakes of the semiconducting TMDs MoS_2, $MoSe_2$, WS_2, and WSe_2, where the 2D nature of the materials and the large effective mass results in exciton binding energies

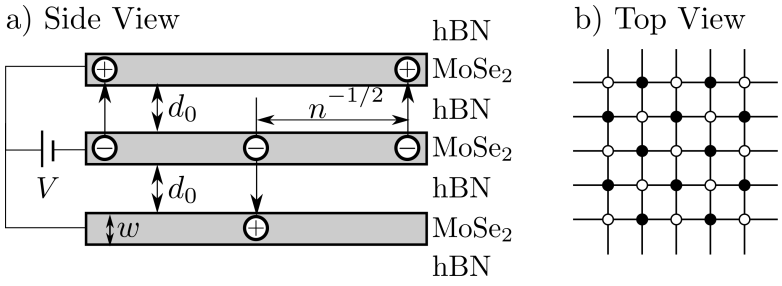

Figure 1.8: a) Cross section of a capacitor made of three $MoSe_2$ monolayers of width w shown in gray. Each spacer of width d_0 has the same number of hBN layers, which are labeled. The outer top and bottom layers are covered by hBN as well. The capacitor charges via the creation of alternating up and down pointing electron-hole dipoles (indirect excitons) shown by arrows. The electrons in the central plane form a square lattice with a lattice constant $n^{-1/2}$. b) Top view of the square lattice of alternating dipoles. White (black) circles correspond to dipoles whose orientation points up (down). Each orientation forms its own square sublattice.

~ 100 meV[87, 88]. Heterostructures of TMDs provide an additional platform of control over the excitonic properties. It has been shown[88, 89] that in bilayer $MoSe_2/WSe_2$ structures under illumination, the type II band alignment of the $MoSe_2$ and WSe_2 monolayers allows the formation of indirect excitons, in which an electron in $MoSe_2$ binds to a hole in WSe_2. Because of the weak overlap of the electron and hole wavefunctions, these excitons have very large lifetimes compared to their intralayer counterparts[88]. In addition, the separation of the electron and hole creates a large out of plane dipole moment which allows the binding energy of these excitons to be tuned with an external gate, making them an ideal platform for research and potential applications[90, 87, 89, 91].

In the final chapter of this thesis, we study the capacitance of a device consisting of three identical monolayers of intrinsic TMD (such as $MoSe_2$) each of width w, separated by the same number of hBN layers of total width d_0 on each side, so that the structure is symmetric with respect to the central layer midplane (see Fig. 1.8 a))[92]. Such a device acts similar to indirect excitons in trilayer TMD heterostructures such as $WSe_2/MoSe_2/WSe_2$. In either case, we can imagine a three layer device in which the central layer has a concentration n of electrons while each of the outer layers has a concentration $n/2$ of holes. Correspondingly, an equal number of interlayer excitons, each with a dipole moment $ed = e(d_0+w)$, are directed from the central plane to the top

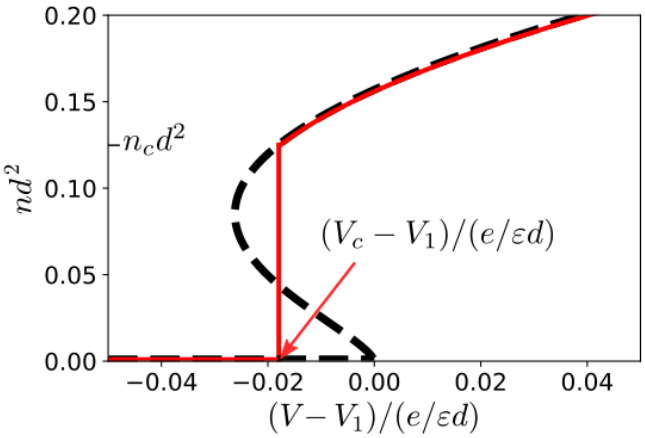

Figure 1.9: The dimensionless density nd^2 as a function of dimensionless voltage $(V - V_1)/(e/\varepsilon d)$ for the three-layer device shown in Fig. 1.8. The dashed curve shows the curve $n(V)$ obtained from Eq. (6.9), while the solid red curve shows the equilibrium $n(V)$ curve obtained using Maxwell's rule. We see that in equilibrium, the density jumps to a value n_c at the critical voltage V_c. Thus the capacitor charge experiences a first order phase transition with growing V.

and to the bottom (see Fig. 1.8a). At large distances along the plane, two antiparallel dipoles attract each other, while at distances smaller than d they repel each other. It is natural to assume that as a result the dipoles form a two-dimensional antiferroelectric square lattice. This lattice is similar to NaCl, where Na-like and Cl-like sites are occupied by up and down pointing dipoles, i.e. all nearest neighbor dipoles are antiparallel (see Fig. 1.8b)). Electrons of the central plane form a square lattice with the lattice constant $n^{-1/2}$.

In the 3 layer capacitor, the attraction between indirect excitons in the device causes a first order phase transition at low temperatures when the applied voltage V grows (see Fig. 1.9). While at small V there are no dipoles and the capacitor remains uncharged, at some critical value $V = V_c < V_1$ the whole lattice of alternating dipoles emerges. This means that a macroscopic charge $Q_c = eSn_c$, where $n_c = 0.13d^{-2}$ and S is the device area, enters this capacitor. Thus, the differential capacitance

$$C^{-1} = \frac{1}{(eS)^2}\frac{d^2E}{dn^2}, \tag{1.15}$$

of the system with energy E and area S has a δ-peak at the critical voltage $V = V_c$.

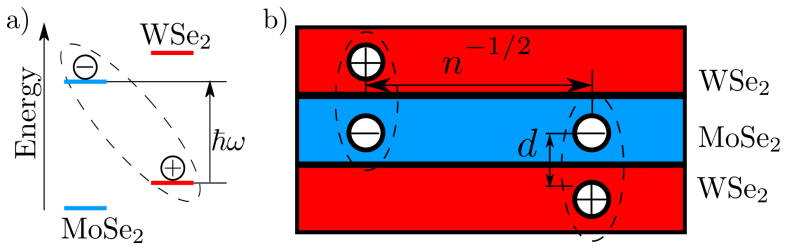

Figure 1.10: a) Band alignment in $MoSe_2/WSe_2$ bilayer. b) Schematic of a trilayer $WSe_2/MoSe_2/WSe_2$ device for optical studies of spatially interacting indirect excitons. When the device is illuminated at low temperatures, the type II band alignment of neighboring $WSe_2/MoSe_2$ monolayers (see inset) allows the formation of indirect excitons consisting of an electron in $MoSe_2$ and a hole in WSe_2. Excitons of opposite polarity attract each other and form a crystal with alternating dipoles.

This result is summarized in Fig. 1.9 as a plot of the density nd^2 as a function of the voltage $(V - V_1)/(e/\varepsilon d)$. Here we have used the definition of the voltage as

$$V = \frac{1}{eS}\frac{dE}{dn}, \tag{1.16}$$

while V_1 is the threshold voltage required to create a single isolated electron-hole pair in an intrinsic semiconductor. The dashed curve is obtained from Eq. (1.16). Most noticeable is that there is a range in which there are three densities for each voltage: a lower branch along $n = 0$, a middle branch, and an upper branch. Within the middle branch, the capacitance defined by Eq. (1.15) is negative and this region is thermodynamically unstable and is inaccessible. In an experiment, we do not expect the density to change continuously along the dashed curve, but instead along the curve shown in red where the density jumps to a value

$$n_c = 0.13d^{-2}, \tag{1.17}$$

at a critical voltage

$$V_c = V_1 - 0.018\frac{e}{\varepsilon d}. \tag{1.18}$$

As the density abruptly jumps, there is a δ-peak in the capacitance at $V = V_c$. For $V \geq V_c$ we can write the capacitance as

$$C(V) = eSn_c\delta(V - V_c) + C_u(V), \tag{1.19}$$

where the non-singular capacitance $C_u(V)$ is obtained by differentiating the upper branch of the $n(V)$ curve shown in Fig. 1.9 with respect to V, and is calculated in Ch. 6.

We conclude with a brief discussion on the implications for interlayer excitons in trilayer devices shown in Fig. 1.10. In particular we predict that at low illumination intensities these excitons condense into droplets of density n_c due to their attraction, and that these droplets do not interact with each other.

Chapter 2

Excess Electron Screening of Charged Impurities in Modern AlGaAs/GaAs Heterostructures

2.1 Introduction

In this chapter, we study the mobility μ and the quantum mobility μ_q of modern AlGaAs/GaAs heterostructures. The contents of these chapters are a reproduction of Refs. [23] and [27]. A typical modern $Al_xGa_{1-x}As$/GaAs heterostructure, schematically shown in Fig. 1.1(a), consists of a GaAs quantum well of width $w = 30$ nm surrounded by $Al_xGa_{1-x}As$ barriers. A 2DEG with a concentration $n_e \simeq 3\times10^{11}$ cm^{-2} fixed by the electrostatics of the device is provided by two remote doping layers symmetrically positioned at setback distances of $d \simeq 80$ nm. It has a low-temperature mobility $\mu \simeq 3\times10^7$ cm^{2}V^{-1}s^{-1} and a quantum mobility[1] $\mu_q \equiv e\tau_q/m^\star \sim 1\times10^6$ cm^{2}V^{-1}s^{-1},[5, 15, 16, 17] where τ_q is the quantum lifetime and $m^\star \approx 0.067m_e$ is the electron effective mass in GaAs. As mentioned in Ch. 1, we separate the mobilities into the contribution μ_R and $\mu_{q,R}$ from the remote ionized impurities (RI), and the contribution μ_B and$\mu_{q,B}$ from the background charged impurities (BI). In modern heterostructures, the BI concentration is extremely small ($\lesssim 10^{14}$ cm^{-3}) and the doping layers have a sophisticated design

[1] Quantum mobility governs the amplitude of low-field quantum oscillations,[18, 19, 20, 21] which increase exponentially with μ_q.

which substantially reduces RI scattering.

As shown in Fig. 1.1(b), each doping layer consists of a narrow (typical width of 3 nm) GaAs quantum well, which is doped in the middle by a δ-layer of Si donors with a typical concentration $n \sim 10^{12}$ cm^{-2} and surrounded by AlAs layers with a typical width of 2 nm. The doping layer shown in Fig. 1.1(b) is a special case of a short-period GaAs/AlAs superlattice (SPSL), suggested by Baba[93] and later implemented by Friedland[22]. Following Refs. [6], [7], and [22] we use this abbreviation for the doping scheme shown in Fig. 1.1(b). To our knowledge, the structure shown in Fig. 1.1a was first realized in the early 2000s,[94, 95] although single heterointerfaces with one such doping layer appeared much earlier[96, 97].

The SPSL-doping scheme augments the advantage of weak RI scattering of the 2DEG electrons. In AlAs/GaAs heterostructures with thick layers, the X-minima in AlAs are higher in energy than the Γ-minimum in GaAs. However, for thin layers size quantization plays an important role. In our SPSL-doping layers, the much lighter effective mass in GaAs produces a much larger size quantization energy than in AlAs, raising the Γ-minimum in GaAs above the X-minima in AlAs.[98, 99] Thus, a concentration fn of electrons which are not transferred to the 2DEG (excess electrons) are stored in the AlAs side wells, where f is what we call the donor filling fraction. Each excess electron pairs with a donor in a compact dipole atom, so that their low-temperature parallel-to-2DEG conductance is negligible. Furthermore, excess electrons choose donors which minimize their energy; this leads to significant correlations in the positions of charged donors[24, 25] and thus to a dramatic reduction of RI scattering. In what follows, we call this redistribution of electrons excess electron screening (EES) and describe it by the screening radius r_s. EES is different from the conventional screening by the 2DEG which is described in the paper by the Thomas Fermi (TF) screening radius q_{TF}^{-1} and exists on top of the EES. As we show, EES also reduces the BI potential.

Due to the length of this section, we begin with a quick overview of the plan. In Sec. 2.2 we study the quantum mechanics of an isolated compact dipole atom in the doping layer. We compute the binding energy of an electron in a compact dipole atom and show that its localization length in the plane of the layer is small enough to proceed classically. In Sec. 2.3 we study the screening of fluctuations of the donor concentration $n(\rho)$ by EES and compute μ_R and $\mu_{q,R}$ [Eqs. (2.15) and (2.16)]. We proceed verify these

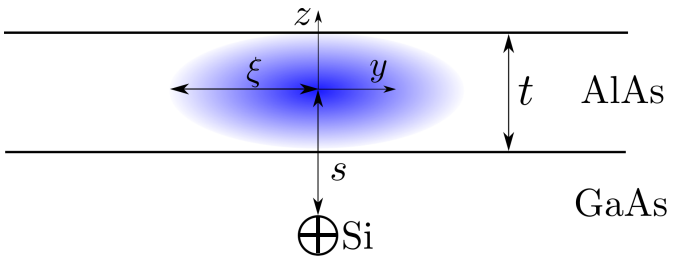

Figure 2.1: (Color online) Schematic image of the electron wave function cloud (blue) in the AlAs layer of thickness t. This cloud is bound to a Si donor (+) in the GaAs layer a distance s away from the midpoint of the AlAs layer. ξ is the electron localization length in the $x-y$ plane.

results with numerical simulations of the remote donor layer in Sec. 2.4. In Sec. 2.5 we provide a simplified description of the BI scattering valid for the sample parameters being considered, followed by a detailed calculation of μ_B and $\mu_{q,B}$ in Sec. 2.6. We conclude in Sec. 2.7 with a comment on the possible relation between the RI potential and the measured gap of the fractional quantum Hall effect at filling factor 5/2.

2.2 Localization of electrons in the doping layers

A remarkable feature of the SPSL-doping scheme is that the excess electrons in the AlAs layers are able to reduce the random potential of donors in the GaAs layer but their parallel-to-2DEG conductance is negligible. As stated above, the main reasons for this are the proximity of the electrons to the donors and the large effective electron mass in AlAs. In this section we justify this claim, showing that excess electrons, while residing in AlAs, are strongly bound to donors in GaAs.

An illustration of an electron bound state is shown in Fig. 2.1. Each excess electron resides in the middle of the AlAs layer of thickness t and is bound to a donor in GaAs at a distance s away with the localization length ξ in the $x-y$ plane. The z-axis is perpendicular to the AlAs/GaAs interface and the origin is centered above the donor at the midpoint of the AlAs layer. The AlAs/GaAs and AlAs/$Al_xGa_{1-x}As$ interfaces are treated as infinite barriers so that the electrons are completely confined to the AlAs layer. This means that there are two competing energy scales: the separation Δ between the first and the second subbands of the AlAs layer and the Coulomb binding energy E_b.

Below we show that $E_b \ll \Delta$ for reference sample parameters $t = 2$ nm and $s = 2.5$ nm. This allows us to think that electrons are bound in the plane at $z = 0$ by an effective 2D potential

$$V(\rho, s) = -\frac{2}{t} \int\limits_{-t/2}^{t/2} dz \cos^2\left(\frac{\pi z}{t}\right) \frac{e^2}{\bar{\kappa}\sqrt{\rho^2 + (s+z)^2}}\,, \tag{2.1}$$

obtained by averaging the Coulomb attraction of the donor over the ground state wave function $\phi(z) = (2/t)^{1/2}\cos(\pi z/t)$. Here $\rho = \sqrt{x^2 + y^2}$ and $\bar{\kappa}$ is the effective dielectric constant. Because the dielectric constants of GaAs ($\kappa \simeq 13$) and AlAs ($\kappa_{\rm A} \simeq 10$) are relatively close, we use $\bar{\kappa} = (\kappa + \kappa_{\rm A})/2 \simeq 11.5$. (Here and below we do not discriminate between the dielectric constants of GaAs and $Al_xGa_{1-x}As$ for the relevant $x \simeq 0.24$.) The corresponding Schrödinger equation is then given by

$$-\frac{\hbar^2}{2m^\star_{xy}}\nabla^2\psi(\rho) + V(\rho, s)\psi(\rho) = -E_b\psi(\rho)\,, \tag{2.2}$$

where $m^\star_{xy}$ is the electron's effective mass in the $x - y$ plane. To find E_b we use a variational approach with the trial wave function

$$\psi(\rho) = \exp\left(-\frac{\sqrt{\rho^2 + s^2}}{b}\right)\,, \tag{2.3}$$

where b is the variational parameter which minimizes E_b.

The results of the variational calculation E_b/Ry and b/a_{xy} as a function of s/a_{xy} are given in Fig. 2.2, where $a_{xy} = \bar{\kappa}\hbar^2/(m^\star_{xy}e^2)$ is the in-plane effective Bohr radius and $Ry = \hbar^2/(2m^\star_{xy}a^2_{xy})$. Using $m^\star_{xy} = 0.22m_e$ for AlAs, we find $a_{xy} \simeq 2.6$ nm and $Ry \simeq 23$ meV near the X-point minima [100]. With $s = 2.5$ nm, we then estimate the electron binding energy $E_b \approx 21$ meV.

Above we have assumed that $E_b \ll \Delta$, allowing us to average the potential over the fast motion along z-direction and treat an electron as two-dimensional. To justify this assumption we estimate the inter-subband separation $\Delta = 3\hbar^2\pi^2/(2m^\star_z t^2)$. The electronic spectrum near the X-point minima in AlAs is anisotropic and $m^\star_z = 0.95m_e$[100]. We find that indeed $\Delta \simeq 0.26$ eV $\gg E_b$.

The localization length ξ of the electron in an isolated dipole atom in the $x-y$ plane is given by

$$\xi = \frac{\hbar}{\sqrt{2m^\star_{xy}E_b}}\,, \tag{2.4}$$

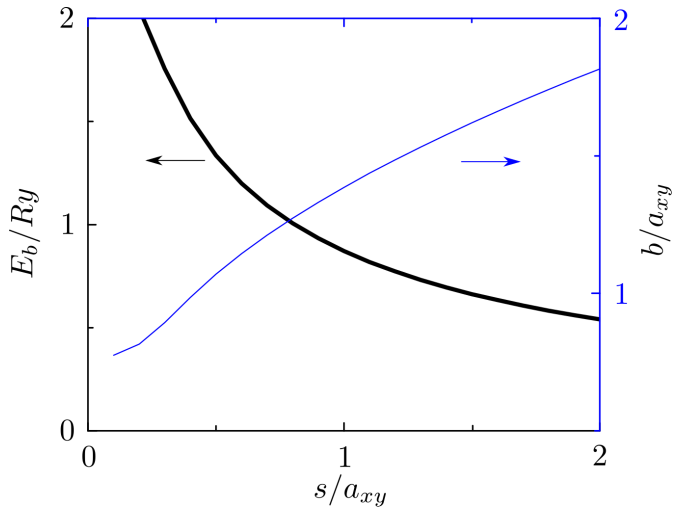

Figure 2.2: (Color online) The binding energy E_b in Ry (thick line) and the variational parameter b in units of the in-plane effective Bohr radius a_{xy} (thin line) as a function of the distance s to the binding donor in units of a_{xy} as obtained from the variational calculation for $t = 2$ nm.

which yields $\xi \simeq 2.7$ nm. For $n = 1 \times 10^{12}$ cm^{-2}, we find $n\xi^2 \simeq 0.07$ which should be compared to the critical value of $(n\xi^2)_c$ below which electrons are localized and transport is activated.

We can estimate $(n\xi^2)_c$ using the data for a Si MOSFET doped by sodium at the SiO_2 side of the interface[101]. These sodium atoms donate electrons which reside on the silicon side of the interface. Such MOSFET is therefore similar to the SPSL-doping layer in which a sodium ion in SiO_2 assumes the role of Si in GaAs. The activation energy E_1 of the electron conductivity along the interface $E_1(n)$ as a function of the surface concentration of sodium n was investigated in Ref. [101]. At small n, $E_1 \approx 24$ meV, in agreement with theoretical predictions for the binding energy of an isolated donor. With increasing n, $E_1(n)$ decreases and extrapolation to large n shows that it vanishes at $n \approx 1.7 \pm 0.5 \times 10^{12}$ cm^{-2}. Using Eq. (2.4) with the binding energy of an isolated donor (24 meV) and the in-plane effective electron mass ($0.19\, m_e$) we find the localization length of the electron bound to an isolated sodium ion $\xi \approx 2.9$ nm and conclude that in Si MOSFET localization sets in at $(n\xi^2)_c \approx 0.14 \pm 0.04$. Since our estimate of $n\xi^2 \approx 0.07$ for SPSL-doping layer is smaller than this value, excess electrons should be localized and their hopping conductivity at low T should be much smaller

than e^2/h (and activated).[2] Measurements of the conductivity of SPSL-doping layers have shown that it is indeed activated[102, 103].

2.3 Scattering by remote donors

Since excess electrons in the AlAs layers and donors in the GaAs layer form compact dipole atoms, scattering from these dipoles can be ignored. However, localized electrons can still choose among host donors, minimizing the total energy of the system. As a result, the ionized donors are screened by the fn electrons, so that the correlator of the random potential energy $\langle U(\boldsymbol{\rho})U(0)\rangle$ is reduced ($\boldsymbol{\rho} = (x, y)$ is a vector in the $x - y$ plane). The Fourier image of the potential correlation function and the Fourier image of the correlator $D(\rho)\,\langle n(0)[1 - f(0)]n(\boldsymbol{\rho})[1 - f(\boldsymbol{\rho})]\rangle$ of ionized donor concentration fluctuations can be related as

$$\left\langle |U(q)|^2 \right\rangle = \left(\frac{2\pi e^2}{\kappa q}\right)^2 D(q), \tag{2.5}$$

and so the screening of the potential can be understood as originating from the correlations of the ionized donors. If donors of concentration n are charged and uncorrelated, $D(q) = n$ in Eq. (2.5). At small f when the concentration of ionized donors is still approximately n, screening by the excess electrons reduces $\left\langle |U(q)|^2 \right\rangle$ (and thus $D(q)$) by the factor $(1 + (qr_s)^{-1})^2$. Accounting for the additional factor $(1 - e^{-2qd_w})^2$ from the images of the donors in the 2DEG, $D(q)$ can be written as

$$D(q) \simeq \frac{(qr_s)^2 n}{(1 - e^{-2qd_w})^2}\,, \tag{2.6}$$

where we have used the condition $qr_s \ll 1$, valid for the important wave numbers $q \sim d_w^{-1}$ and not too small f (see below).

Since $d_w \gg w$ we can treat the 2DEG as if it were confined to an infinitely thin plane located at the center of the quantum well. The contributions of RI scattering to the mobility and quantum mobility can then be calculated using Born approximation

[2] At small enough f, when the density of states of the SPSL structure is small, localization can be achieved even at $n\xi^2 \simeq (n\xi^2)_c$.

as

$$\mu_R^{-1} = \frac{2\pi\hbar}{ea_B^2}\int_0^{2\pi}\frac{d\theta(1-\cos\theta)e^{-2qd_w}}{(q+q_{TF})^2}D(q)\,, \tag{2.7}$$

$$\mu_{q,R}^{-1} = \frac{2\pi\hbar}{ea_B^2}\int_0^{2\pi}\frac{d\theta e^{-2qd_w}}{(q+q_{TF})^2}D(q)\,, \tag{2.8}$$

where $q = 2k_F\,|\sin(\theta/2)|$ is the transferred momentum, θ is the angle between the initial electron wave vector $\mathbf{k}$ and the final wave vector $\mathbf{k}+\mathbf{q}$, $q_{TF} = 2a_B^{-1}$ is the inverse Thomas-Fermi screening radius of the 2DEG, and $a_B = \kappa\hbar^2/m^\star e^2 \simeq 10$ nm is the effective Bohr radius in GaAs.

The main contribution to the integrals in Eqs. (2.7) and (2.8) comes from $q \lesssim (2d_w)^{-1}$. For such q, $q + q_{TF} \simeq q_{TF}$ (since $a_B \ll d_w$). Changing the integration variable to q, and extending the upper bound of integration to ∞ (since $k_F d_w \gg 1$), we find

$$\mu_R^{-1} = \frac{\pi\hbar}{2ek_F^3}\int_0^{\infty} q^2 D(q)e^{-2qd_w}dq\,, \tag{2.9}$$

$$\mu_{q,R}^{-1} = \frac{\pi\hbar}{ek_F}\int_0^{\infty} D(q)e^{-2qd_w}dq\,. \tag{2.10}$$

In Eqs. (2.7), (2.8), (2.9), and (2.10) the random fluctuations of the RI potential are screened twice: once by EES and once by 2DEG screening. In the absence of EES ($f = 0$), a single layer of donors with concentration n is characterized by $D(q) = n$ and one arrives at

$$\mu_R = \frac{8e}{\pi\hbar}\frac{(k_F d_w)^3}{n}\,, \tag{2.11}$$

$$\mu_{q,R} = \frac{2e}{\pi\hbar}\frac{k_F d_w}{n}\,, \tag{2.12}$$

with the well-known ratio $\mu_R/\mu_{q,R} = (2k_F d_w)^2$.

We now return to Eq. (2.6) and calculate r_s for $f \ll 1$. Since only a small concentration fn of excess electrons remain in the AlAs barriers, they only occupy the lowest energy states. Such states are provided by rare pairs of anomalously close donors, separated by distance ρ (see such a pair in Fig. 1.1(b)). An electron forms a dipole with one

donor while the other donor remains ionized and its attractive potential lowers the electron energy by $e^2/\bar{\kappa}\rho$ when $\rho \gg s, \xi$. At small f, one can easily calculate the chemical potential $E_F(f,n)$ which separates the energy levels of the occupied and empty dipole atoms, and is measured from the energy of an isolated dipole atom [104]. The probability to find a second donor in a disk of radius $\rho_F \equiv e^2/\bar{\kappa}\,|E_F|$ centered around the first donor is $\pi n \rho_F^2$. The average concentration of such donor pairs, i.e., the concentration of electrons, is then $\pi n^2 \rho_F^2/2 = fn$, where factor $1/2$ eliminates double counting. Recalling that E_F is negative, one then finds[104]

$$E_F = -\left(\frac{\pi}{2}\right)^{1/2} \frac{e^2 n^{1/2}}{\bar{\kappa}} \frac{1}{f^{1/2}}\,, \tag{2.13}$$

and

$$r_s = \frac{\bar{\kappa}}{2\pi e^2}\frac{1}{n}\frac{dE_F}{df} = \frac{1}{4(2\pi n)^{1/2}}\frac{1}{f^{3/2}} \simeq \frac{0.1}{n^{1/2} f^{3/2}}\,. \tag{2.14}$$

Unfortunately, Eqs. (2.13) and (2.14) are only valid for very small $f \ll 0.15$ [104]. [3]

As mentioned in the introduction, the mobilities likely cross over from being limited by RI scattering to being determined by BI scattering in the range $0.15 < f < 0.39$. In this range, we use the results of numerical modeling of the ground state of the fn excess electrons on n random donors and a neutralizing background [24, 104]. For $0.15 < f < 0.39$ we find a simple fit and find r_s given by Eq. (1.5) with an accuracy of 20%. Using this r_s with Eq. (2.6) and combining with Eqs. (2.9) and (2.10), we arrive at

$$\mu_R \simeq 24 f^3 \frac{e}{\hbar} k_F^3 d_w^5\,, \tag{2.15}$$

$$\mu_{q,R} \simeq 24 f^3 \frac{e}{\hbar} k_F d_w^3\,. \tag{2.16}$$

Our results are based on the assumption that the donors are randomly distributed in the plane of their δ-layer. The distribution of donors at low temperatures is a snapshot of the distribution of donors at a temperature $T_D \sim 800$ K $\sim 6e^2 n^{1/2}/\bar{\kappa}$ below which the diffusion of donors stops. At this temperature dipole atoms are ionized and donors separated by a distance ρ interact with the Coulomb repulsion energy $e^2/\bar{\kappa}\rho$. If $e^2/\bar{\kappa}\rho > T_D$, the probability to find such a pair of donors is reduced by the Boltzmann factor $\exp[-(e^2/\bar{\kappa}\rho)/T_D]$. For the important pairs, $e^2/\bar{\kappa}\rho_F \sim |E_F|$, and using Eq. (2.13) we

[3] The reason is that at $f \geq 0.15$ the correction to Eq. (2.13) from the long-range potential fluctuations becomes substantial.

find that this effect is relevant only at $f \lesssim 0.05$, where EES plays little role. Therefore, Eqs. (2.15) and (2.16) are robust against this effect for experimentally relevant f.

We have also assumed that the system of excess electrons is close to its ground state at low temperatures. Although these electrons are localized, the rate of electron hops from a dipole atom to the nearest empty donor $\gamma \simeq \gamma_0 \exp[-2(n\xi^2)^{-1/2}]$ has a large prefactor $\gamma_0 \sim 10^{12}$ s^{-1} related to the emission of phonons. For $n = 1 \times 10^{12}$ cm^{-2} the exponential factor is $\sim 10^{-3}$ resulting in $\gamma \sim 10^9$ s^{-1}, much larger than the typical rate of cooling of the sample.

Our Eq. (2.15) for μ_R can be compared with Ref. [24] which numerically studied the screening of the RI potential by excess donors in $Al_xGa_{1-x}As$/GaAs heterostructures with a conventional δ-doping in $Al_xGa_{1-x}As$ at $d \leq 50$ nm (only the equilibrium theory of Ref. [24] is relevant here). In the important range of filling fractions $0.2 < f < 0.4$ if we use the parameters of Ref. [24] our μ_R agrees with its Fig. 4(a). Ref. [24] did not study μ_q or BI scattering.

As we saw above, in modern heterostructures both μ_R and $\mu_{q,R}$ are larger than μ_B and $\mu_{q,B}$ at $f > f_c = 0.36$. However, the remote donors can become important for the quantum mobility if one succeeds to substantially reduce BI scattering. We thus would like to estimate μ_R and $\mu_{q,R}$ at $1 - f \ll 1$, i.e., when almost all of the donors form neutral dipole atoms and only a small fraction of donors $1 - f \ll 1$ are ionized. Ionized donors can be treated as holes which repel each other and tend to form a Wigner crystal.[104, 25] If such a crystal were ideal, it would not scatter electrons. However, due to the discreteness of the random positions of donors, holes have to move from their ideal position to the nearest neighbor donor. Each such move effectively creates a dipole with the arm $\sim n^{-1/2}$ randomly oriented in the $x-y$ plane. The number of such dipoles in the relevant square of size d_w is $(1-f)nd_w^2$ and because of their random orientation the amplitude of potential fluctuations created by them in the 2DEG can be estimated as $[(1-f)nd_w^2]^{1/2}(en^{-1/2}/\kappa d_w^2) = (1-f)^{1/2}(e/\kappa d_w)$. A more accurate estimate of the dipole scattering gives,

$$\mu_R \simeq 7.7 \frac{e}{\hbar} \frac{k_F^3 d_w^5}{1-f}\,, \tag{2.17}$$

$$\mu_{q,R} \simeq 6.5 \frac{e}{\hbar} \frac{k_F d_w^3}{1-f}\,. \tag{2.18}$$

Note, that our results for $1 - f \ll 1$ disagree with Ref. [24], which arrived at a much

faster growth of μ_R near $f = 1$. This is because the authors only considered macroscopic fluctuations of the donor concentration and ignored fluctuations in the position of the nearest neighbors mentioned above.

2.4 Numerical Modeling of EES and the Remote Donor Limited Mobilities

In Sec. 2.3, we presented analytical estimates for the effects of EES on the low temperature mobility μ and quantum mobility μ_q[23]. Here we numerically model EES and calculate both mobilities limited by a single remote donor layer containing donors with concentration n and excess electrons with concentration fn. For our analysis we treat f as an independent variable. We show below that the mobilities can be written in terms of the dimensionless mobilities $F(f)$ and $F_q(f)$ defined in Eqs. (1.1) and (1.2). We evaluate $F(f)$ and $F_q(f)$ numerically at all f. Our main results are shown by squares in Fig. 2.3. At $d_w > r_s, k_F^{-1}$, the functions $F(f)$ and $F_q(f)$ should be independent of d_w so that they are universal. Indeed we found that both $F(f)$ and $F_q(f)$ are indistinguishable for $d_w = 7$, 9, and 10 in units $n^{-1/2}$. For $f \ll 1$ and $1 - f \ll 1$ they agree with our Eqs. (1.3) and (1.4). Best linear fits of the data are given by

$$\log F(f) = 3.3f - 0.9, \tag{2.19}$$

$$\log F_q(f) = 3.6f - 1.1, \tag{2.20}$$

and we see that $F(f) \simeq F_q(f)$ for all f.

The results are presented in Fig. 2.3. We see that at $f \ll 1$, Eq. (1.3) is significantly smaller than the numerical results, while Eq. (1.4) is only slightly smaller. This discrepancy originates from the approximations used in Ref. [23], where the inverse mobility was calculated to the lowest order in r_s/d_w and made $F(f)$ and $F_q(f)$ universal functions. Restoring the dependence on r_s/d_w significantly improves the agreement at $f \ll 1$, as shown by the thick dashed lines in Fig. 2.3, where μ and μ_q were calculated for $d_w = 9n^{-1/2}$. For more details see the discussion below Eq. (2.8)

Let us now explain how we arrive to these results. First we generate $N = 10^4$ randomly positioned donors in a square with side L. Then we find the pseudoground state of the system of fN electrons which occupy fN donors in the presence of a neutralizing uniform background charge with density $-e(1-f)n$, where $n = N/L^2$. All charged donors have oppositely charged point-like images in the 2DEG at the distance d_w. We minimize the energy of electrons following the algorithm used in Refs. [104, 24, 25] and arrive at the set of charged donor coordinates in a pseudoground state.

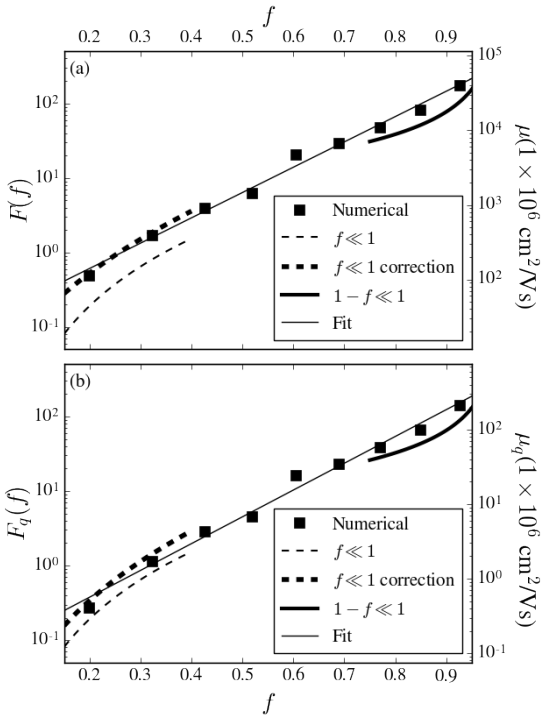

Figure 2.3: The numerical results (squares) for the dimensionless mobilities $F(f)$ (a) and $F_q(f)$ (b) defined in Eqs. (2.15) and (2.16) plotted on a log-linear scale. Asymptotic estimates[23] Eqs. (2.15) and (1.4) are shown at $f \ll 1$ (thin dashed lines) and at $1 - f \ll 1$ (solid curves). The thick dashed lines are improvements to Eqs. (1.3) and (1.4) at $f \ll 1$ for $d_w = 9n^{-1/2}$. Best fit Eqs.(2.19) and (2.20) are shown by the solid straight lines. Corresponding values of μ and μ_q are shown on the right vertical axis for the device described.

The spacial fluctuations of charge is then measured by convolving the charge density of our square with a "Gaussian envelope". Namely, we calculate the weighted number of charges in our Gaussian envelope centered in the middle of our square at $(0, 0)$ as

$$N_R = \sum_i \exp\left[-\frac{(x_i^2 + y_i^2)}{R^2}\right], \tag{2.21}$$

where the sum runs over all charged donors and R is the envelope "radius". We average N_R and N_R^2 over 100 random realizations of our squares for each f. Then we find the mean square fluctuation of the number of charged donors in a Gaussian envelope:

$$\delta N_R^2 = \left\langle N_R^2 \right\rangle - \left\langle N_R \right\rangle^2, \tag{2.22}$$

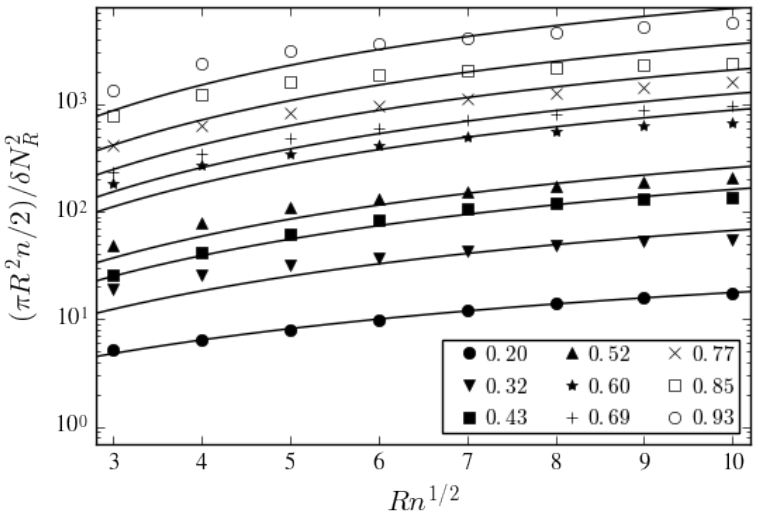

Figure 2.4: Plots of $(\pi R^2 n/2)/\delta N_R^2$ vs. $Rn^{1/2}$ on a log-linear scale for $0.20 \leq f \leq 0.93$. Values of f are given in the legend.

where $\langle ... \rangle$ denotes averaging over 100 realizations In the absence of correlations ($f = 0$), $\langle N_R \rangle = \pi R^2 n$, $\langle N_R^2 \rangle = \pi R^2 n/2 + (\pi R^2 n)^2$, and $\delta N_R^2 = \pi R^2 n/2$.

The results of our simulation of δN_R^2 for $0.20 \leq f \leq 0.93$ are shown in Fig. 2.4 as the ratio $(\pi R^2 n/2)/\delta N_R^2$ on a logarithmic scale. EES reduces δN_R^2 relative to $\pi R^2 n/2$ dramatically with increasing f: $\delta N_R^2 \sim 1$ at $f = 0.20$ and $\delta N_R^2 \sim 0.02$ at $f = 0.92$. The values of f shown in Fig. 2.4 are measured in the center of the square with the help of the identity $\langle N_R \rangle = \pi R^2 n(1 - f)$ and are slightly larger than the original f due to the fringe field at the edge of the square.

δN_R^2 can be related to the correlator of charge density fluctuations $D(\boldsymbol{r}, \boldsymbol{r'}) = \langle n(\boldsymbol{r}) n(\boldsymbol{r'}) \rangle - \langle n(\boldsymbol{r}) \rangle \langle n(\boldsymbol{r'}) \rangle$ ($\boldsymbol{r} = (x, y)$ is a vector in the $x - y$ plane), where $n(\boldsymbol{r}) = \sum_i \delta(\boldsymbol{r_i} - \boldsymbol{r})$. Treating the sum in Eq. (2.21) as an integral over $n(\boldsymbol{r})$, Eq. (2.22) can be written as

$$\delta N_R^2 = \int \int D(\boldsymbol{r}, \boldsymbol{r'}) \exp\left[-\frac{(r^2 + r'^2)}{R^2}\right] d^2 r d^2 r', \tag{2.23}$$

Far from the edges of our square, $D(\boldsymbol{r}, \boldsymbol{r'}) = D(r - r')$ and we may relate it to its Fourier image $D(q)$ as

$$D(r) = \frac{1}{(2\pi)^2} \int D(q) \exp(-i\boldsymbol{q} \cdot \boldsymbol{r}) d^2 q. \tag{2.24}$$

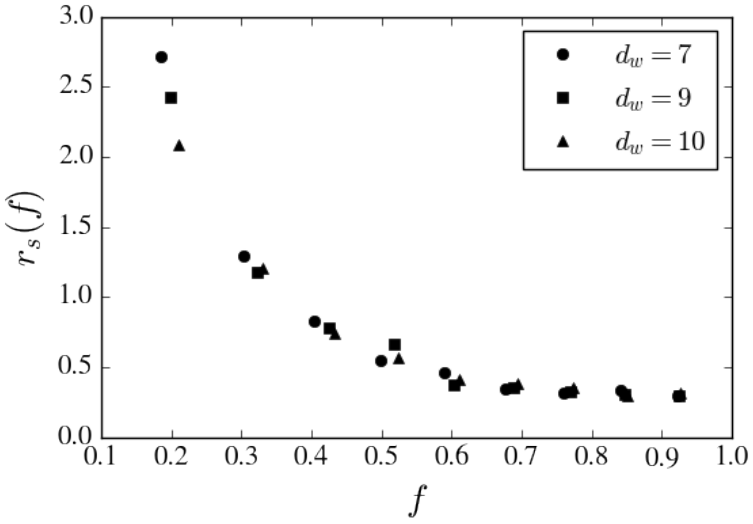

Figure 2.5: The effective screening radius $r_s(f)$ in units $n^{-1/2}$ obtained from fits of the numerical simulations for $d_w = 7$, 9, and 10 in units of $n^{-1/2}$.

Combining Eqs. (2.23) and (2.24), we find

$$\delta N_R^2 = \frac{R^4}{4} \int D(q) \exp\left[-\frac{(qR)^2}{2}\right] d^2q. \tag{2.25}$$

Below we use,

$$D(q) = \frac{(1-f)n(qr_s)^2}{(1+qr_s)^2(1-\exp[-2qd_w])^2}, \tag{2.26}$$

to fit Eq. (2.25) and find the screening radius of the excess electrons $r_s(f)$ as a single fitting parameter. Eq. (2.26) was used for $f \ll 1$ in Sec. 2.3 and led to Eqs. (1.3) and (1.4). Here we have added the additional factor $(1-f)$ because the concentration of charged donors is $(1-f)n$. For $d_w = 9n^{-1/2}$ the best fits of our data are shown by the solid lines in Fig. 2.4. We repeated the simulations for $d_w = 7n^{-1/2}$ and $d_w = 10n^{-1/2}$ and found the same $r_s(f)$ as shown in Fig. 2.5.

Now the mobilities μ and μ_q can be calculated according to Eqs. (2.7) and (2.8) Using Eqs. (2.26), (2.7) and (2.8) with our results for $r_s(f)$ shown in Fig. 2.5, we arrive at $F(f)$ and $F_q(f)$ shown in Fig. 2.3.

In Sec. 2.3 we used the approximate screening radius $r_s = 0.18f^{-3/2}n^{-1/2}$ at $f \ll 1$ to calculate μ and μ_q using Eqs. (2.26)-(2.8). In order to obtain the simple expressions

in Eqs. (1.3) and (1.4), we assumed $r_s \ll d_w$ and set the denominator $(1 + qr_s)^{-2} = 1$ in Eq.(2.26). In order to improve the agreement with the numerical results in Fig. 2.3, we have calculated μ and μ_q using Eq. (2.26) without this approximation for $d_w = 9n^{-1/2}$ and the approximate r_s and obtained the thick dashed lines in Fig. 2.3. For this calculation, we again assumed $k_F^{-1}, a_B \ll d_w$, so that the functions $F(f)$ and $F_q(f)$ depend only on f and nd_w^2.

So far we have dealt only with ideal devices in which the only disorder is the random position of the donors within the δ-layer. In real devices, there are additional types of disorder such as the spreading of the donors throughout the GaAs layer shown in Fig. 1(b), and roughness of the AlGaAs/AlAs/GaAs interfaces of the remote donor layers.[23] This additional disorder can be quite substantial, for instance the roughness of the AlGaAs/AlAs/GaAs interfaces can shift the quantization energy of the excess electrons by several $e^2n^{1/2}/\kappa$, where $e^2n^{1/2}/\kappa$ is the scale of the Coulomb interaction. Such large disorder increases r_s, weakens EES, and reduces the mobilities. To model this disorder, we added to each donor site a random energy E chosen from a Gaussian distribution $(2\pi)^{-1/2}\Gamma^{-1}\exp[-E^2/(2\Gamma^2)]$. The resulting $F(f)$ and $F_q(f)$ obtained from simulations with $\Gamma = 2$ and $\Gamma = 4$ in units of $e^2n^{1/2}/\kappa$ are shown in Fig. 1.2 along with the best fit results for $\Gamma = 0$. Due to increased fluctuations of the results for $\Gamma = 2$, 4, we averaged over 400 realizations of a 100x100 square for both Γ. We see that at small f the difference between the mobilities for $\Gamma = 2$, 4 and $\Gamma = 0$ is small. However at $f \geq 0.4$ the growth of mobilities with increasing f slows and eventually saturates. For $\Gamma = 4$, and for $n_e = 3 \times 10^{11}$ cm^{-2} and $d_w = 90$ nm, we find that μ_q saturates at a level comparable to the highest measured values of $1 - 2 \times 10^6$ cm^{2}V^{-1}s^{-1},[5, 105] while μ is still 10 times larger than the largest experimental values. On the other hand, background impurities may limit μ_q at the same level[23]. This suggests that the improvement of μ_q in record samples requires the minimization of this additional disorder together with the reduction of background impurities.

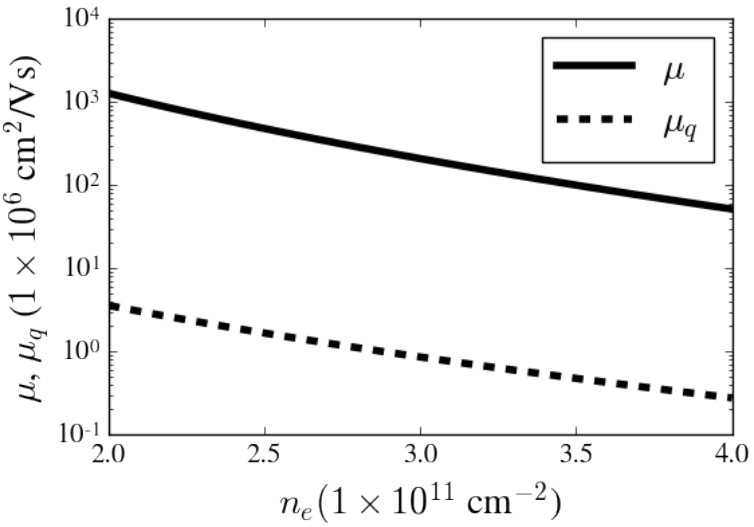

Figure 2.6: Mobility μ and quantum mobility μ_q as functions of n_e plotted on a log-linear scale. Here we assume the mobilities are limited by a single donor layer with $n = 10^{12}$ cm^{-2} donors, where $0.6n$ excess electrons have been lost to the surface.

2.5 Scattering by background impurities

In this section we consider scattering by background impurities in SPSL-doped heterostructures taking into account EES. We begin with μ_B and $\mu_{q,B}$ calculated in the Born approximation as

$$\mu_B^{-1} = \frac{m^{\star 2}}{e\pi\hbar^3 k_F^2} \int_0^{2k_F} \left\langle |U(q)|^2 \right\rangle \frac{q^2}{\sqrt{4k_F^2 - q^2}} dq \,, \tag{2.27}$$

$$\mu_{q,B}^{-1} = \frac{2m^{\star 2}}{e\pi\hbar^3} \int_0^{2k_F} \left\langle |U(q)|^2 \right\rangle \frac{1}{\sqrt{4k_F^2 - q^2}} dq \,, \tag{2.28}$$

where $\left\langle |U(q)|^2 \right\rangle$ is the BI scattering potential.

In this section as everywhere above we assume that the 2DEG occupies the first subband only. Then the square of the wave function is well concentrated in the range $-w/4 < z < w/4$ near the midplane of the quantum well. If the BI are uniformly distributed with a concentration N, then in the absence of EES, the scattering potential can be written as

$$\left\langle |U(q)|^2 \right\rangle = \frac{N}{q} \left(\frac{2\pi e^2}{\kappa(q + q_{TF})} \right)^2 . \tag{2.29}$$

It is easy to see that with such a $\left\langle |U(q)|^2 \right\rangle$ Eq. (2.28) diverges logarithmically. This divergence results from scattering from an infinite number of distant impurities. (These impurities scatter at small angles so that they do not affect transport, and μ_B^{-1} remains finite.) In order to truncate this divergence, one must either consider a sample with finite thickness, or use multiple scattering theory that goes beyond the Born approximation[106, 107].

Let us now show that EES truncates the divergence even stronger. We assume that $f \gtrsim f_c$ so that EES is already so strong that its screening radius $r_s \ll d_w$, i.e. the doping layer screens a static potential as if it were a metal. This means that at $f \geq f_c$, μ_B and $\mu_{q,B}$ are independent of f. Let us consider an impurity at a distance $z > 0$ from the midplane of the 2DEG, as shown in Fig. 2.7. When the impurity is located between the 2DEG and the doping layer, the doping layer creates an oppositely charged image of the impurity at the distance $2d_w - z$ which reduces its potential. When $z \ll d_w$, the image is far from the 2DEG and its effect is small. However, when z becomes close to d_w

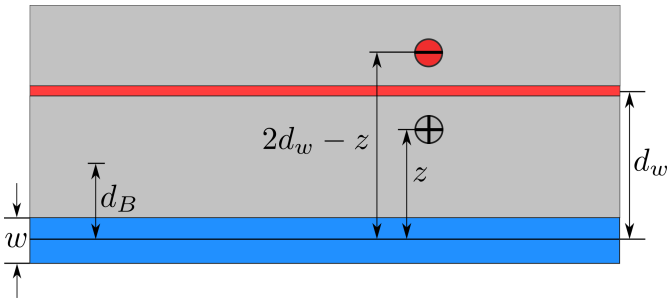

Figure 2.7: The upper half of the structure shown in Fig. 1(a) with an impurity (plus) at a distance z from the midplane of the 2DEG. Due to EES, an image charge (red minus) is produced at a distance $2d_w - z$ from the midplane that reduces the potential of the impurity.

as shown in Fig. 2.7 the impurity forms a compact dipole with its image whose potential in the 2DEG practically does not scatter. Thus, the scattering off of impurities located at distances larger than a critical distance $z = d_B$ becomes negligible. We can estimate d_B by solving the equation

$$\left(\frac{e}{\kappa d_B} - \frac{e}{\kappa(2d_w - d_B)}\right)^2 = \frac{1}{2}\left(\frac{e}{\kappa d_B}\right)^2 , \tag{2.30}$$

which gives $d_B \simeq 0.5 d_w$. Here we use the squares of the potentials as they lead to scattering. Furthermore, we can ignore the impurities at $z > d_w$, as the doping layer acts as a Faraday cage which screens these impurities.[4] Thus we need to consider only the impurities within the finite distance $|z| < d_B$.

Now let us make our model more general and assume that the BI concentrations outside and inside the well are N_1 and N_2, respectively. Then we can write the linear equations

$$\mu_B^{-1} = A_1 N_1 + A_2 N_2 , \tag{2.31}$$

$$\mu_{q,B}^{-1} = B_1 N_1 + B_2 N_2 , \tag{2.32}$$

for the mobilities μ_B and $\mu_{q,B}$ with coefficients A_1, A_2, B_1, and B_2 which are estimated below.

[4] For these impurities the scattering potential is reduced by the factor $4(d_w/r_s)^2 \sim 520$ at $f = f_c$. Strictly speaking the logarithmic divergence of $\mu_{q,B}^{-1}$ exists even in this case. However, it is substantial only for the sample thickness $L \sim \exp(4(d_w/r_s)^2)$ which is unrealistically large and so we can safely ignore the impurities located behind the doping layers.

Let us first concentrate on A_1 and B_1 related to the impurities in the $Al_xGa_{1-x}As$ barriers. Due to EES, only the impurities of the layer $w/2 < |z| < d_B$ contribute to scattering. Because $a_B/2, w/4 < w/2 \ll d_B$, for the purpose of estimates we can apply Eqs. (2.11) and (2.12) to a thin layer of impurities between z and $z + dz$ with concentration $N_1 dz$, and sum the contributions of these layers arriving at

$$\mu_B^{-1} = \frac{\pi}{4}\frac{\hbar}{e}\int\limits_{w/2}^{d_B}\frac{N_1 dz}{(k_F z)^3} = A_1 N_1\,, \tag{2.33}$$

$$\mu_{q,B}^{-1} = \pi\frac{\hbar}{e}\int\limits_{w/2}^{d_B}\frac{N_1 dz}{k_F z} = B_1 N_1\,, \tag{2.34}$$

where we multiplied by 2 as these impurities lie on both sides of the 2DEG. We find[5]

$$A_1 \simeq \frac{\pi}{2}\frac{\hbar}{e}\frac{1}{k_F^3 w^2}\,, \tag{2.35}$$

$$B_1 \simeq \pi\frac{\hbar}{e}\frac{1}{k_F}\ln\left(\frac{d_w}{w}\right)\,. \tag{2.36}$$

Let us switch to A_2 and B_2 which are determined by impurities in the GaAs well. Here, in order to get a very rough estimates we do not discriminate between the two smallest spatial scales, the screening radius of 2DEG $a_B/2 \simeq 5$ nm, and the "half width of electron layer" $w/4 = 7.5$ nm. Then we can write

$$A_2 \approx \frac{\pi}{4}\frac{\hbar}{ek_F}\left(1 + k_F\int\limits_{w/4}^{w/2}\frac{dz}{(k_F z)^3}\right) \simeq 17\frac{\hbar}{e}\frac{1}{k_F^3 w^2}\,, \tag{2.37}$$

$$B_2 \approx \pi\frac{\hbar}{ek_F}\left(1 + k_F\int\limits_{w/4}^{w/2}\frac{dz}{k_F z}\right) \simeq 5\frac{\hbar}{e}\frac{1}{k_F}\,, \tag{2.38}$$

where we took into account that $k_F w/4 \simeq 1$ and replaced z by $w/4$ when integrating from 0 to $w/4$.

Using the reference sample parameters,[6] and expressing the mobilities in units

[5] This result assumes $a_B \ll w$ in contrast to the one[108] for $w \ll a_B$.

[6] We use the following reference sample parameters: $n_e = 3\times10^{11}$ cm^{-2}, $\mu = 3\times10^7$ cm^{2}V^{-1}s^{-1}, $\mu_q = 1\times10^6$ cm^{2}V^{-1}s^{-1}, $d = 80$ nm, $w = 30$ nm, $n = 1\times10^{12}$ cm^{-2}, $t = 2$ nm, and $s = 2.5$ nm. Samples with similar parameters are given in Refs. [7] and [15].

1×10^6 cm^{2}V^{-1}s^{-1} and N_1 and N_2 in units of 10^{14} cm^{-3}, we find that Eqs. (2.35), (2.36), (2.37), (2.38) give $A_1 = 0.005$, $B_1 = 0.20$, $A_2 = 0.06$ and $B_2 = 0.25$. In the next section we develop a quantitative theory of BI scattering which confirms the estimates $A_1 = 0.005$, $B_1 = 0.20$ and leads to slightly larger $A_2 = 0.10$ and $B_2 = 0.33$.

Now one can easily calculate N_1 and N_2 from μ_B and $\mu_{q,B}$ solving Eqs. (2.31) and (2.32). For example, if $\mu = 3 \times 10^7$ cm^{2}V^{-1}s^{-1} and $\mu_q = 1 \times 10^6$ cm^{2}V^{-1}s^{-1}, at $f = f_c$ we can subtract the contribution of μ_R and $\mu_{q,R}$ from μ and μ_q and find $\mu_B = 33 \times 10^6$ cm^{2}V^{-1}s^{-1} and $\mu_{q,B} = 2 \times 10^6$ cm^{2}V^{-1}s^{-1}. They correspond to $N_1 \simeq 2 \times 10^{14}$ cm^{-3} and $N_2 \simeq 2 \times 10^{13}$ cm^{-3}. In this case $Al_xGa_{1-x}As$ accounts for nearly 90% of $\mu_{q,B}$, while it accounts for only 40% of μ_B. This large sensitivity to the $Al_xGa_{1-x}As$ impurities implies that for improvements one should focus not only on the Ga purity,[9] but also on the Al purity as well, particularly if one is interested in high $\mu_{q,B}$.

Previous work[106] has shown that the ratio $\mu_B/\mu_{q,B}$ without EES in single heterojunction devices is ~ 10. As EES reduces BI scattering, one might expect that this ratio would decrease. Yet in the above discussion, we have shown that the ratio $\mu_B/\mu_{q,B}$ can be as large as 18. This large number is a result of allowing N_1 and N_2 to be different, while Ref. [106] assumed that $N_1 = N_2$. The large ratio N_1/N_2 compensates the reduction in BI scattering by EES. If we assume that $N_1 = N_2$, then it follows from Eqs. (2.31) and (2.32) with $A_1 = 0.005$, $B_1 = 0.20$, $A_2 = 0.10$ and $B_2 = 0.33$ that EES reduces the ratio to $\mu_B/\mu_{q,B} \simeq 5$.

Let us now consider a heterostructure in which the bottom doping layer is removed to allow tuning of the electron concentration in the 2DEG by a back gate placed at a distance $L \simeq 800$ nm below the 2DEG[17, 109]. In this case we expect the scattering from the impurities below the 2DEG to increase as distant impurities, which were previously screened by the excess electrons, now contribute to scattering.

The gate also produces images of background impurities which screen their static potential (see Fig. 4). Therefore, we can modify the parameter B_1 by replacing the EES screening length d_B by the gate screening length $L/2$ for the bottom layer and write

$$B_1(L) \simeq \frac{B_1}{2}\left[1 + \frac{\ln(L/w)}{\ln(2d_B/w)}\right]. \tag{2.39}$$

For the reference sample parameters, and $L = 800$ nm we find $B_1(L) \simeq 1.9B_1$. This finding seems to be in qualitative agreement with experiments, which reported higher μ_q in

heterostructures with two SPSL doping layers[15, 16] than in a gated heterostructure[17] of the same w and tuned to the same n_e. Note, however, that the difference in μ_q could also originate from other factors, such as different f or N_1.

Above we have assumed that the Born approximation is valid everywhere and that the logarithmic divergence is truncated by the EES of impurities. In principle, one may go beyond the Born approximation and use a self-consistent multiple scattering theory to truncate the logarithmic divergence, which introduces a truncation length on the order of k_F^2/N_1[106, 107]. For modern samples, $N_1 \sim 10^{14}$ cm^{-3} and the distance $k_F^2/N_1 \sim 0.2$ mm, which is significantly larger than either $d_w/2$ or $L/2$, so that there is no need to use the self-consistent multiple scattering theory.

2.6 Quantitative Theory of Scattering by Background Impurities

We begin by deriving the screened interaction between a 2DEG in a quantum well of width w and an impurity at a distance z away from the center of a quantum well ($z = 0$). The impurity is screened by two electron gases − the 2DEG inside of the quantum well and the excess electrons (EE) in the nearest doping layer a distance $|z| = d_w$ away from the center of the main quantum well (See Fig. 1.1(a)). We ignore the thickness of the doping layer (as it is small compared to d_w) and consider the screening by only the doping layer nearest to the impurity.

The screening of a single impurity is calculated using the random phase approximation (RPA), which amounts to writing a set of self consistent equations for the screened interactions between a charged impurity i and the electrons. Here, we introduce the notation $U_{i,k}$ for the screened impurity interactions and $\widetilde{U}_{i,k}$ for the bare impurity interactions, where the subscript k can be 1 (2DEG) or 2 (EE). Screening occurs because of the electron-electron interactions $\widetilde{U}_{k,l}$, which can be 2DEG-2DEG ($k = l = 1$), EE-EE ($k = l = 2$) or 2DEG-EE ($k = 1, l = 2$). We assume that the electrons are completely confined inside the well and occupy only the first subband, so their linear density in the z-direction is $\lambda_1(z) = (2/w)\cos^2(\pi z/w)\Theta(w/2 - |z|)$. Conversely, since we ignore the thickness of the doping layer, the linear density of the EE is given by $\lambda_2(z) = \delta(z - d_w)$.

Using this notation, the RPA gives the system of equations

$$U_{i,k} = \widetilde{U}_{i,k} + \sum_{l=1}^{2} U_{i,l}\Pi_l \widetilde{U}_{l,k}\,, \tag{2.40}$$

where Π_k are polarization functions of the electrons,

$$\widetilde{U}_{i,k} = \left(\frac{2\pi e^2}{\kappa q}\right) \int dz' \lambda_k(z') e^{-q|z-z'|} \tag{2.41}$$

are the bare impurity-electron interactions, and

$$\widetilde{U}_{k,l} = \left(\frac{2\pi e^2}{\kappa q}\right) \int dz \int dz' \lambda_k(z)\lambda_l(z') e^{-q|z-z'|} \tag{2.42}$$

are the electron-electron interactions. Solving for $U_{i,k}$, we find

$$U_{i,1} = \frac{\widetilde{U}_{i,1}(1-\Pi_2\widetilde{U}_{2,2}) + \widetilde{U}_{i,2}\Pi_2\widetilde{U}_{2,1}}{(1-\Pi_1\widetilde{U}_{1,1})(1-\Pi_2\widetilde{U}_{2,2}) - \Pi_1\Pi_2\widetilde{U}_{1,2}^2}\,. \tag{2.43}$$

The bare impurity interactions are straightforward to calculate from Eqs. (2.41) and (2.42). For $\widetilde{U}_{i,1}$ we find

$$\widetilde{U}_{i,1}(q,z) = \left(\frac{2\pi e^2}{\kappa q}\right) F_0(qw) \begin{cases} \operatorname{csch}\left(\frac{qw}{2}\right)\left[1-\exp\left(\frac{-qw}{2}\right)\cosh(qz)\right], & |z| < w/2 \\ \exp(-qz), & |z| > w/2\,, \end{cases} \tag{2.44}$$

where

$$F_0(x) = \frac{8\pi^2}{x[x^2+4\pi^2]} \sinh\left(\frac{x}{2}\right)\,. \tag{2.45}$$

For $\widetilde{U}_{i,2}$ we find

$$\widetilde{U}_{i,2}(q,z) = \left(\frac{2\pi e^2}{\kappa q}\right) \exp(-q|z-d_w|). \tag{2.46}$$

Similarly, we find for the electron-electron interactions that

$$\widetilde{U}_{1,1} = \left(\frac{2\pi e^2}{\kappa q}\right) G(qw)\,, \tag{2.47}$$

$$\widetilde{U}_{1,2} = \left(\frac{2\pi e^2}{\kappa q}\right) e^{-qd_w} F_0(qw)\,, \tag{2.48}$$

$$\widetilde{U}_{2,2} = \left(\frac{2\pi e^2}{\kappa q}\right)\,, \tag{2.49}$$

where

$$G(x) = \frac{20\pi^2 x^3 + 3x^5 - 32\pi^4(1 - e^{-x} - x)}{x^2(4\pi^2 + x^2)^2}\,. \tag{2.50}$$

For the polarization functions we use the Thomas-Fermi approximation which gives $\Pi_1 = -\kappa q_{TF}/2\pi e^2$ and $\Pi_2 = -\kappa r_s^{-1}/2\pi e^2$.

Let us now examine Eq. (2.43) at different z. For simplicity, we will set $w = 0$ and assume $2qd_w \ll 1$, as small q give the main contribution to $\mu_{q,B}$. For $z \ll d_w$, Eq. (2.43) with the interactions given in Eqs. (2.44)-(2.49) reduces to

$$U_{i,1}(q, z) \simeq \frac{2\pi e^2}{\kappa q_{TF}}\,, \tag{2.51}$$

so that an impurity at small z is screened by the 2DEG but not by the EE. Conversely, for $z \gtrsim d_w$ we find

$$U_{i,1}(q, z) \simeq \frac{r_s e^{-qz}}{2d_w}\left(\frac{2\pi e^2}{\kappa q_{TF}}\right)\,, \tag{2.52}$$

so that at larger z $U_{i,1}$ is suppressed by a factor $2d_w/r_s$. For $f = f_c$ and reference sample parameters, $2d_w/r_s \simeq 23$ and the impurities at $z \gtrsim d_w$ play no role.

The above discussion allows us to make two assumptions that substantially simplify the calculations. First, we ignore EES for the impurities in the GaAs well ($|z| < w/2$). Second, we ignore the impurities in the $Al_xGa_{1-x}As$ beyond the doping layer[54] ($|z| > d_w$). Under these assumptions, μ_B and $\mu_{q,B}$ can be calculated using the Born approximation according to Eqs. (2.27) and (2.28). The scattering potential $\langle|U(q)|^2\rangle$ is given by

$$\langle|U(q)|^2\rangle = \int_{-\infty}^{\infty} N(z) U_{i,1}^2(q, z) dz\,, \tag{2.53}$$

where

$$N(z) = \begin{cases} N_1\,, & |z| > w/2 \\ N_2\,, & |z| < w/2 \end{cases}$$

is the 3D concentration of impurities at a distance z from the center of the 2DEG, N_1 (N_2) is the concentration of impurities in $Al_xGa_{1-x}As$ (GaAs), and $U_{i,1}(q, z)$ is the impurity-electron interaction with EES defined in Eq. (2.44). Performing the integration in Eq. (2.53) yields

$$\langle|U(q)|^2\rangle = \left(\frac{2\pi e^2}{\kappa q}\right)^2 \left[\frac{N_1}{q}\frac{F_1(qw, qd, qr_s)}{\varepsilon^2(q)} + \frac{N_2}{q}\frac{F_2(qw)}{\varepsilon_0^2(q)}\right]\,, \tag{2.54}$$

where

$$F_1(x,y,z) = e^{-x}F_0^2(x)\left[\frac{(1+z)^2 - e^{-2y}[z(2+z)+4y(z+1)] - e^{-4y}}{z^2}\right], \tag{2.55}$$

and

$$F_2(x) = \frac{1}{x}\left(\frac{4\pi^2}{4\pi^2+x^2}\right)^2\left[\frac{8e^{-x}-e^{-2x}-7}{x} + 2(2+e^{-x}) + \frac{2x^2}{\pi^2} + \frac{3x^4}{8\pi^4} - \frac{8x(1-e^{-x})}{4\pi^2+x^2}\right], \tag{2.56}$$

are the form factors[110] for $Al_xGa_{1-x}As$ and GaAs respectively, while

$$\varepsilon(q) = \left(1 + G(qw)\frac{q_{TF}}{q}\right)\left(1 + \frac{1}{qr_s}\right) - F_0^2(qw)\frac{q_{TF}}{q^2 r_s}e^{-2qd_w} \tag{2.57}$$

and

$$\varepsilon_0(q) = 1 + G(qw)\frac{q_{TF}}{q} \tag{2.58}$$

are the dielectric functions with and without EES. With Eqs. (2.54)−(2.58), we can find the coefficients A_1, A_2, B_1, and B_2 in Eqs. (2.31) and (2.32). Using the reference sample parameters, we find $A_1 = 0.005$, $A_2 = 0.10$, $B_1 = 0.20$, and $B_2 = 0.33$.

2.7 Quantum Hall effect at $\nu = 5/2$

In this section we would like to comment on the puzzle of the experimentally obtained gap $\Delta_{5/2}^{exp}$ of the quantum Hall effect at filling factor $\nu = 5/2$ [7, 111, 112]. The observed $\Delta_{5/2}^{exp} \lesssim 0.7$ K is considerably smaller than the theoretical value of $\Delta_{5/2}^{th} \simeq 2$ K and we would like to see if our theory can shed the light on this issue.

If in the absence of 2DEG screening the magnitude of the long range fluctuations of the potential energy of 5/2 excitations $V \lesssim \Delta_{5/2}^{th}$, they should not affect $\Delta_{5/2}^{exp}$ as it is determined by the classical trajectories of excitations with activation over the saddle points[113]. However, when $V \gg \Delta_{5/2}^{th}$ the disorder is nonlinearly screened by the 2DEG and creates large compressible islands separated by relatively narrow stripes of incompressible liquid[114, 115]. In this case, $\Delta_{5/2}^{exp}$ can be substantially smaller than $\Delta_{5/2}^{th}$ due to the following effects[112]. First, the self-energy of charged excitations created in the incompressible stripes is reduced by the proximity of the excitations to the metal-like compressible islands. Second, the tunneling through the saddle points of V can now happen at smaller distances which are comparable with the size of the excitation. Here,

we would like to show that at $f = f_c$ the disorder is already so weak due to EES that $V \sim \Delta_{5/2}^{th}$ and thus there is no reason to expect a substantial deficit of $\Delta_{5/2}^{exp}$.

Even though at $f = f_c$ the remote donors and background impurities provide equal contributions to μ_q^{-1}, their effective concentrations, which determine the spatial scales of their random potentials, are different. Indeed, comparing Eqs. (2.16) and (2.12) we can find that at $f = f_c$ EES reduces n to an effective concentration n_s of randomly positioned charged donors $n_s \simeq 0.57/d_w^2 \approx 6 \times 10^9$ cm$^{-2} \ll n$. On the other hand, the BI potential is due to impurities in the layers of width $0.5d_w$ located on both sides of the 2DEG. For $N_1 \simeq 2 \times 10^{14}$ cm^{-3}, the two-dimensional concentration of such impurities is $n_B = d_w N_1 \approx 2.1 \times 10^9$ cm$^{-2} \approx n_s/3$. As a result, the spatial scale $n_B^{-1/2}$ of the BI potential is larger than the scale $n_s^{-1/2}$ of the RI potential.

Due to their smaller spatial scale $n_s^{-1/2}$, the random fluctuations of the remote donor potential $\sim e n_s^{1/2}/\kappa$ are responsible for tunneling at a saddle point. For fluctuations of the potential energy of the 5/2 excitations with charge $e/4$ this translates to $V \sim e^2 n_s^{1/2}/4\kappa \approx 2$ K $\simeq \Delta_{5/2}^{th}$. Thus the compressible islands of the 2DEG should be small and play marginal role. Then the sum of the two self-energies necessary to create two oppositely-charged excitations should be close to $\Delta_{5/2}^{th}$ and the characteristic tunneling distance at the saddle point of V should be $n_s^{-1/2}$. This distance should be compared to the size of the charge $e/4$ excitations $2l_B$,[112] where $l_B = (\hbar c/eB)^{1/2}$ is the magnetic length. At $B = 5$ T, $2l_B \simeq 23$ nm and $n_s^{-1/2}$ is five times larger than $2l_B$. Thus we expect that tunneling through saddle points plays a very weak role and there should be a range of temperatures in which the transport is activated with no deficit[113]. Of course, at very low temperatures one should expect that tunneling eventually becomes important and hopping transport takes over. At $f < f_c$, the EES is weaker so that the amplitude of the potential energy fluctuations V is larger and leads to large compressible islands and narrow incompressible strips which can substantially reduce $\Delta_{5/2}^{exp}$[5].

Above we assumed that the random positions of donors is the only source of disorder. As shown in the previous section, additional sources of disorder can weaken the effects of EES and lead to the deficit of $\Delta_{5/2}^{exp}$. It is therefore plausible that reduction of these sources of disorder can lead to the increase of $\Delta_{5/2}^{exp}$.

Chapter 3

Anomalous Thermodynamic Properties of Electron Accumulation Layer in $SrTiO_3$

3.1 Introduction

In this chapter, we study the thermodynamic properties of accumulation layers in $SrTiO_3$ (STO). The contents of this chapter are a reproduction of Ref. [47]. In order to describe the accumulation layer, we imagine that a concentration N of positive charge lies at the STO surface. This charge attracts electrons to the surface, creating the accumulation layer (see Fig. 1.3). In Ref. [42], the authors calculated the three-dimensional (3D) electron density profile $n(x)$ of the accumulation layer with a large 2D density N as a function of the distance x from the surface. To account for the nonlinear dielectric response in STO they used the Landau-Ginzburg free energy expansion [43, 44] while describing the degenerate electron gas with the Thomas-Fermi approximation [45]. They arrived at the self-consistent potential

$$\varphi(x) = \frac{C_1}{A^{2/7}} \frac{e}{b} \left(\frac{b}{a}\right)^{8/7} \left(\frac{b}{x+d}\right)^{8/7} \tag{3.1}$$

and the electron density profile

$$n(x) = \frac{C_2}{A^{3/7}} \frac{1}{b^3} \left(\frac{b}{a}\right)^{12/7} \left(\frac{b}{x+d}\right)^{12/7}, \tag{3.2}$$

where $a = 3.9\ \mathring{A}$ is the lattice constant, $b = \hbar^2/m^*e^2 = 0.30\ \mathring{A}$, $m^* = 1.8m_e$ is the effective mass of the electron, m_e is the electron mass, and d is the characteristic decay length of the electron density

$$d = \frac{C_3}{A^{3/5}} b \left(\frac{a}{b}\right)^{2/5} \left(Na^2\right)^{-7/5}. \tag{3.3}$$

Here C_1, C_2, C_3 are dimensionless constants, and A is a numerical constant describing the nonlinear dielectric response. The values of these parameters and all other numerical constants can be found in Tab. 3.2.

We first study the low-temperature magnetization M_s and the specific heat c_s per unit area of such an accumulation layer. Because the neutrality condition

$$N = \int_0^\infty n(x)dx \tag{3.4}$$

converges, one might suspect that M_s and c_s are similar to that of a degenerate electron gas in a uniform layer, with a thickness d, surface concentration N, and a bulk density $n(N) = N/d$. For the purpose of comparison, we denote these quantities in the uniform layer as $\tilde{M}_s$ and $\tilde{c_s}$. Instead, we find that M_s and c_s are strongly enhanced above $\tilde{M}_s$ and $\tilde{c_s}$. The reason for this is that in calculating these quantities, we must integrate the local magnetization $M(x)$ and specific heat $c(x)$ per unit volume across the entire layer. Both these quantities are proportional to the local density of states at the Fermi level, which decreases slowly as $n(x)^{1/3} \propto 1/x^{4/7}$. As a result, integrating $M(x)$ and $c(x)$ over the accumulation layer causes M_s and c_s to diverge, and the integral must be truncated at a large $x = L$. There are several possible mechanisms for the truncation, such as the finite width of the sample W, the crossover to a linear dielectric response with a dielectric constant κ, and the application of a back gate with negative voltage $-|V|$ as shown in Fig. 3.1. As a result, the magnetization $M_s(L)$ and the specific heat $c_s(L)$ per unit area of the accumulation layer are enhanced above their uniform layer values $\tilde{M}_s$ and $\tilde{c_s}$ by a power law factor that depends on the truncation length L. This introduces a power law dependence on the width W, the linear dielectric constant κ, and the magnitude of the back gate voltage $|V|$ depending on which mechanism is responsible for the truncation. Similar anomalous behavior of kinetic coefficients for STO accumulation layers dominated by surface scattering has previously been studied[46]. We emphasize that in this paper we are only discussing thermodynamic properties of the electrons in which the different scattering mechanisms play no role.

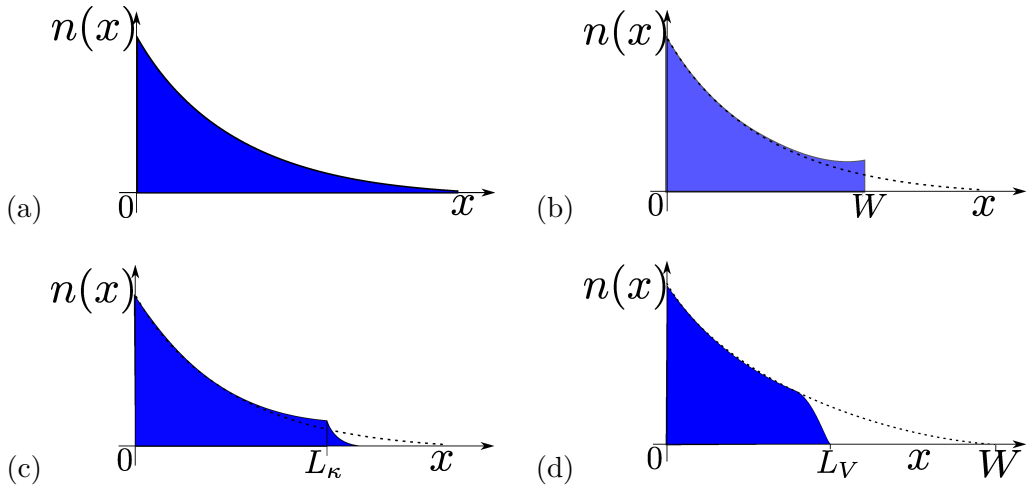

Figure 3.1: Schematics of the density profile $n(x)$ for an accumulation layer in STO with a) no truncation, b) truncation by the finite sample width W, c) truncation by the linear-nonlinear crossover, and d) truncation by the back gate voltage V. Here x is the distance from the surface. The dotted line in b), c), and d), correspond to the density profile without truncation.

The second half of the paper describes the capacitance formed between the accumulation layer and a back gate located at the $x = W$ edge of the sample. When the magnitude of the voltage $|V|$ is small, the capacitance can be described with the usual Debye screening radius and an effective dielectric constant determined by the electric field $E(W)$ at the sample edge. We find that the capacitance in this region is approximately constant with respect to the back gate voltage. However, when the voltage is increased beyond the limit of the Debye theory, the electrons are confined to a region of thickness L_V as measured from the $x = 0$ surface, leaving a fully depleted region of size $W - L_V$ near the back gate. We show that the capacitance in this limit can be described with an effective width $W + \beta L_V$ and a dielectric constant $\kappa(V) \propto V^{-2/3}$ that changes with the back gate voltage. What is surprising is that the coefficient β is positive, leading to an effective width larger than the width of the sample. As we explain in detail below, this counterintuitive result comes from a combination of the dependence of L_V on V and the dependence of the dielectric constant on L_V.

3.2 Magnetization

Let us explore the magnetization of an STO accumulation layer. We assume that the magnetic field is applied perpendicular to the surface, and is weak in the sense that $\mu_B B \ll k_B T$, where $\mu_B = |e|\,\hbar/2m_e c$ is the Bohr magneton, T is the temperature, and k_B is the Boltzmann constant. We know that under these conditions there are two contributions to the magnetization of a degenerate electron gas; the paramagnetic effect from the spins of the electrons and the diamagnetic effect due to the orbital motion of electrons in the applied magnetic field.

First let us discuss Pauli paramagnetism within the accumulation layer.[44] In the weak field limit ($\mu_B B \ll E_F$) the magnetization per unit volume is given by

$$M = \mu_B^2 B g(n) \tag{3.5}$$

where $g(n)$ is the density of states at the Fermi level defined in Eq. (1.7). This formula has a very simple interpretation. The Zeeman splitting of the different spins gives rise to an additional occupancy of electrons whose spin is aligned with the magnetic field. In the weak field limit, the response is linear, so that each electron within an energy range $\mu_B B$ of the Fermi level contributes a moment μ_B to the magnetization. The total density of electrons that contribute is then $\mu_B B g(n)$, giving rise to Eq. (3.5). It is important to note that Eq. (3.5) is valid both in the uniform layer and the accumulation layer, so long as we identify $n = n(x)$ as the bulk density at a distance x from the surface, and $M = M(x)$ as the magnetization per unit volume at the distance x.

In order to calculate the total magnetization per unit area M_s, $M(x)$ must be integrated over the entire layer:

$$M_s = \int_0^\infty M(x)dx. \tag{3.6}$$

Using this definition, we now discuss how M_s differs between the uniform layer and the accumulation layer. In the case of a uniform layer of thickness d and bulk density $n(N) = N/d$, Eq. (3.6) shows that the magnetization is

$$\tilde{M}_s = \alpha \frac{3}{2} \mu_B^2 B \frac{N}{E_F(N/d)}, \tag{3.7}$$

where $E_F(N/d)$ is the Fermi energy of a uniform layer with bulk density N/d. Additionally, we have introduced a correction factor $\alpha < 1$ to account for the diamagnetic contribution(see below).

When the layer is not uniform, we use Eq. (3.2) for the local density. The magnetization of the accumulation layer is then found to be

$$M_s \propto \int_0^\infty \frac{1}{(x+d)^{4/7}} dx. \tag{3.8}$$

We see that the integral diverges as $x^{3/7}$ for large x, and so we truncate the integral at a value $x = L$. With this truncation the leading order contribution to the magnetization per unit area is given by Eq. (1.8).

The truncation length L can be a result of i) the finite width of the sample, ii) truncation due to the transition to a linear dielectric response, and iii) the application of a back gate to the layer. The details of each truncation mechanism will be discussed individually below and the smallest of these values is to be substituted into Eq. (1.8).

Finite Sample Width. In a sample with a very small width, such as GTO/STO/LSAT heterostructures with an STO layer of width W, the truncation is due to the finite sample width. Here LSAT stands for $(LaAlO_3)_{0.3}(Sr_2AlTaO_6)_{0.7}$ In this case the magnetization is given simply by

$$M_s(W) = C_4 \tilde{M}_s \left(\frac{W}{d}\right)^{3/7}. \tag{3.9}$$

For symmetric quantum wells such as GTO/STO/GTO with an STO layer of width W, an accumulation layer forms on each GTO/STO interface and the density profile is symmetric about the center of the well[116]. When $W > 8a = 3.2$ nm, these accumulation layers are essentially separate and one can calculate the magnetization using the above method for each of the layers, using a truncation length of $W/2$ instead of W.

Transition to linear dielectric response. Within the layer, the electric field decays with increasing x as $1/x^{15/7}$. As a result the field at large x becomes so small that the dielectric response of the STO sample becomes linear with a large dielectric constant κ. It has been shown in Ref. [46] that this crossover occurs at a distance

$$L_\kappa = C_5 b \kappa^{7/10} \left(\frac{a}{b}\right)^{2/5} \tag{3.10}$$

where C_5 is a numerical constant[46]. Substituting this into Eq. (1.8), the magnetization of the layer becomes

$$M_s(\kappa) = C_6 \tilde{M}_s \left(\frac{b}{d}\right)^{3/7} \left(\frac{a}{b}\right)^{6/35} \kappa^{3/10} \tag{3.11}$$

where C_6 is a numerical constant.

Truncation by the back gate voltage. In an STO sample of width W, a back gate can be used to apply a voltage V to the gas and alter the structure of the layer. When $V < 0$ electrons are repelled away from the back gate[1] . Let us assume that $n(x)$ vanishes at $x = L_V$, and that $L_V \ll W$, where W is the width of the STO sample. Then we can think that the magnitude of the back gate electric field is $E_x = |V|/W$. Conversely, we mentioned before that the electric field within the accumulation layer $E_x = -d\varphi/dx$ decays like $1/x^{15/7}$, where $\varphi(x)$ is given by Eq. (3.1) . The length L_V can then be defined as the distance in which these two electric fields are equal and we find

$$L_V = \gamma b \left(\frac{b}{a}\right)^{8/15} \left(\frac{|V|\, b^2}{eW}\right)^{-7/15} . \tag{3.12}$$

Here we have introduced a numerical constant γ which cannot be determined from the qualitative description above. A numerical calculation using the Thomas-Fermi approach finds $\gamma \approx 3.94$, and the details of the procedure are described in Appendix. Using L_V as the truncation length in Eq. (1.8), we arrive at the magnetization as a function of back gate voltage

$$M_s(V) = C_7 \tilde{M}_s \left(\frac{b}{d}\right)^{3/7} \left(\frac{b}{a}\right)^{8/35} \left(\frac{eW}{b^2\,|V|}\right)^{1/5} \tag{3.13}$$

where C_7 is a numerical constant.

Diamagnetism. Now we address the correction factor α due to the diamagnetic effect. In a uniform system, this effect leads to the well known value $-(1/3)\tilde{M}_s$, with one major difference. Because the diamagnetic effect is a result of the orbital motion, we must use the effective mass m^* instead of the bare electron mass m_e in the definition of the magnetic moment $\mu_B = |e|\,\hbar/2m^*c$. Because $\tilde{M}_s \propto \mu_B^2$, we find that the correction factor α is then given by

$$\alpha = 1 - \frac{1}{3}\left(\frac{m_e}{m^*}\right)^2 . \tag{3.14}$$

In the case of STO, we use the fact that $m^* = 1.8\ m_e$ and find that $\alpha \approx 0.90$.

[1] When $V > 0$ extra electrons are brought to STO. They form an accumulation layer at the interface with a gate, similar to the symmetric wells GTO/STO/GTO As a result the magnetization and specific heat will grow with V and in the symmetric case are enhanced by a factor $2^{4/7}$ compared to when $V = 0$ and the truncation was by the finite sample width W.

Truncation	$c_s(L)$
Finite Sample Width W	$C_4\tilde{c_s}\left(\frac{W}{d}\right)^{3/7}$
Crossover to Linear Dielectric Constant κ	$C_6\tilde{c_s}\left(\frac{b}{d}\right)^{3/7}\left(\frac{a}{b}\right)^{6/35}\kappa^{3/10}$
Back gate Voltage V	$C_7\tilde{c_s}\left(\frac{b}{d}\right)^{3/7}\left(\frac{b}{a}\right)^{8/35}\left(\frac{eW}{b^2\left\|V\right\|}\right)^{1/5}$

Table 3.1: Specific heat per unit area c_s of the STO accumulation layer for the different truncation mechanisms. Here $\tilde{c_s}$ is the specific heat per unit area of a degenerate gas in a uniform layer of thickness d and bulk concentration N/d, W is the width of the STO sample, κ is the linear dielectric constant of STO, and V is the back gate voltage. C_4, C_6, and C_7 are numerical constants.

3.3 Specific Heat

The specific heat per unit volume of a uniform gas at low temperatures is known to depend linearly on the temperature and described by the formula

$$c = \frac{\pi^2}{3}k_B^2 T g(E_F). \tag{3.15}$$

This equation is similar in nature and interpretation to that of the magnetization for a uniform gas, with $\mu_B B$ replaced by $k_B T$.

Just as before, in order to describe the specific heat of the accumulation layer, Eq. (3.15) must be expressed through its local value and integrated over the entire layer. Because the only dependence on position enters through the density of states, the divergence of the integration is identical to that of the magnetization. Therefore, it can easily be shown that the specific heat of the accumulation layer is given by

$$c_s(L) = C_4\tilde{c_s}\left(\frac{L}{d}\right)^{3/7}, \tag{3.16}$$

where $\tilde{c_s} = (\pi^2/2)k_B^2 TN/E_F(N/d)$ is the specific heat per unit area of the uniform layer of thickness d and bulk density N/d, C_4 is the same numerical constant that appears in

Eq. (1.8), and L is the truncation length. The truncation mechanisms discussed in the previous section are the same for the specific heat leading to the results in Tab. 3.1.

3.4 Back Gate Capacitance of Thin STO Samples

In the previous sections we have discussed the effect of the long tail of $n(x)$ on various thermodynamic quantities, and found that the magnetization and specific heat are enhanced by a factor proportional to $L^{3/7}$. In principle the dependence of M_s and c_s on the truncation length can be used for an experimental study of the tail of the distribution. Here we would like to describe how the capacitance as a function of the back gate voltage may also be used to study the tail of the distribution. A similar study of the quantum capacitance of the accumulation layer has previously been suggested as a tool to measure the characteristic length d of the layer[42]. Earlier negative compressibility in LAO/STO structures was discovered by capacitance studies[117, 118].

In the following dicussion we assume that prior to the application of the back gate the tail is truncated by the sample width W. Let us now imagine that a negative back gate voltage $-|V|$ is applied to the STO sample by a metallic gate mounted on the $x = W$ edge. Let us further assume that part of the tail has been depleted so that the length of the layer is $L_V \ll W$, where L_V is defined in Eq. (3.12). This means that the back gate has "stolen" a small amount of electrons and acquires a negative charge $-\sigma$ while leaving a net positive charge $\sigma = e(N - \int_0^{L_V} n(x)dx)$ on the STO side as illustrated in Fig. 3.2. Thus a capacitor is formed between the accumulation layer and the back gate with charge σ, voltage V, and the inverse differential capacitance per unit area $C^{-1} = dV/d\sigma$.

In order to calculate the differential capacitance C^{-1}, we must first relate the potential V across the capacitor to the charge per unit area σ. We proceed as follows. The region between the plates is fully depleted of electrons. As a result, the electric field E within this region is given by $E = |V|/(W - L_V)$. Additionally, we know from Gauss's law that the displacement field D is such that $D = 4\pi\sigma$. Using the Landau-Ginzburg description of the dielectric response of the STO lattice, one finds that $E = AD^3/((4\pi)^3 P_0^2)$ where $P_0 = e/a^2$ is the characteristic polarization of STO.

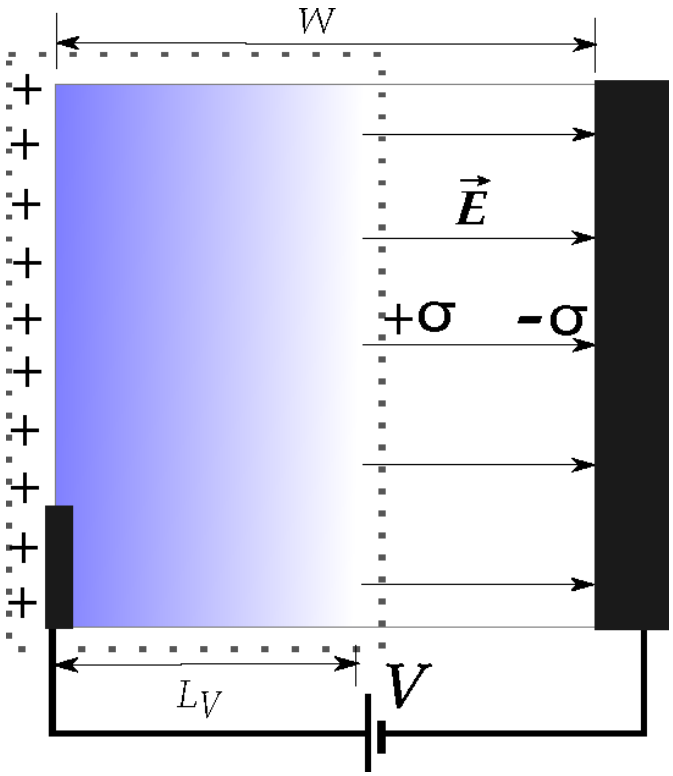

Figure 3.2: Schematic image of the STO layer of width W with a back gate at a negative voltage (right side). The back gate depletes the accumulation layer, so that the electron gas shown in blue (grey) lies in a region of size L_V and a depletion layer of size $W - L_V$ is created. A small number of electrons are "stolen" by the back gate resulting in a negative surface charge $-\sigma$, while the left side (dotted box) gains a net positive surface charge σ and forms a capacitor with the back gate.

Combining these three equations we find that

$$A\frac{\sigma^3}{(e/a^2)^2} = \frac{|V|}{W - L_V}. \tag{3.17}$$

Taking the derivative $dV/d\sigma$, we find

$$C^{-1} \simeq 3A\frac{\sigma^2}{(e/a^2)^2}(W - L_V) - A\frac{dL_V}{d\sigma}\frac{\sigma^3}{(e/a^2)^2}. \tag{3.18}$$

Using Eq. (3.17) with Eq. (3.18) and keeping only the first order in L_V/W, we find $C(V)$ to be

$$C^{-1}(V) = \frac{4\pi}{\kappa(V)}(W + \beta L_V), \tag{3.19}$$

where $\beta = 2/15$ and

$$\kappa(V) = \frac{4\pi}{3}\left(\frac{A^{1/2}\,|V|\,a^2}{We}\right)^{-2/3} \tag{3.20}$$

is the dielectric constant when the accumulation layer is fully depleted.

We see from Eq. (3.19) that the correction to first order in L_V increases the effective width. The fact that this correction is positive may seem counterintuitive as the effective thickness of the capacitor becomes larger than the sample width W. However, we see from Eq. (3.18) that this is not the real width of the capacitor. Instead the positive correction comes from the combined dependence of L_V on the charge σ and the dependence of the dielectric constant on L_V to give an overall positive correction to the main term of order W. If one wishes to verify Eq. (3.19) and the positive correction, one may plot $[4\pi C_V/\kappa(V)]^{-1} - W$ vs. V and examine whether it agrees with the $|V|^{-7/15}$ behavior given by Eq. (3.12).

If the applied voltage is sufficiently small so that $L_V = W$ then there is no fully depleted region. Instead we can linearize the small depletion of the layer around the density $n(W)$ at the right edge of the sample. The capacitance is then given by the familiar expression

$$C^{-1} = \frac{4\pi R_D}{\kappa_{eff}} \tag{3.21}$$

where

$$R_D^2 = \frac{\kappa_{eff}}{4\pi e^2 g(W)} \tag{3.22}$$

is the Debye screening radius, $g(W)$ is the density of states at $x = W$, and $\kappa_{eff} = (1/3)D/E$ is the effective dielectric constant defined by the derivative $\delta D/\delta E$ at the right edge. Using $E = AD^3/((4\pi)^3 P_0^2)$, $E = -d\varphi/dx$ with $\varphi(x)$ from Eq. (3.1), we find

$$\kappa_{eff} = \frac{C_\kappa}{A^{1/7}}\left(\frac{b}{a}\right)^{4/7}\left(\frac{W}{b}\right)^{10/7} \tag{3.23}$$

where C_κ is a numerical coefficent. Combining Eq. (3.23) with $g(W) = g(n(W))$ from Eq. (1.7), we find that

$$C^{-1} = C_8\frac{4\pi W}{\kappa_{eff}} \tag{3.24}$$

where C_8 is a numerical coefficient. If we compare Eq. (3.24) with our earlier expression Eq. (3.19), we see that as the magnitude of the voltage is decreased, the capacitance first

grows, and then saturates at a constant value related to the electron density $n(x)$ near the sample edge. Therefore measurements of the peak capacitance near zero voltage allow for a study of the tail of the density distribution.

Let us discuss in more detail the necessary conditions for this to be observed. In the above discussion, we assumed that the truncation prior to the application of the back gate was by the sample width W. This need not be the case, as when the sample width becomes too large the main truncation will be due to the crossover to a linear dielectric response. This does not change any of the results, so long as we require that $L_V \ll L_\kappa$ whenever W is too large. We can estimate the maximum size of the sample from Eq. (3.10), where we find that $L_\kappa \approx 328$ nm. From this we can use Eq. (3.12) and equate it to the $\min(L_\kappa, W)$ to find the minimum voltage needed to observe the effects of the back gate. Samples such that $W \ll L_\kappa$ have been studied and their capacitance qualitatively agrees with our above predictions[39].

3.5 Discussion

Effective Mass: In the above discussion we have assumed that the band structure of STO near the bottom of the conduction band consists of a single isotropic band with an effective mass m^*. In truth near the conduction band bottom of STO are three degenerate bands formed by xy, xz and yz Ti d-orbitals. This degeneracy is lifted by the spin-orbit interaction and results in two low energy bands that are nearly degenerate and a higher energy band offset by 20 meV[119]. The mass m^* used in the single band Thomas-Fermi approximation comes from the total density of states of all three bands at the Fermi surface. When $E_F \gg 20$ meV or equivalently $n > 10^{19}$ cm^{-3} all 3 bands contribute to m^*. At smaller concentrations, the high energy band is empty and no longer contributes to the density of states. This will slightly lower m^*. This minor difference in m^* does not affect the dependence of the magnetization and specific heat on W, κ, and V and instead only changes the parameter b in all formulas.

Rashba Interaction: The Rashba spin-orbit interaction due to the breaking of inversion symmetry at the interface has been measured in LAO/STO gated structures. This interaction is characterized by the Rashba parameter α_R which is proportional to the electric field E[120]. Near the surface where the field is largest it results in a

splitting between bands by an amount $\Delta = 2\alpha_R k_F \simeq 10$ meV at surface concentrations $N = 4.5 \times 10^{13}$ cm^{-2}. At such concentrations the Fermi energy $E_F(0) = 18$ meV $\gtrsim 10$ meV, so that near the surface the Rashba spin-orbit interaction is marginally small. Far from the surface in the tail of the electron density, which is most important for our results, $\Delta \ll E_F$. The reason for this is that even though the local Fermi energy $E_F(x) \propto x^{-8/7}$ at large x, the electric field $E \propto x^{-15/7}$ and $k_F \propto x^{-4/7}$. Therefore $\Delta/E_F \propto x^{-11/7}$ and the splitting quickly becomes irrelevant.

Bulk Fermi level: Above we have assumed that the bulk of STO is lightly doped by donors, so that the bulk Fermi level lies near the bottom of the conduction band and the density of electrons tends to zero at large x. Actually, bulk STO is believed to be heavily compensated so that Fermi level in the bulk is in the middle of the gap[121]. This does not affect the structure of the accumulation layer as the Fermi level does not acquire its bulk value until distances comparable to the screening radius of thermally activated carriers which is exponentially large at low temperatures.

3.6 Calculation of the numerical constant γ in the back gate truncation length

Eq. (3.12) was derived from a qualitative argument in which the electric fields from the back gate and the accumulation layer were matched. While this procedure should produce the correct scaling behavior, it is not reasonable to expect an accurate numerical coefficient in this way. In order to calculate the coefficient γ, we instead use the Thomas-Fermi approximation in which the self consistent potential $\varphi(x)$ is found to satisfy

$$\frac{d}{dx}\left(\frac{d}{dx}\frac{\varphi}{e/b}\right)^{1/3} = \frac{2^{3/2}}{3\pi^2}\frac{A^{1/3}}{b^{4/3}}\left(\frac{a}{b}\right)^{4/3}\left(\frac{\varphi}{e/b}\right)^{3/2}, \tag{3.25}$$

where $b = \hbar^2/m^* e^2 \approx 0.30$ $\mathring{A}$ has been introduced and $A = 0.9$[42]. This equation was derived for the case of no back gate. In order to account for a back gate with voltage $-|V|$applied to the sample, we simply change $\varphi \to \varphi - |V|$ in Eq. (3.25) In order to prepare for numerical calculations, it is useful to rewrite Eq. (3.25) in a dimensionless form. Using $y = x/b$ and $\chi = (\varphi - |V|)/(e/b)$, we can write this as

$$\frac{d}{dy}\left(\frac{d\chi}{dy}\right)^{1/3} = \theta\chi^{3/2}, \tag{3.26}$$

where $\theta = 2^{3/2}A^{1/3}(a/b)^{4/3}/(3\pi^2)$. It can be verified that this equation can be integrated to find

$$\frac{d\chi}{dy} = -\left(\frac{8}{5}\theta\chi^{5/2} + g_1\right)^{3/4} \tag{3.27}$$

where g_1 is a constant of integration that can be related to the electric field at L_V in the following way. We assume that the electrons only occupy a region $0 < x < L_V$, and so the density profile $n(x)$ vanishes at L_V. Within the Thomas-Fermi approximation, we assume that the density is such that $\hbar^2(3\pi^2 n)^{2/3}/2m^* = e(\varphi - |V|)$, from which it follows that $n(x) \propto \chi^{3/2}$. Therefore, χ must also vanish at L_V. From this and Eq. (3.27), it immediately follows then that

$$g_1 = \left(\frac{d\chi}{dy}\right)^{4/3}\Bigg|_{L_V}. \tag{3.28}$$

Because χ is the dimensionless form of the electric potential, it follows that $-d\chi/dy$ is the electric field E in units of e/b^2, and so $g_1 = E^{4/3}$ in units of e/b^2.

Now that we understand the meaning of g_1, we can find γ as follows. We first guess a value of $E(L_V)$. Once we make this guess, then we know both g_1 and the value of χ at L_V, and so χ is uniquely defined. Eq. (3.27) may then be used to numerically integrate from L_V to any other value of y. In particular, we know what the value of the electric field is at $x = 0$ where it must match the electric field of the positive charges near the surface given by (Eq. (3.4)). So we may perform the integration until the value of $d\chi/dy = A(Nb^2)^3(a/b)^4$. If we track the change in y during this procedure, we can find L_V/b for this particular choice of $E(L_V)$. We can then repeat this process many times in order to generate a curve of L_V vs. $E(L_V)$. Once this curve is obtained, we fit the data to the equation

$$L_V = \gamma\left(\frac{b}{a}\right)^{8/15} E_V^{-7/15} \tag{3.29}$$

where we have assumed the dependence of L_V on b/a and E_V from Eq. (3.12) and L_V and E_V are in units of b and e/b^2. Performing this procedure at a concentration $N = 10^{14}$ cm^{-2} gives us $\gamma = 3.94$. Performing this at concentrations $N = 3\times10^{14}$ cm^{-2} does not change this value within the precision of our calculation.

3.7 Table of coefficients

C_1	C_2	C_3	C_4	C_5	C_6	C_7	A
5.8	1.3	2.4	2.1	3.9	3.7	3.7	0.5-1.5

Table 3.2: Values of the numerical coefficients for the Eqs. in the text.

Chapter 4

Electron Accumulation Layer in Ultrastrong Magnetic Field

4.1 Introduction

The contents of this chapter are a reproduction of Ref. [48]. When a degenerate electron gas at low temperature T is subjected to an ultrastrong magnetic field, its properties undergo dramatic changes. Particularly, when the external field B is so strong such that

$$\hbar\omega_c \gg E_F \gg k_B T, \frac{e^2 n^{1/3}}{\kappa}, \tag{4.1}$$

the cyclotron energy becomes the dominant energy scale in the system. Here $\omega_c = eB/m^*c$ is the cyclotron frequency, m^* is the effective mass, $E_F \approx \hbar^2 n^{2/3}/2m$ is the Fermi energy at $B = 0$, $k_B T$ is the thermal energy, κ is the dielectric constant, and n is the three dimensional concentration of electrons. When Eq. (4.1) is satisfied, we say that the system is in the "extreme quantum limit" (EQL).

Under the influence of a magnetic field $\mathbf{B}$, the kinetic energy of electrons in the direction perpendicular to $\mathbf{B}$ is quantized into Landau levels. In the EQL, the gap between adjacent levels becomes very large and electrons occupy the lowest Landau level only. As a result, the energy of the electron gas depends only on the momentum in the direction parallel to $\mathbf{B}$, creating a quasi-one-dimensional state. It has been proposed that under such conditions, various instabilities such as charge density waves,

spin density waves, or Wigner crystallization occur[122, 123, 124, 125].

We repeat the conditions under which the EQL can be reached. From Eq. (4.1), it follows that in order for the gas to remain metallic, one must have $na_B^3 \gg 1$. Here $a_B = \kappa\hbar^2/m^*e^2$ is the effective Bohr radius of the material. Additionally, the strong magnetic field condition, $\hbar\omega_c \gg E_F$, requires $n\lambda^3 \ll 1$, where I have introduced $\lambda = \sqrt{\hbar c/eB}$ as the magnetic length. Combining $na_B^3 \gg 1$ and $n\lambda^3 \ll 1$, we find that in order to reach the EQL, we require $\lambda \ll a_B$.

Possibly the most ideal material in which the EQL may be reached is bulk (STO), due to the large dielectric constant $\kappa = 2 \times 10^4$, at liquid helium temperatures.[126, 127] As a result, the Bohr radius of STO becomes $a_B = 700$ nm. Several studies of the bulk magnetic properties of the material have been conducted[128, 129, 130, 131], but despite such effort the EQL in bulk STO have not met much success, presumably due to disorder effects[131].

In this chapter, we study the conditions under which one can observe the EQL in electron accumulation layers in semiconductors with a given dielectric constant κ and Bohr radius a_B. Such an accumulation layer can be created in many ways. One example already mentioned is the polar catastrophe in LAO/STO heterostructures which creates an accumulation layer at the interface. Other common techniques include ionic liquid gating[132] of the semiconductor surface and δ-doping by donors in the bulk of the sample[133]. In all such cases the end result is an external electric field $\mathbf{E}$ along the direction perpendicular to the surface that causes electrons to accumulate near the surface. We can always relate E to the surface concentration N of electrons in the accumulation layer by

$$E = \frac{4\pi eN}{\kappa}. \tag{4.2}$$

In our discussion below, all results are expressed through the surface concentration N rather than the external field E.

Within the EQL phase we calculate the Thomas-Fermi profiles of the electron density and electostatic potential as a function of the distance from the surface. By comparing the parameters found in the EQL metal with those of the quasi-classical metal (M), we determine the strength of the magnetic field at which the electrons enter the EQL. On the other end, these parameters are compared to those of the Wigner crystal (WC) phase at a large magnetic field to find the upper limit of the magnetic field at which

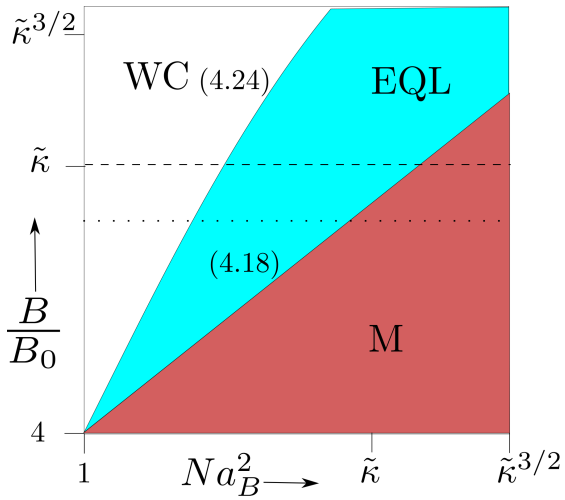

Figure 4.1: Phase diagram of the electron gas for $\mathbf{B} \perp \mathbf{E}$ in the dimensionless plane of B/B_0 and the surface concentration Na_B^2 plotted in a log-log scale. The regions are the quasi-classical metal (M), the metallic EQL phase (EQL), and the insulating Wigner crystal state (WC). The dashed line indicates the ratio B_{max}/B_0 in STO, while the dotted line is the same quantity in InSb. See Eqs. (4.3), and (4.4) in the text for the definitions of B_0 and $\tilde{\kappa}$.

the EQL metal is still valid. Fig. 4.1 summarizes our results for the case of $\mathbf{B} \perp \mathbf{E}$ as a phase diagram in dimensionless units of B/B_0 and Na_B^2. Here

$$B_0 = m^{*2}e^3c/(\kappa^2\hbar^3) \tag{4.3}$$

is the magnetic field such that $\lambda = a_B$. To preserve the universality of Fig. 4.1 for different semiconductor parameters, we introduce the material specific constant

$$\tilde{\kappa} = \frac{\kappa m_e}{m^*}. \tag{4.4}$$

In this notation, $B_0 = (2.5 \times 10^5)\, \tilde{\kappa}^{-2}$ T.

Let us discuss what is achievable experimentally. The strongest static magnetic fields available in laboratories are approximately $B_{max} \simeq 45$ T, from which it follows that

$$B_{max}/B_0 \approx 1.8 \times 10^{-4}\, \tilde{\kappa}^2 \tag{4.5}$$

Given the values of κ and a_B in STO at liquid helium temperatures, we find $\tilde{\kappa} = 1.3 \times 10^4$, and so $B_{max}/B_0 \approx \tilde{\kappa}$, while for InSb, $\tilde{\kappa} = 1.1 \times 10^3$ and $B_{max}/B_0 \approx \tilde{\kappa}^{3/4}$. These values are indicated in Figs.4.1 and 4.2 by the dashed and dotted lines respectively.

Below we focus on STO. Fig. 1.4 presents that phase diagram for $\mathbf{B} \perp \mathbf{E}$ in STO at liquid helium temperatures. The lower EQL border defined by Eq.,(4.18) intersects B_{max} in STO at a concentration $N \simeq 8 \times 10^{12}$ cm^{-2}. Surface concentrations as low as 1×10^{12} cm^{-2} with high mobility have been achieved in modified LAO/STO interfaces and δ-doped STO,[134, 135] so that the lower critical magnetic field is reachable. Additionally, this range of surface concentrations $N = 1 \times 10^{12} - 8 \times 10^{12}$ cm^{-2} corresponds to bulk concentrations N/d ranging between 3×10^{17} cm^{-3} and 1×10^{18} cm^{-3}, where according to the data a reasonably large mobility can be maintained making the EQL achievable in this range of concentrations. Here d is the characteristic width of the accumulation layer.

4.2 Thomas-Fermi Theory of the Accumulation Layer

4.2.1 Quasi-classical Metal

In an accumulation layer, an electric field E applied perpendicular to the the surface causes electrons to accumulate with a three-dimensional concentration $n(x)$, where x is the distance measured from the surface. Here we assume that the semiconductor is such that the Fermi level in the bulk of the material lies at the bottom of the conduction band, and the electron concentration tends to zero at large distances. This can be true if the semiconductor is lightly doped by donors. This problem was first solved in the absence of a magnetic field by Frenkel,[49] and we repeat his argument below.

In order to find the density profile, we make use of the Thomas-Fermi approach in which the local potential $\varphi(x)$ is related to the local chemical potential $\mu(x)$ such that $e\varphi(x) + \mu(x) = \varepsilon_F = 0$. In a normal metal, the chemical potential is related to the density such that

$$\mu_0(x) = \frac{\hbar^2}{2m^*}[3\pi^2 n_0(x)]^{2/3}. \tag{4.6}$$

When the dielectric response is linear, the potential and density are related through Gauss's law, such that

$$\frac{d^2\varphi_0}{dx^2} = \frac{4\pi e}{\kappa} n_0(x). \tag{4.7}$$

Combining Eqs. (4.6) and (4.7) with the above equilibrium condition, we obtain the

Thomas-Fermi Equation

$$\frac{d^2}{dx^2}\left(\frac{\varphi_0}{e/a_B}\right) = \frac{2^{7/2}\kappa^{1/2}}{3\pi a_B^2}\left(\frac{\varphi_0}{e/a_B}\right)^{3/2}. \tag{4.8}$$

The solution of this equation that satisfies the condition $\lim_{x\to\infty}\varphi(x) = 0$ is known to be

$$\varphi_0(x) = C_1\frac{e}{\kappa}\frac{a_B^3}{(x+d_0)^4}, \tag{4.9}$$

and the associated density is

$$n_0(x) = C_2\frac{a^3}{(x+d_0)^6} \tag{4.10}$$

where $C_1 = (225\pi^2/8) \simeq 278$ and $C_2 = (1125\pi/8) \simeq 442$.

To determine the characteristic width d_0, we use the definition of the two-dimensional electron density

$$N = \int_0^\infty n(x)dx. \tag{4.11}$$

Combining Eqs. (4.10) and (4.11) we find that for the quasi-classical metal

$$d_0 = C_3 a_B\left(\frac{1}{Na_B^2}\right)^{1/5}, \tag{4.12}$$

where $C_3 = (225\pi/8)^{1/5} \simeq 2.45$.

4.2.2 Extreme Quantum Limit

The main purpose of this chapter is to understand how the above distribution changes when the gas is subjected to such strong magnetic fields that it is in the EQL.

As stated above, when in the EQL, the kinetic energy in the direction perpendicular to the field is quantized and electrons occupy the lowest Landau level. This means that the density of electrons in the direction perpendicular to the field is fixed by the density of the lowest Landau level $1/(2\pi\lambda^2)$. In addition, the magnetic field aligns the spins in the direction of the field, lifting the spin degeneracy. The remaining direction has a density determined by the wavevector k. We can relate the maximum value of this wave vector to the three dimensional density of electrons by

$$\left(\frac{k}{\pi}\right)\frac{1}{2\pi\lambda^2} = n(x). \tag{4.13}$$

As a result, the local chemical potential changes from Eq. (4.6) to

$$\mu(x) = \frac{\hbar^2}{2m^*}[2\pi^2\lambda^2 n(x)]^2. \tag{4.14}$$

Proceeding in the same way as before, we arrive at the EQL Thomas-Fermi equation

$$\frac{d^2\varphi}{dx^2} = \frac{2^{3/2}e^{1/2}}{\pi(\lambda^4\kappa a_B)^{1/2}}\varphi^{1/2}. \tag{4.15}$$

The solution gives the potential

$$\varphi(x) = C_4\frac{e}{\kappa a_B}\frac{(x-d_\lambda)^4}{\lambda^4}, \tag{4.16}$$

and density as

$$n(x) = C_5\frac{(x-d_\lambda)^2}{a_B\lambda^4}, \tag{4.17}$$

where $C_4 = 1/(18\pi^2) \simeq 0.006$ and $C_5 = 1/(6\pi^3) \simeq 0.005$. Using Eq. (4.11), the characteristic width is determined to be $d_\lambda = C_6(Na_B\lambda^4)^{1/3}$ where $C_6 = (18\pi^3)^{1/3} \simeq 8.23$.

This result is valid when $d_\lambda < d_0$. We find then that the magnetic field compresses the accumulation layer closer to the surface. Equating Eqs. (4.12) and (1.13), and going back to the magnetic field, we find that the EQL is achieved when

$$B > B_{c1} = C_7 B_0 (Na_B^2)^{4/5}, \tag{4.18}$$

where $C_7 = (C_6/C_3)^{3/2} \approx 6.15$. If $B_0 < B < B_{c1}$, $n(x)$ obeys Eq. (4.10) until $\mu(x) = \hbar\omega_c$ where the gas enters the EQL. The distance from the surface at which this occurs is given by

$$x_\lambda \approx (\lambda a_B)^{1/2}. \tag{4.19}$$

At this distance, the remaining electrons are in the EQL and the electron density is sharply cut off.

We emphasize that the direction of the magnetic field has played no role in our discussion so far. Therefore, we see that our boundary given by Eq. (4.18) is independent of the field direction. This line is shown in both Fig. 4.1 and Fig. 4.2. For $B \gg B_{c1}$, these diagrams lose their universality and we discuss them separately in the following section.

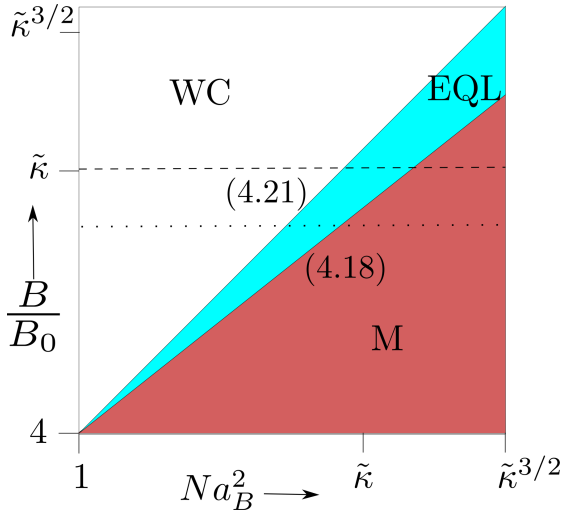

Figure 4.2: Phase diagram of the electron gas for $\boldsymbol{B} \parallel \boldsymbol{E}$ in the dimensionless plane of B/B_0 and the surface concentration Na_B^2 plotted in a log-log scale. The regions are the quasi-classical metal (M), the metallic EQL phase (EQL), and the insulating Wigner crystal state (WC). The dashed line indicates the ratio B_{max}/B_0 in STO, while the dotted line is the same quantity in InSb. See Eqs. (4.3), and (4.4) in the text for the definitions of B_0 and $\tilde{\kappa}$. Numerical values of N and B for STO at liquid helium temperatures can easily be recovered from comparison of Figs. 1.4 and 4.1.

4.3 Phase Diagrams for different Magnetic field directions

Below we address the role of the magnetic field direction and complete the phase diagrams Figs. 4.1 and 4.2. Let us assume that the electric field is strong enough such that $Na_B^2 > 1$. The Thomas-Fermi approximation is only valid as long as the electrons can be treated semiclassically. We can make this condition quantitative by requiring that

$$\frac{1}{\pi}\int_0^\infty k_x(x)dx > 1 \tag{4.20}$$

which is a generalization of the 1d particle in a box. This condition depends on the direction of the magnetic field relative to the electric field, and so below we consider separately the two cases $\boldsymbol{B} \parallel \boldsymbol{E}$ and $\boldsymbol{B} \perp \boldsymbol{E}$.

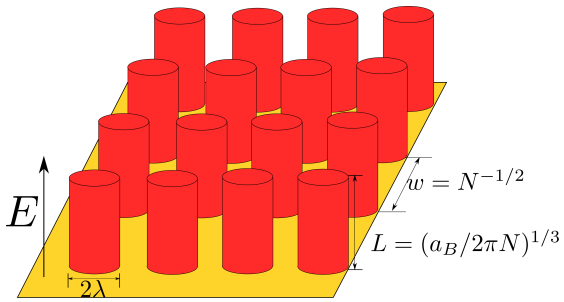

Figure 4.3: (Color Online) Schematic of the electron structure in the WC phase for **B** ∥ **E**. Each electron (red/dark grey) forms a cylinder of radius λ oriented along the direction of the magnetic field on the surface (yellow/light grey) inside the semiconductor.

4.3.1 Magnetic Field Parallel to Electric Field

When **B** ∥ **E**, $k_x(x) = 2\pi^2\lambda^2 n(x)$. From this we find that the approximation breaks down when

$$B = B_{c2} = B_0(2\pi N a_B^2). \tag{4.21}$$

This is the boundary between regions EQL and WC in Fig. 4.2. As the magnetic field is increased beyond this value, the Thomas-Fermi approximation becomes invalid everywhere. Instead, the electron gas forms a WC consisting of single electron cylinders of radius λ and height L (see Fig. (4.3)). The height of the cylinders can be determined as follows. At the border B_{c2}, the electron gas is confined to the first sub-band of a triangular potential well. The kinetic energy is then

$$K = \frac{\hbar^2}{2mL^2} \tag{4.22}$$

while its potential energy is $U = eEL/2$, where E is related to N by Eq. (4.2). Equating the kinetic and potential energies we find that

$$L = (a_B/2\pi N)^{1/3}. \tag{4.23}$$

The height of the cylinders L should agree parametrically with the size of the accumulation layer d_λ along the EQL-WC phase boundary Eq. (4.21). Let us confirm this. Along the boundary, we know that Eq. (4.21) gives $N = 1/\lambda^2$, so that $L = (\lambda^2 a)^{1/3}$. If instead we are coming from the EQL region, we find that $d_\lambda = (\lambda^2 a_B)^{1/3}$.

Eq. (4.23) is the same as the width of the first sub-band wave functions obtained for an inversion layer in an electric field E.[136, 137] However, contrary to the inversion layer where electrons are delocalized in the plane perpendicular to the field E, electrons here are strongly localized by the magnetic field in a cylinder of size λ. This is also the simplest case of quantum screening[138, 139, 140].

4.3.2 Magnetic Field Perpendicular to Electric Field

If $\mathbf{B} \perp \mathbf{E}$, $k_x = 1/\lambda$. As a result, we find instead of Eq. (4.21) that the Thomas-Fermi approximation fails when $B > B_0(Na_B^2)^2$. We show below that the EQL phase forms a WC at a somewhat smaller field

$$B_{c3} \approx \frac{B_0(Na_B^2)^2}{(\ln(Na_B^2))^2}. \tag{4.24}$$

This is the boundary given in Fig. 4.1.

The structure of the WC phase for $\mathbf{B} \perp \mathbf{E}$ is markedly different than when $\mathbf{B} \parallel \mathbf{E}$. We can imagine the electrons as cylinders of radius λ oriented along B which lie on their sides in the plane of the surface (See Fig. 1.5).

To describe the WC, one can imagine that E is replaced by a uniform positive surface charge density eN which is partitioned into Wigner-Seitz (WS) cells with charge e, length L, and width $w = 1/NL$ so that each cell contains exactly one electron. We assume that the energy of each WS cell is approximately given by the sum of the kinetic energy Eq. (4.22), and the electrostatic energy $U = -(e^2/\kappa L)\ln(NL^2)$. Optimization of this energy with respect to L gives

$$L \simeq \frac{a_B}{\ln(Na_B^2)}. \tag{4.25}$$

As the magnetic field is reduced, it is natural to assume that the WC-EQL transition occurs when the electron is the same size as the WS cell. Setting $w = \lambda$, and using Eq. (4.25), we arrive at the border Eq. (4.24). We see that the logarithmic term in the denominator of Eq. (4.24) resembles those obtained previously for the metal-insulator transition in the bulk of a doped semiconductor in a strong magnetic field.[141, 139]

Up until now our theory is generic and is valid for any semiconductor material with a linear dielectric constant. In STO, however, the dielectric response becomes nonlinear at

sufficiently high surface concentrations.[42] It was shown the dielectric response becomes nonlinear when

$$Na_B^2 = N_{c1}a_B^2 = \frac{1}{\sqrt{\kappa}}\left(\frac{a_B}{a_0}\right)^2 \approx \tilde{\kappa}^{3/2}. \tag{4.26}$$

Here $a_0 \simeq 3.9\ \mathring{A}$ is the lattice constant in STO. We see in Figs. 4.1 and 4.2 that at this concentration, B_{max} is such that the gas is still in region M, where the magnetic field only acts to cut the tail of the distribution. Thus, the EQL phase is unachievable experimentally when the dielectric response is nonlinear and so we limit Figs. 4.1 and 4.2 to $Na_B^2 < \tilde{\kappa}^{3/2}$.

4.4 Magnetocapacitance

In this section we calculate the capacitance of an accumulation layer as a function of the magnetic field for all phases. Our results can be used as tools for an experimental study of Figs. 4.1 and 4.2. For the setup we imagine that the accumulation layer is either created by the electric field of a metallic gate, or by a built in electric field E to which a metallic gate adds a relatively small field E'. Examples of such devices include the gating of an intrinsic semiconductor by an ionic liquid and the application of a metallic gate to the top LAO surface in the LAO/STO heterostructure. In both cases one can study the differential capacitance per unit area $C = d(eN)/dV$, where V is the gate voltage. The inverse capacitance C^{-1} may be written as the sum of the inverse geometrical capacitance and the inverse quantum capacitance

$$C_q^{-1} = \frac{4\pi d_q}{\kappa}. \tag{4.27}$$

Below we calculate d_q for our phases M, EQL, and WC in both $\mathbf{B} \parallel \mathbf{E}$ and $\mathbf{B} \perp \mathbf{E}$ cases.

Let us discuss some of these results. In Sec.4.2 the Thomas-Fermi potential profiles were found for the metallic M and EQL phases. From Eq. (4.9), we find that in region M the potential difference from $x = 0$ to $x = \infty$ at a given concentration is

$$\varphi(N) = \pi\left(\frac{225\pi}{8}\right)^{1/5}\frac{e}{\kappa a_B}(Na_B^2)^{4/5}. \tag{4.28}$$

Taking the derivative $d\varphi/dN$ and using Eq. (4.27), one finds

$$d_q(M) = \frac{d_0}{5}. \tag{4.29}$$

In the EQL we know that the potential is instead given by Eq. (4.16) where d_λ is given by Eq. (1.13). Proceeding in the same way, we find that the EQL changes the capacitance to

$$d_q(EQL) = \frac{d_\lambda}{3}. \tag{4.30}$$

Eqs. (4.29) and (4.30) are not surprising. In both cases, d_q is the width of the accumulation layer in the direction of the electric field E, up to some numerical prefactor. To put another way, the effective width of the quantum capacitor is the width of the accumulation layer.

In order to find the point at which the capacitance transitions from that of the quasi-classical metal to the EQL metal, we equate Eqs. 4.29) and (4.30). We find then that the EQL becomes observable in capacitance measurements at $B'_{c1} = (5/3)^{3/2} B_{c1}$, which is slightly larger than Eq. (4.18). At this field we should see the effects of the EQL begin to emerge, and so we use this as the field at which the gas transitions.

Eqs. (4.29) and (4.30) are valid for both $\mathbf{B} \parallel \mathbf{E}$ and $\mathbf{B} \perp \mathbf{E}$ cases. As the magnetic field is increased, the two cases separate because of their different WC structure. We first discuss the $\mathbf{B} \parallel \mathbf{E}$ case. As the magnetic field is increased, we see from Eq. (4.30) that d_q will decrease. When $B = B_{c2}$ (Eq. (4.21)), a Wigner transition occurs and the gas enters the WC region. In this state, the width of the accumulation layer in the direction of E is approximately given by Eq. (4.23) and no longer depends on the magnetic field. In order to find the value of the capacitance, we combine Eqs. (4.21) and (4.30) and find

$$d_q(\mathrm{WC}_\parallel) = C_8 \frac{a_B}{(N a_B^2)^{1/3}} \tag{4.31}$$

where $C_8 = (\pi/6)^{1/3} \approx 0.81$.

When $\mathbf{B} \perp \mathbf{E}$ the transition to the WC phase happens at a much larger B given by Eq. (4.24). At this value of the field, the width of the accumulation layer is such that $d_q \sim 1/N a_B$. If the field is increased further, then d_q continues to decrease as the negative energy due to correlation effects of the WC begin to dominate[104]. However at such large fields, the distance between electrons may become comparable to the distance between the WC and the gate, and the coupling of electrons to their image charge becomes the dominant factor in the determination of the capacitance.[142] Despite this, such magnetic fields are too high to reach experimentally, and so we refrain from any

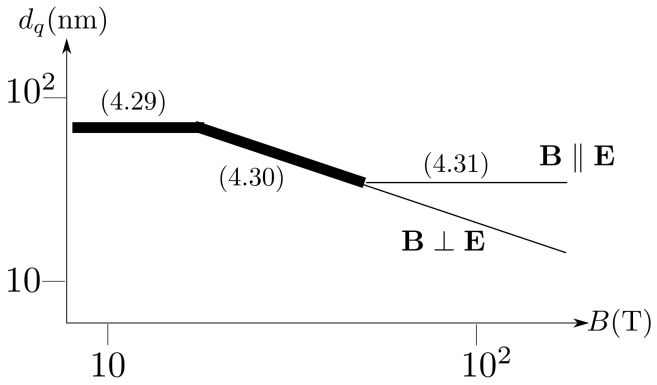

Figure 4.4: Log-log plot of d_q(nm) as a function of B(T) for the phases of Figs. 4.1 and 4.2 in STO at liquid helium temperatures with a surface concentration $N = 10^{12}$ cm^{-2}. The region in which d_q is the same for both $\boldsymbol{B} \parallel \boldsymbol{E}$ and $\boldsymbol{B} \perp \boldsymbol{E}$ is illustrated by a thick line. The numbers in parentheses correspond to equations in the text.

further discussion of this limit.

We summarize these results in Fig. 4.4 as a plot of d_q vs. B for STO samples with a surface concentration $N = 10^{12}$ cm^{-2}. At this concentration, the transition into the EQL occurs when $B = B'_{c1} \approx 18$ T while the EQL-WC transition occurs at $B = B_{c2} \approx 46$ T. We see then that the EQL phase is within the realistic range of magnetic fields and so capacitance measurements at this concentration provide an opportunity in which the first border will be observed. However if one wishes to see the splitting between the two directions, one needs to go to lower concentrations than $N = 10^{12}$ cm^{-2}.

4.5 Heavy Atoms in Pulsars

So far, we have restricted our discussion to electron accumulation layers in semiconductor materials with such large Bohr radii that the EQL is achievable experimentally. For atoms, the EQL is achieved when the magnetic field is larger than $B_0 = 2.34 \times 10^5$ T and is completely unattainable in a laboratory setting. However, in rotating neutron stars, or pulsars, the magnetic fields at the surface range from $10^8 - 10^9$ T[107], so that the EQL can be achievable even for atoms. The effect of the large magnetic field on the structure of the surface layer of neutron stars has been studied extensively[143].

It is believed that within the surface of neutron stars there exists a layer enriched by iron atoms[144]. Motivated by this, Kadomtsev studied heavy atoms in ultrastrong magnetic fields, where he used an EQL Thomas-Fermi equation which is the spherically symmetric analog of our Eq. (4.15)[145, 146]. He found that the EQL Thomas-Fermi description of the atom is valid as long as the magnetic field is in the range

$$Z^{4/3} \ll \frac{B}{B_0} \ll Z^3 \tag{4.32}$$

where Z is the nuclear charge of the atom. When $B/B_0 \ll Z^{4/3}$, the magnetic field has only a perturbative effect on the atomic structure, while for $B/B_0 \gg Z^3$, the atom is elongated along the direction of the magnetic field. We will now show that there exists a mapping between the nuclear charge Z and the surface concentration N showing that the $Z^{4/3}$ and Z^3 borders are in agreement with those we found for the EQL phase when $\boldsymbol{B} \parallel \boldsymbol{E}$.

We can imagine that within the accumulation layer, electrons are bound at a distance d away from the surface by the positively charged plane with charge density eN. We can think that this plane consists of positive squares (nuclei) of length d and charge

$$Z = Nd^2. \tag{4.33}$$

At the lower critical field B_{c1}, we know that the characteristic width of the gas is given by Eq. (4.12). Using Eq. (4.33) we find that the nuclear charge at this field is $Z = (Na_B^2)^{3/5}$. From here, we find then that the lower critical field B_{c1} given by Eq. (4.18) is related to the nuclear charge by

$$\frac{B_{c1}}{B_0} = (Na^2)^{4/5} = Z^{4/3} \tag{4.34}$$

in agreement with the lower border of Eq. (4.32). On the other hand, we know that if the magnetic field is applied parallel to the electric field, the Thomas-Fermi approximation fails when $B = B_{c2}$, where B_{c2} is given by Eq. (4.21). At this field strength, the width of the layer d is given by Eq. (1.13), from which it follows that $Nd^2 = (Na_B^2)^{5/3}(B_0/B)^{4/3}$. Solving this equation for B, and using Eq. (4.21), we find that the EQL region ends when

$$\frac{B}{B_0} = Z^3 \tag{4.35}$$

in agreement with Kadomtsev's second border.

Note that in our comparison, we have used the case of $\boldsymbol{B} \parallel \boldsymbol{E}$. In a heavy atom, the magnetic field can be both parallel and perpendicular to the electric field of the nucleus. However, we know from Sec. III that when the $\boldsymbol{B} \parallel \boldsymbol{E}$, the Thomas-Fermi approximation fails at a smaller B than for the case of $\boldsymbol{B} \perp \boldsymbol{E}$. It is for this reason that the mapping from the accumulation layer to the heavy atoms needs $\boldsymbol{B} \parallel \boldsymbol{E}$.

Let us conclude with a discussion about the structure of the atom when $B/B_0 \gg Z^3$. At such fields all electrons are in the lowest Landau level and occupy a single sub-band in the direction of the field B. From the above mapping, it would seem natural to expect the structure to be similar to a WC where the same limits apply. Actually, due to the strength of the Coulomb field of the point charge Z, the electrons instead compress into a single uniformly charged cylinder of radius $R = \lambda Z^{1/2}$ and height $L = a_B/Z \ln(B/Z^3)$. The compression of the cylinder is stopped by the kinetic energy $\hbar^2/(2mL^2)$ along the direction of B. One can think that in our Fig. 4.2, the atom becomes "frozen" at the EQL-WC border when $B/B_0 \gg Z^3$.

Chapter 5

Roughness scattering induced insulator-metal-insulator transition in a quantum wire

5.1 Introduction

Much of the focus in nanowire technology is in creating ballistic nanowires that can support the Majorana zero edge modes for quantum computation[63, 64]. In this chapter, we fill the gaps in the theoretical description of roughness limited mobility both for quantum wells and quantum wires. We show below that the possibility to achieve ballistic transport depends strongly on the radius R and the length $\mathcal{L}$ of the wire. Namely, we derive the roughness limited Drude mobility and the "metallic window" shown in Fig. 1.7. The contents of this chapter are a reproduction of Ref. [74].

Before addressing why such a window exists, let us describe conventional models of roughness developed for quantum wells. In a quantum well confined by interfaces at $z = 0$ and $z = L$, the surface roughness is a random shift of the interface position $\Delta(\vec{r})$ from the average level so that $< \Delta(\vec{r}) >= 0$, where $\vec{r} = (x, y)$ is the coordinate in $z = 0$ (or $z = L$) interface plane. The roughness is described by the height correlator and its

Fourier transform

$$\begin{aligned} < \Delta(\vec{r})\Delta(\vec{r'}) > &= W(\vec{r} - \vec{r'}), \\ < |\Delta(q)|^2 > &= W(q). \end{aligned} \tag{5.1}$$

First theories of surface roughness scattering have assumed the correlator to be Gaussian.[1, 147, 107, 148, 149].

$$\begin{aligned} W(\vec{r} - \vec{r'}) &= \Delta^2 e^{-(\vec{r}-\vec{r'})^2/d^2}, \\ W(q) &= \pi\Delta^2 d^2 e^{-q^2 d^2/4}. \end{aligned} \tag{5.2}$$

However, experimental observations using TEM and STM measurements of Si/SiO_2 interfaces and InAs/GaSb interfaces found that the spacial correlations follow an exponential behavior [150, 151]

$$\begin{aligned} W(\vec{r} - \vec{r'}) &= \Delta^2 e^{-\sqrt{2}|\vec{r}-\vec{r'}|/d}, \\ W(q) &= \pi\Delta^2 d^2 (1 + q^2 d^2/2)^{-3/2}. \end{aligned} \tag{5.3}$$

This correlator describes randomly distributed flat islands of typical thickness Δ and diameter d on the top of the last complete layer of the crystal [75]. On the other hand, Gaussian roughness can be visualized as randomly positioned stacks of total height Δ and diameter d made of progressively smaller islands of flat atomic layers on the top of bigger ones [75] similar to the ancient Mayan pyramids. As we show below, in many cases the two correlators give the same expression for the mobility in terms of Δ and d, and so the difference in parameter values can have serious implications. Only at very large electron densities when $k_F d \gg 1$, (k_F is the Fermi wave number), do the two correlators give different expressions for the mobility. This difference is relatively unimportant for this work, so we give results only for the exponential correlator.

While the above isotropic roughness models were designed for quantum wells with flat interfaces, they are valid for quantum wires of characteristic size $R > d$. [1] In the most of this chapter we deal with such roughness. However TEM images of InAs wires[70] suggest that in quantum wires another model of roughness in which the radius of the wire varies along its axis may be more realistic. We discuss this "Variable Radius Model" (VRM) and its implications in Sec. 5.7.

[1] For the case of cylindrical wires, the characteristic size R would be the radius of the wire. However, the results presented are applicable to any cross-section that can be described with a single characteristic length, such as a square wire with side length 2R or a regular hexagonal wire in which R is the distance from the center of thewire to each vertex.

We consider wires with linear electron concentration η doped by a relatively distant back gate (we assume that there are no chemical donors in the wire). Then the interplay between the concentration η, the radius of the wire R, and the semiconductor Bohr radius a_B determines the number of filled subbands of radial quantization, what is the Fermi wavenumber k_F of electrons, and whether the confinement is electrostatic or by the surface barriers (referred to as geometric confinement). Here the effective Bohr radius $a_B = \kappa\hbar^2/m^*e^2$, κ is the effective dielectric constant, $\hbar$ is the reduced Planck constant, and m^* is the effective electron mass. This means that for quantum wires, there are five lengths Δ, d, η^{-1}, R, and a_B, or four dimensionless lengths when all are scaled by a_B, that determine the Drude mobility.

Below we use the scaling theory to calculate the low temperature roughness limited Drude mobility μ in units $(e/\hbar)\left(d^4/\Delta^2\right)$ as a function of the dimensionless variables R/a_B and ηa_B. Here the use of Drude's name signifies that we ignore interference effects and electron-electron correlations. Our results for different regions in Fig. 1.6 as a "phase diagram" in the plane of R/a_B and ηa_B, the details of which are elaborated in Sec. 5.5. For the most interesting case $\Delta \ll d \ll a_B$ we find a total of 9 regions $A-I$ whose mobilities are listed in Table 1.1. It should be noted that due to the limitations of the scaling theory, the mobility expressions for the different regions of the phase diagram are valid only away from the borders between different regions. In the vicinity of the border between regions, there is a smooth crossover between the two mobilities, the details of which are beyond the scope of this thesis. While the scaling approach only gives the dependence of mobility on the different parameters without numerical precision, its simplicity allows for a clear picture of the different physical domains and the approximate limits under which they occur.

Now we are ready to address the origin of the Drude conductance peak which leads to the "metallic window" for large R, illustrated by the colored regions in Fig. 1.6. Schematic plots of the Drude conductance (in units e^2/h) $G = \eta\mu h/\mathcal{L}e$ of the wire with length $\mathcal{L}$ are shown in Fig. 1.7 for two representative values of R by full lines. They are obtained from cross sections of Fig. 1.6 and the mobilities in Table 1.1. At low concentrations, we see that the Drude conductance increases with increasing concentration. This corresponds to Region G of Fig. 1.6, where there is a single radial subband occupied and the electrons are confined geometrically. We know from Fermi's golden rule that the

relaxation time τ is inversely proportional to the density of states at the Fermi energy, which in the one-dimensional (1D) case goes like $1/k_F \sim \eta$. The scattering potential however is independent of concentration in this regime. Therefore, the relaxation time τ, the mobility μ, and conductance G increase with concentration due to the decrease in the density of states. This trend continues until the concentration is large enough that multiple subbands become occupied. Now electrons have more states to scatter into, and the relaxation time quickly decreases with increasing concentration. Thus the conductance peaks at the border concentration η_c when electrons begin to populate multiple subbands. The peak of the Drude conductance for the most interesting cases of $R \leq a_B$ is given by

$$G_{max} = \frac{R^5}{\mathcal{L}\Delta^2 d^2}. \tag{5.4}$$

So far we have ignored electron-electron interactions and quantum interference effects. They dramatically change the conductivity of one dimensional systems at low temperatures. For single subband wires (regions D and G) electron-electron interactions result in Wigner-crystal-like correlations and pinning of the electron gas leading to the metal-insulator crossover near $\eta a_B = 0.5$[152]. In Fig. 1.7 the corresponding collapse of conductance at $\eta a_B < 0.5$ is shown by the dashed lines. According to Luttinger liquid theory [77, 78] similar effects persist at very low temperatures in very long wires. We are interested here in relatively short wires with $\mathcal{L} \sim 1$ μm, where plasmon quantization does not allow such effects to develop [78]. Therefore, for $\eta a_B > 1$ we can ignore electron-electron interactions. However, in this case we should still take into account quantum interference effects. They lead to one-electron localization when the dimensionless conductance $G < 1$. This means that when $G_{max} < 1$ (see lower curve in Fig. 1.7), the wire is an insulator at any concentration η. On the other hand, for $G_{max} > 1$ (see upper curve in in Fig. 1.7) the wire has a concentration window of metallic behavior. The critical radius $R_c(\mathcal{L})$ in which the metallic window opens is then determined by the condition that $G_{max} = 1$. For G_{max} defined by Eq. (5.4) we find $R_c(\mathcal{L}) = (\Delta^2 d^2 \mathcal{L})^{1/5}$. Note that the restriction that $\eta a_B > 0.5$ necessary for the single subband wires to be metallic requires $R_c < 2a_B$.

The conductance peak leads to the zero temperature reentrant insulator-metal-insulator transition with increasing η in quantum wires with $R > R_c(\mathcal{L})$. Such a transition was first predicted for a two-dimensional electron gas (2DEG) in silicon

MOSFET[76]. However it was later shown[75] that there is no second reentrant metal-insulator transition at large concentrations of a 2DEG as the dimensionless conductance saturates at a value larger than unity. As our paper shows the idea of Ref. [76] is realized in quantum wires. (For more details see our Sec. II below.)

The metallic regimes for a wire with $R_c(\mathcal{L}) < a_B$ are shown in different colors in Fig.1.6, while regions where the electrons are localized are left blank. The dark red, light red, and pink colored regions of the metallic regime specify a single-subband ballistic conductor, a many-subband ballistic conductor, and a diffusive metal respectively. It should be emphasized that the metal-insulator and ballistic-diffusive borders depend on the wire length. With decreasing $\mathcal{L}$ and $R_c(\mathcal{L})$ the colored regions expand dramatically and for short wires eventually cover most of the phase diagram. In Fig. 1.6 we used $\mathcal{L} \sim 1$ μm as in Fig. 1.7, which is typically used in quantum devices (see details in Sec. 5.8).

The detailed derivation of all the metallic border equations are given in Sec. 5.6 and in Tab. 5.2. Here we give a brief summary of the derivation. Let us begin with the metal-insulator border. For $\eta a_B > 0.5$ this border comes from the condition that the Drude conductance $G_D = e^2/h$, and gives rise to the sequence of border lines between the colored and uncolored regions with minimum at $R_c(\mathcal{L})$ in Fig. 1.6. For $\eta a_B < 0.5$ there is no metallic regime for the single subband regions (G and H), as illustrated by the vertical line that cuts off the dark red region of Fig. 1.6 at low concentrations. This line continues vertically to the asymptotic line $\eta a_B \sim C(R/a_B)$, which can be understood as the Wigner crystallization of the 2DEG at $na_B^2 = C \ll 1$, where $n = \eta/2\pi R$. Finally we address the ballistic-diffusive border which only exists in the regions with many subbands occupied. Typically, a diffusive metal becomes ballistic when the mean free path $l = \mathcal{L}$. However, for the many subband regions there is an ambiguity, as we can have different l for different subbands. Fortunately, the conductance in these cases is determined by a small subset of subbands which have identical l and we define the ballistic-diffusive border by the line where $l = \mathcal{L}$ for these subbands.

Let us discuss the conductance in the different colored regions of Fig. 1.6. We begin with the ballistic regimes (red regions of Fig. 1.6). Here the dimensionless conductance $G \approx 2K$, where K is the number of ballistic channels of a wire with finite length $\mathcal{L}$, and the factor of 2 comes from the spin degeneracy. Estimates of K can be found in

Sec. 5.6. Within the diffusive regime (pink regions of Fig. 1.6) $G = (h/e)\eta\mu/\mathcal{L}$, where the mobility is given in Tab. 1.1. Finally, in the insulating regions electrons are localized at temperature $T = 0$. At finite T wires conduct via phonon assisted hopping. Calculations of the hopping conductivity are relatively straightforward, but are beyond the scope of this thesis.

5.2 Roughness limited mobility results for quantum wells

To understand the roughness limited mobility of quantum wires, it is convenient to first make clear of that in quantum wells. We start from a quantum well confined by two high potential barriers at $z = 0$, L. It has the two-dimensional (2D) electron concentration n created either by two positive donor layers located symmetrically on both sides of the well or by two symmetric metallic gates. In both cases, at $z = 0$, L there is an electric field pointing into the well with $|E| = 2\pi ne$, where e is the electron charge. Interplay of effects of the electric field and barrier confinement creates 5 different types of wells shown in Fig. 5.1 in regions I - IX. In a narrow well the electric field E plays a minor role in level quantization compared to confining barriers so that we assume that all subbands are geometrically confined in the small L regions VI, VII, VIII, and IX in Fig. 5.1. When the concentration is relatively small, electrons occupy only the first subband. At larger n electrons populate many subbands (see the level schematics in regions VI and VII in Fig. 5.1). In wider wells shown in regions I, II, III, IV and V the electric field becomes important compared to the surface barriers. In turn this leads to the splitting of the electron density in two peaks. With growing L, in the beginning (regions IV and V) this splitting is moderate and affects only the lowest subbands. In regions II and III the splitting results in two separate accumulation layers in response to the electric field each side of the well. Finally at large L and small n we again reach the single subband limit, however the confinement is electrostatic rather than geometric (region I in Fig. 5.1).

The roughness limited mobility of a single-subband electron gas of a quantum well (regions I, VIII and IX) was thoroughly studied in Refs. [1, 147, 107, 148] more than 30 years ago. On the other hand, the roughness limited mobility of accumulation layers was calculated recently in Ref. [75], results of which are directly applicable to regions

II and III. However, no work has been done in the intermediate regions where many subbands are occupied but the electric field is weak so that some or all of the subbands are confined geometrically (regions IV, V, VI, and VII). In the next two sections we fill this gap. Below, because of the complexity of the problem, we first present the final results in this section and then give their derivations in next section. The complete results at $d \ll a_B$ are shown in Fig. 5.1 and Table 5.1. The single subband results I, VIII, and IX are taken from Refs. [1, 147, 107, 148] and accumulation layer results II and III are from Ref. [75]. For the intermediate regions IV, V, VI, and VII, we obtain their results in this section.

Let us first look at the physical meaning and corresponding equations of boundary lines in Fig. 5.1. Across the line between Region I and Region II, the concentration becomes so large that electrons have to occupy multiple subbands (see level schematics in Fig. 5.1). With n further increased, $k_F d$ becomes larger than unity in Region III where k_F is the three-dimensional (3D) electron Fermi wavenumber here. Instead of averaging over different islands, the electron hits only a single island now. This leads to the change of the mobility result at the II-III border.

For regions I, II, and III, all subbands are electrostatically confined. For moderately smaller well width L, some of the subbands become geometrically confined. This happens when the well width L becomes smaller than the characteristic thickness D of the accumulation layer, where[49, 153]

$$D \simeq \frac{a_B}{\left(n a_B^2\right)^{1/5}}. \tag{5.5}$$

The criterion $L = D$ then gives the line between II, III and IV, V. At the line between IV and V, $k_F d = 1$.

With further reduction of L, all subbands would be geometrically confined (see the level schematic in Fig. 5.1). This happens when the electrostatically confined distance of the lowest subband electrons from the surface is equal to the well width L. This distance is $D_0 \simeq a_B^{1/3}/n^{1/3}$ (see Refs. [1, 148]) which is the smallest among all subbands since the lowest subband has the smallest kinetic energy in the z direction. The condition $L = D_0$ gives the line between IV, V and VI, VII. The border between VI and VII corresponding to the critical point of $k_F d = 1$ is a continuation of the line between regions IV and V. Moving to even smaller L from regions VI and VII, we cross over to the single subband

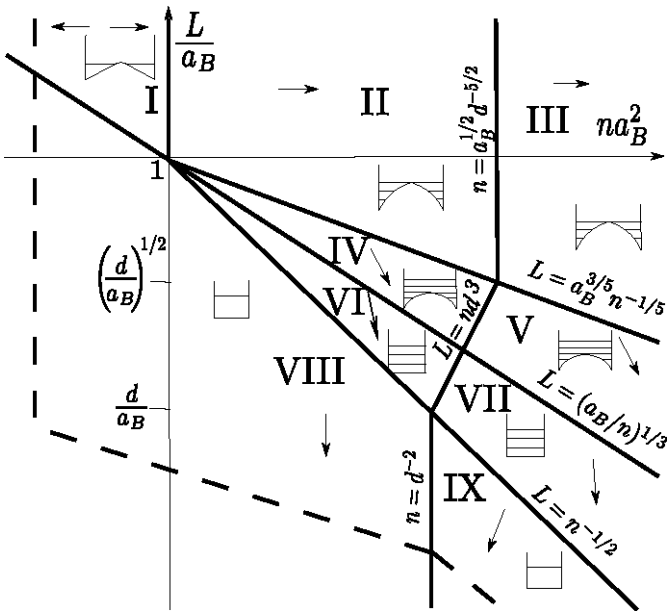

Figure 5.1: The scaling "phase diagram" of roughness limited electron mobility of quantum well at different well width L and 2D electron concentration n for $d \ll a_B$ in the log-log scale. Different "phases" or regions are denoted by Roman numerals. Mobility expressions corresponding to these regions are given in Table 5.1. Region boundaries are given by the equations next to them. The schematic self-consistent electron potential energy profile along the z-axis of wells and levels (subbands) occupied by electrons are shown for each region. Small arrows show the direction of mobility decrease in each region. Apparently the maximum mobility is achieved in Region I. The dashed line indicates schematically the border of the metal-insulator transition (MIT) at small enough n. At large n there is no reentrant MIT in spite of the decreasing mobility.

(see the level schematic in Fig. 5.1). This corresponds to the line $k_F L = 1$ between VI, VII and VIII, IX. The border of the VIII and IX regions is the line of $k_F d = 1$ where k_F is the 2D electron Fermi wavenumber here. In Fig. 5.1, one can see that there is another border line between I and VIII, which both correspond to a single subband gas. However, Region I corresponds to two electrostatically split electron subbands near the two well interfaces, while Region VIII represents the case that the electron subband is spatially restricted by the well width L (see the level schematic in Fig. 5.1). Their crossover happens at the point that both electrostatic and geometric confinements give the same thickness of the electron gas. Remember that the electrostatically confined thickness of the first subband is D_0. Then the condition $L = D_0$ gives the border. So

Table 5.1: Mobility μ in units of $(e/\hbar)\left(d^4/\Delta^2\right)$ as a function of the 2D electron concentration n at $d < a_B$ for different regions.

I	II	III
a_B^2/n^2d^6	$a_B^{8/5}/n^{11/5}d^6$	a_B/nd^3
IV	V	VI
$a_B^{1/2}L^{11/6}/n^{11/6}d^6$	$a_B^{1/2}L^{5/6}/n^{5/6}d^3$	$L^{10/3}/n^{4/3}d^6$
VII	VIII	IX
$L^{7/3}/n^{1/3}d^3$	L^6/d^6	$L^6n^{3/2}/d^3$

this line between I and VIII is just an extension of the line between IV, V and VI, VII.

One should note that here in Table 5.1, all results are shown without numerical coefficients, i.e., we present only the scaling behavior. Previous works have already found the exact coefficients in the single subband regions I, VIII, and IX [1, 147]. Results of many subband regions II, IV, and VI with $k_Fd \ll 1$ can also be obtained with the approximate coefficients as seen later in Sec. 5.3. We cannot get coefficients analytically in remaining regions III, V, and VII. Thus we focus only on the scaling behaviors in all tables and derivations.

In Fig. 5.1 the metal-insulator transtition (MIT) is shown schematically by the dashed lines. Let us dwell on the meaning of these lines. The lower line is related to the localization physics of a non-interacting electron gas. Strictly speaking all states are localized in 2D infinite samples, however at $k_Fl \gg 1$ the localization length grows exponentially as $\zeta = l\exp(k_Fl)$, where l is the mean free path. In finite square samples of area A we have in mind that ζ quickly becomes larger than the sample size $A^{1/2}$. This allows one to discuss the metallic conductivity and expect the insulator-metal transition near $\sigma = (e^2/\hbar)\ln(A^{1/2}/l)$. Ignoring the logarithm and using the expressions of mobility μ for VIII and IX in Table 5.1 as well as $\sigma = ne\mu$, one gets that the low L MIT border of Region VIII obeys $L = \Delta^{1/3}d^{1/3}n^{-1/6}$. We also find the MIT border of Region IX is $L = \Delta^{1/3}d^{-1/6}n^{-5/12}$. We have used $\Delta/d = (d/a_B)^{8/5}$ in order to draw these lines.

The vertical line $na_B^2 = C \ll 1$ reflects the role of the Coulomb interaction between electrons in a degenerate electron gas. At $na_B^2 \ll 1$ strong Coulomb repulsion leads to Wigner crystallization. The Wigner crystal is pinned by relatively small disorder and electrons become localized.

5.3 Roughness limited mobility derivations for quantum wells

In the previous section, we have presented the physical picture of all 9 regions and their border lines and summarized the mobility results. In this section, we derive the new expressions of mobility for regions IV, V, VI, and VII. First, let us derive μ for Region VI. According to Fermi's golden rule and the Boltzmann equation, the relaxation time τ_N of a particular state with the wavefunction $\xi(z, \vec{r})$ and with in-plane velocity $\vec{v_k}$ in the N-th (counted from the bottom lowest subband) subband is

$$\frac{1}{\tau_N} = \frac{2\pi}{\hbar} \sum_{N'} \int \frac{d^2k'}{(2\pi)^2} \frac{|V(q)|^2}{\epsilon(q)^2} \delta(\varepsilon - \varepsilon_F) \left(1 - \frac{\vec{v_{k'}} \cdot \vec{E}}{\vec{v_k} \cdot \vec{E}} \frac{\tau'_N}{\tau_N}\right), \tag{5.6}$$

where τ_N, τ'_N denote the relaxation time for N, N'-th subbands, $\vec{v}_{k'}$ is the in-plane velocity for the final state with the wavefunction ξ' in the N'-subband with in-plane momentum $\vec{k'}$, ε is the energy of the final state ξ' and ε_F is the Fermi energy, q is the transferred momentum in the $x-y$ plane between ξ and ξ'. Here V is the scattering matrix element arising from the scattering potential. Due to the electronic screening, the Fourier transform of the scattering potential $V(q)$ is reduced by the dielectric function $\epsilon(q)$ [1]. One should note that here the last term inside the parenthesis of Eq. (5.6) does not reduce to $\cos\theta$, where θ is the angle between initial and final total momenta. This is because, due to the 2D nature of the surface roughness and thus of the scattering potential, the multisubband electron gas experiences anisotropic scattering, i.e., different subbands have different relaxation times [2] . As a result $\cos\theta$ in Eq. (5.6) is replaced by the ratio of the out-of-equilibrium part of distribution function of the states ξ' and ξ represented by $\left(\vec{v_{k'}} \cdot \vec{E} / \vec{v_k} \cdot \vec{E}\right) (\tau'_N/\tau_N)$ (see Ref. [154]). For brevity, we refer to this term as the distribution function ratio (DFR) from now on.

[2] One should note here that the definition of relaxation time τ is still valid according to Ref. [154], which might be broken in more complicated cases.

It is known that the roughness-caused scattering potential $V(\vec{r})$ and corresponding scattering matrix element $V(q)$ satisfy the equation[1, 75]

$$\begin{aligned} V(r) &= \frac{\hbar^2}{m^*}\Delta(\vec{r})\left.\frac{\partial\xi}{\partial z}\frac{\partial\xi'}{\partial z}\right|_{z=0,L}, \\ <|V(q)|^2> &\simeq \left(\frac{\hbar^2}{m^*}\right)^2 \frac{k_z^2}{Z}\frac{k_z'^2}{Z'}W(q), \end{aligned} \tag{5.7}$$

where $k_z \simeq N/Z$, $k_z' \simeq N'/Z'$ are the z-direction momenta of ξ and ξ', Z and Z' are the z-direction widths of the N-th and N'-th subbands, which are determined by the confinement. For example, when the subband N is electrostatically confined, $Z = \varepsilon_z/eE \simeq \hbar^2 k_z^2/m^* e^2 n \simeq a_B k_z^2/n$ (ε_z is the kinetic energy in z-direction), while when geometrically confined, $Z = L$. For Region VI, all subbands are geometrically confined. So

$$<|V(q)|^2> \simeq \left(\frac{\hbar^2}{m^*}\right)^2 \frac{N^2}{L^3}\frac{N'^2}{L^3}W(q). \tag{5.8}$$

Since in Region VI $k_F d \ll 1$, $W(q) \simeq \Delta^2 d^2$ is independent of q according to Eq. (5.3). The scattering is isotropic for a given subband N' with respect to different directions of $\vec{v}_{k'}$. The scattering rate is then reduced to

$$\frac{1}{\tau_N} = \frac{2\pi}{\hbar}\sum_{N'}\int\frac{d^2k'}{(2\pi)^2}\left(\frac{\hbar^2}{m^*}\right)^2 \frac{N^2N'^2\Delta^2d^2}{L^6\epsilon(q)^2}\delta(\varepsilon-\varepsilon_F). \tag{5.9}$$

The (2D) screening radius is $a_B/k_F L$ where $k_F L$ is the total number of subbands in Region VI. Since $L \ll a_B$ in this region, this screening radius is much larger than the Fermi wavelength $1/k_F$. So $\varepsilon(q) \approx 1$ and the screening can be ignored for the scattering between N-th subband and the typical subbands with $k_z' \simeq k_F$ and thus $q \sim k_F$. Eq. (5.9) then yields

$$\begin{aligned} \frac{1}{\tau_N} \simeq \frac{\hbar}{m^*}\frac{N^2\Delta^2d^2}{L^6}\sum_{N'}N'^2 &\simeq \frac{\hbar}{m^*}\frac{N^2\Delta^2d^2}{L^6}(k_F L)^3 \\ &\simeq \frac{\hbar}{m^*}\frac{N^2\Delta^2d^2k_F^3}{L^3} \end{aligned}, \tag{5.10}$$

where the 3D wavenumber $k_F = (n/L)^{1/3}$, and the scattering rate is mainly determined by scattering between the N-th subband and typical subbands with large N'. The absence of screening in the scattering rate calculation is then self-consistently justified.

Also, from Eq. (5.10), one can easily see that $\tau_N \propto 1/N^2$ so the lowest subband with $N = 1$ has the largest relaxation time while for typical subbands with $k_z \simeq k_F$ and, thus, $N \simeq k_F L$, the corresponding relaxation time is $(k_F L)^2$ times smaller. Since there are $\sim k_F L$ subbands in total with each subband having a 2D concentration $n/k_F L$ and the number of typical subbands is close to the total number $k_F L$, the final conductivity is dominated by the lowest subband as

$$\sigma = \frac{n}{k_F L}\frac{e^2}{\hbar}\frac{L^3}{\Delta^2 d^2 k_F^3} = ne\frac{e}{\hbar}\frac{L^2}{\Delta^2 d^2 k_F^4}, \tag{5.11}$$

and the effective mobility is

$$\mu = \frac{\sigma}{ne} = \frac{e}{\hbar}\frac{L^2}{\Delta^2 d^2 k_F^4} = \frac{e}{\hbar}\left(\frac{d^4}{\Delta^2}\right)\frac{L^{10/3}}{d^6 n^{4/3}}. \tag{5.12}$$

This is the result shown in Table 5.1 in Sec. 5.2.

Now let us move to Region IV. This region is a crossover between completely geometrically confined Region VI to completely electrostatically confined Region II. The lowest M subbands are electrostatically confined due to their relatively small distances to the surface while the $k_F L - M$ higher subbands are geometrically confined. So for the lowest M subbands, $k_z^2/Z \sim n/a_B$ is a constant independent of the subband index N determined only by the surface electric field E or the 2D electron concentration n. As a result, the lowest M subbands have comparable relaxation times. The rest $k_F L - M$ subbands are geometrically confined and their contribution to the conductivity is dominated by the lowest subband of the group, i.e., by the $(M+1)$-th subband. Here the index M is obtained by the condition that its electrostatically confined width is equal to the well width L

$$\frac{a_B k_z^2}{n} = L, \qquad k_z \simeq \frac{M}{L}. \tag{5.13}$$

As a result, $M = \left(nL^3/a_B\right)^{1/2}$. Now Eq. (5.10) is modified for subbands from 1 to M as

$$\begin{aligned}\frac{1}{\tau_{1-M}} \simeq & \frac{\hbar}{m^*}\frac{n\Delta^2 d^2}{a_B}\left(\sum_{N'=1,\ldots,M}\frac{n}{a_B} + \sum_{N'=M+1,\ldots,k_F L}\frac{N'^2}{L^3}\right) \\ \simeq & \frac{\hbar}{m^*}\frac{n\Delta^2 d^2}{a_B}\sum_{N'=M+1,\ldots,k_F L}\frac{N'^2}{L^3} \simeq \frac{\hbar}{m^*}\frac{n\Delta^2 d^2 k_F^3}{a_B},\end{aligned} \tag{5.14}$$

where $N'^2/L^3 \gg n/a_B$ for $N' > M$ and the total number of subbands is still $k_F L \gg M$ in Region IV. Therefore the scattering rate of each subband is always determined by its scattering into the typical subbands which are geometrically confined to a width L and have the momentum $k_z = k_F$ in the z-direction. One can easily check that in Region IV, i.e., at $L < n^{-1/5} a_B^{3/5}$, the conductivity is determined by the lowest M subbands and the effective mobility

$$\begin{aligned} \mu =& \frac{\sigma}{ne} = \left(M \times \frac{n}{k_F L} \frac{e^2}{m^*} \frac{m^*}{\hbar} \frac{a_B}{n\Delta^2 d^2 k_F^3} \right) \frac{1}{ne} \\ =& \frac{e}{\hbar} \left(\frac{d^4}{\Delta^2} \right) \frac{a_B^{1/2} L^{11/6}}{n^{11/6} d^6} \end{aligned} \tag{5.15}$$

is obtained in a way similar to that of Region VI discussed before. This is the result given in Table 5.1.

Now let us talk about the $k_F d \gg 1$ case for regions V and VII. In this case, $W(q)$ is no longer a constant but can be much smaller than $\Delta^2 d^2$ for some values of q. The scattering is no longer isotropic in the $x-y$ plane and one cannot ignore the DFR term $\vec{v_{k'}} \cdot \vec{E}\tau'_N / \vec{v_k} \cdot \vec{E}\tau_N$ in Eq. (5.6). As we show in Sec. 5.4, the scattering is dominated by events with $q \simeq k_F$ instead of small $q \lesssim 1/d$. It can be easily seen quasi-classically that only when an electron hits the sharp edge of an island can the non-specular reflection happen. This is an event on a length scale $k_F^{-1} \ll d$ so that the scattering is dominated by $q \simeq k_F$.

For the dominant large angle scattering, though the term $(1 - \vec{v_{k'}} \cdot \vec{E}\tau'_N / \vec{v_k} \cdot \vec{E}\tau_N)$ after averaging over different ϕ is not exactly unity like in the $k_F d \ll 1$ case, it is still of order unity. Thus in the scaling sense, the difference brought by $k_F d \gg 1$ is only in the $(k_F d)^3$ times reduction of $W(q)$. (One should note that for the large angle scattering, the rate is dominated by scattering into typical subbands of $k'_z \simeq k_F$ similarly to the $k_F d \ll 1$ case discussed before. The screening here is again ignored since the large angle scattering has $q \simeq k_F$ and the screening radius $a_B/k_F L$ is much larger than the electron Fermi wavelength k_F^{-1}, similarly to the case in regions IV and VI.) As a result, from Region IV to V, the scattering rate decreases by $(k_F d)^3$ for each subband and the effective mobility increases by $(k_F d)^3$. A similar increase by a factor $(k_F d)^3$ happens across the border from Region VI to Region VII. So far we have derived all the new results in Fig. 5.1 and Table 5.1.

One can see from Fig. 5.1 and Table 5.1 that the results of mobility in different regions match each other at all borders between the regions. Actually, using the derived result Eq. (5.12) for Region VI together with the results for regions II, III, and IX, which are already known, one can uniquely identify the mobility expressions in regions IV, V, and VII by matching them with the neighboring mobilities on the borders.

So far, we have been focused on the $d \ll a_B$ case, which is generic for large a_B semiconductors such as InAs and InSb. Now we would like to briefly discuss the $d \gg a_B$ case, which may take place, say, in silicon. Let us start from the case when $d = a_B$. In this case, the phase diagram Fig. 5.1 is dramatically simplified as the middle regions II, IV, and VI vanish and the border line $k_F d = 1$ merges with the vertical axis $na_B^2 = 1$. Let us now move to the case $d \gg a_B$. Since at $na_B^2 \ll 1$, the electron gas is two-dimensional for all values of L, there is only one line $nd^2 = 1$ for the critical border $k_F d = 1$. We assume that this line is located already in the insulator regime, so that in the whole metallic region $k_F d \gg 1$. This leads to an additional factor $(k_F d)^3$ to the mobility result in Region I and gives $\mu = (e/\hbar)\left(d^4/\Delta^2\right)\left(a_B^2/n^{1/2}d^3\right)$ (see Ref. [75]). Mobility results for the extended regions III, V, VII, and IX remain the same as in Table 5.1.

5.4 Large angle scattering dominance in scattering rate for quantum well

Here by using Eq. (5.6) we prove that the scattering rate in $k_F d \gg 1$ regions V and VII is dominated by the large angle scattering, i.e, scattering events with large $q \simeq k_F$. One might expect that because the correlator $W(q) \sim \Delta^2 d/(k_F d)^3$ for large angle scattering with $q \sim k_F$ is much smaller than that for scattering into small angles with $q \sim 1/d$ by a factor of $(k_F d)^3$ in the denominator, that the scattering is dominated by the small angle regime. However as we show below, the limited number of final subbands that electrons can scatter into for $q \leq 1/d$, the small value of the angular integral $\int d\phi \left(1 - \vec{v_{k'}} \cdot \vec{E}\tau_{N'}/\vec{v_k} \cdot \vec{E}\tau_N\right)$, and in certain cases the smaller z-direction momentum of final states $k_z' \ll k_F$ act to suppress the small angle scattering rate so that the scattering is determined by the large angle scattering. We show this below for three cases: $L < d$ (in some part of regions V and VII); $L > d$ and $M/L < 1/d$ (for the rest of

Region V and some part of Region VII); $L > d$ and $M/L > 1/d$ (for the rest of Region VII).

First let us consider the case when $L < d$. From energy conservation, the total magnitude of the momentum is fixed, and so any difference in magnitude of the in-plane momenta follows from the difference $|k_z - k_{z'}| \sim 1/L$ of their z-momentum. When $L < d$, $q \leq 1/d \ll 1/L$ and the scattering happens only within the same subband. This means that the DFR term $v_{\vec{k}'} \cdot \vec{E}\tau'_N / v_{\vec{k}} \cdot \vec{E}\tau_N$ reduces to the usual $\cos\phi$ for 2D scattering, where ϕ is the angle between $v_{\vec{k}'}$, $v_{\vec{k}}$. The final angular integral for the small angle scattering is $\int (1 - \cos\phi) d\phi \sim \phi^3 \sim (k_F d)^{-3}$, while it is of order unity for the large angle one. This cancels the advantage of larger $W(q)$ in the small angle scattering. Moreover, the small angle scattering has only one final subband to scatter into while the large angle scattering covers all $k_F L$ subbands. This combined with the small angular integral means that the small angle scattering rate is $k_F L \gg 1$ times smaller than that of the large angle when $L < d$.

Now let us look at the second case where $L > d$ and $M/L < 1/d$. For simplicity, we focus on the lowest subbands with $k_z < M/L \ll k_F$ as these dominate the conductivity in regions V and VII. In the limit $L > d$ and $M/L < 1/d$, there will always exist $L/d > M$ subbands with $k'_z < 1/d$ so that the scattering now involves intersubband scattering. As a result the DFR term is not reduced to $\cos\phi$ and the term $\left(1 - v_{\vec{k}'} \cdot \vec{E}\tau_{N'} / v_{\vec{k}} \cdot \vec{E}\tau_N\right)$ is of order unity instead of being infinitesimal for small q and thus small ϕ. The angular integral of this term would just give $1/(k_F d)$ from the small angle $\int d\phi \simeq 1/dk_F$ and does not compensate the $(k_F d)^3$ reduction of the correlator. However, we must consider the importance of k'_z in the scattering matrix element according to Eq. (5.7). For the small angle scattering $k'_z < 1/d$, while for the large angle regime $k'_z \sim k_F$. This gives an extra factor $1/(k_F d)^2$ to $|V(q)|^2$ in small angle regime relative to the large angle scattering. This additional factor combined with the small angular integral compensates the $1/(k_F d)^3$ reduction of the correlator. Considering also the accessible number of final subbands L/d in the small angle limit is $k_F d$ times smaller the $k_F L$ available subbands for large angle scattering, we find that the small angle scattering rate is $k_F d$ times smaller than that of the large angle.

Finally we must consider the intermediate case when $L > d$ and $M/L > 1/d$. For small angle scattering the number of subbands L/d that may be scattered into is small,

and so we expect that the DFR term is near the 2D limit $\cos\phi$. Expanding around this value, we find that the DFR term is approximately

$$\frac{\vec{v_{k'}} \cdot \vec{E}\tau'_N}{\vec{v_k} \cdot \vec{E}\tau_N} = \cos\phi(1 - \frac{\delta v_k}{v_k} - \frac{\delta\tau_N}{\tau_N}), \tag{5.16}$$

where $\delta v_k = |v_k - v'_k|$ and $\delta\tau_N - |\tau_N - \tau'_N|$. Let us examine these correction terms, beginning with $\delta v_k/v_k$. The allowed difference in k and k' is $1/d$ for the small angle scattering. Since $k \simeq k_F$ for lowest subbands, the velocity difference ratio $|v_{k'} - v_k|/v_k = |k' - k|/k$ is then $1/k_F d$. In considering the other correction term $\delta\tau_N/\tau_N$, let us assume that the scattering rate of each subband is always determined by their large angle scattering into typical subbands and show that this assumption self-consistent. With this assumption the difference in relaxation times $\delta\tau_N$ is solely caused by the different z-direction momenta and subband widths as seen from Eq. (5.7). Again we focus on the the lowest M subbands as these determine the conductivity. For the bottommost subbands, all subbands within $q \sim 1/d$ are electrostatically confined and $\delta\tau_N = 0$ as $k'^2_z/Z' = k_z^2/Z = n/a_B$ (see Eq. (5.7)) For the higher subbands with $k_z \sim M/L$, there are bands within $q \sim 1/d$ which are instead geometrically confined and the correction is non-vanishing. Indeed, we find that $\delta\tau_N \sim \tau_N \delta k_z/k_z$ and so the correction is given by $(1/d)/(M/L)$. We find then that the leading contribution to the DFR term in Eq. (5.16) in the small angle regime is approximately $1 - (1/d)/(M/L)$, where we have used the fact that $1/(k_F d) \ll L/Md$ in the limits being considered.

Using the DFR term above, the angular integral now gives a factor $(1/k_F d)(1/d)/(M/L)$ to the scattering rate, while the integral is of order unity for the large angle limit. Combined with the fact that the final state in the small angle regime has $k'^2_z/Z' \simeq (M/L)^2/L$, we find that these terms give an extra factor $(Md/L)/(k_F d)^3$ compared to the same terms for the large angle limit. We see then that there is a factor of $1/(k_F d)^3$ term that compensates the suppression of the correlator in the large angle limit. Adding the fact that the small angle scattering can only scatter into $L/d \ll k_F L$, we find that the ratio of scattering rates in the small and large angle regimes is $M/(k_F L) \ll 1$ and indeed the large angle limit dominates.

5.5 Roughness Limited Mobility in Quantum Wires

In the previous sections, we described the roughness limited mobility in a quantum well as a function of the 2D electron concentration n and the well width L. Here we would like to generalize these results to that of a nanowire with linear electron concentration η and radius R. We assume that an electric field $E = 2e\eta/R$ applied radially inward at surface of the wire. Such a system can be realized by a metallic gate surrounding the nanowire, or a planar gate located a distance larger than the wire radius R.

Our results are summarized in Fig. 1.6 as a "phase diagram" in the plane (η, R), where each "phase" or region marked by a capital letter denotes a different dependence of the mobility on R and η as shown in Table 1.1. Just as for quantum wells, many different regions appear due to the interplay between the electrostatic and geometric confinements. The electronic structure of each region is illustrated with a radial level (subband) schematic similar to those in Fig. 5.1. One can divide all regions into three groups. In regions D and G the electron gas is strictly one-dimensional (1DEG), i.e. it occupies a single subband in the wire cross-section. In Region A electrons occupy a single radial subband and many azimuthal subbands (2DEG). Finally, in regions B, C, E, F, H, and I, electrons occupy many subbands in both the radial and azimuthal directions and the gas is three-dimensional (3DEG). In order to clarify the meaning of the level schematics, Fig. 5.2 provides an illustration of the electronic structure in the 3DEG regions. Each top image shows the electron density (shaded regions) in a cross section of the wire while its bottom image shows the corresponding level schematic along the wire diameter.

Let us first concentrate on the 2DEG and 3DEG regions, where the circumference $2\pi R$ is much larger than the typical electron wavelength k_F^{-1}. This means that we can generalize our results of the quantum well by treating the wire along the x axis as a stripe-like quantum well whose y-direction size is $2\pi R$ and 2D concentration $n = \eta/2\pi R$. As a result each of the regions I-VII of Fig. 5.1 has an analogous region in Fig. 1.6 in which the electronic structure near the surface and the mobility are the same upon substituting $n = \eta/2\pi R$ and $L \simeq R$ everywhere. For example, in Region B electrons are confined electrostatically near the wire surface and form an accumulation layer (see Fig. 5.2(a)) whose thickness is given by Eq. (5.5) with $n = \eta/2\pi R$, similar to region II

for the quantum well. By using the correspondence between regions A, C, E, F, H, and I of Fig. 1.6 with regions I, III, IV, V, VI, and VII of Fig. 5.1 we find the wire mobility values for each of these regions as listed in Table 1.1.

So far we have shown that in the 2DEG and 3DEG limits of the nanowire, there is a corresponding region in Fig. 5.1 from which the mobility of the wire may be obtained upon substituting $n = \eta/R$. In regions D and G however, the electron gas in the wire forms a 1DEG for which there is no corresponding region in the quantum well. Let us first concentrate on Region G, where the gas is geometrically confined to a single subband in the plane of its cross-section (y, z) with energy $E_R = \hbar^2/2m^*R^2$ and its wavelength along the wire axis is $k_F^{-1} = \eta^{-1}$. Here y is the azimuthal direction along the wire circumference and z is the radial direction. Due to the roughness, the radius of the wire varies along the wire surface in the x and azimuthal directions by an amount $\delta R = \Delta(k_F^{-1}R/d^2)^{-1/2}$, where $k_F^{-1}R/d^2$ is the typical number of islands over which the electron averages the roughness. These variations lead to a change in the confinement energy that acts as a random scattering potential given by $V = E_R(\delta R/R)$. Using $\hbar/\tau \approx V^2/(\hbar^2 k_F^2/2m^*)$ to estimate the scattering rate, we find the mobility in Region G to be

$$\mu = \frac{e}{\hbar}\frac{\eta R^7}{\Delta^2 d^2}. \tag{5.17}$$

If we increase R so that we enter Region D, the electron gas is instead confined electrostatically to a single subband of width $D_0 = (a_B R/\eta)^{1/3}$. This change amounts to replacing R by D_0 in the confinement energy E_R. The mobility can thus be obtained by replacing the R^6 factor in Eq. (5.17) by $D_0^6 = a_B^2 R^2/\eta^2$ and so the mobility in Region D is given by

$$\mu = \frac{e}{\hbar}\frac{a_B^2 R^2}{\eta^2 \Delta^2 d^2}(\eta R) = \frac{e}{\hbar}\frac{a_B^2 R^3}{\eta \Delta^2 d^2}. \tag{5.18}$$

The factor ηR is unchanged as this came from averaging over an area $k_F^{-1}R$ on the surface and was independent of the confinement in the radial direction. The mobility values given in Eqs. (5.17) and (5.18) are shown in Tab. 1.1.

We can make the previous discussion more rigorous by considering the scattering rate using Fermi's golden rule. In the 1DEG limit there is only one radial or azimuthal

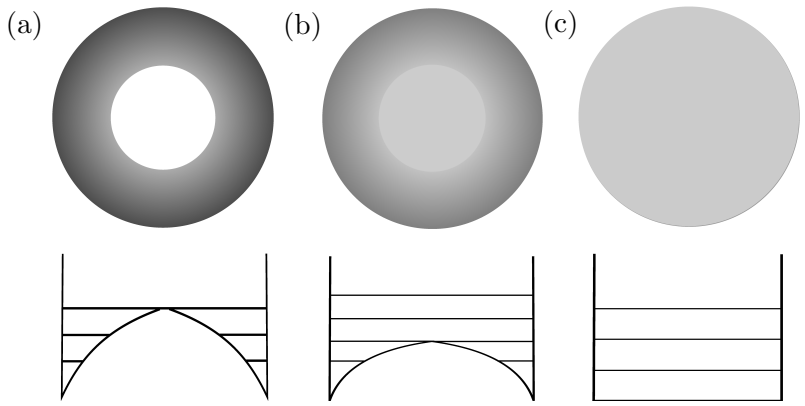

Figure 5.2: Electron concentration within the nanowire (top) and the corresponding level schematic along the diameter (bottom). Regions of higher concentration correspond to darker shading. a) Regions B and C of the scaling "phase diagram" Fig. 1.6, where all subbands are confined electrostatically forming an accumulation layer of thickness D near the surface. b) Regions E and F, where the lowest subbands are confined electrostatically, while the top subbands are confined geometrically. c) Regions H and I, where all the subbands are confined geometrically.

subband occupied so that the scattering rate given by Eq. (5.6) then simplifies to

$$\begin{aligned}\frac{1}{\tau} =& \frac{2\pi}{\hbar}\frac{1}{R}\sum_{k_y'}\int\frac{dk_x'}{2\pi} < |V(q)|^2 > \delta(\varepsilon_F - \varepsilon') \\ =& \frac{2\pi}{\hbar}\frac{1}{R}\int\frac{dk_x'}{2\pi} < |V(q)|^2 > \delta(\varepsilon_F - \varepsilon').\end{aligned} \tag{5.19}$$

Here the marginal one-dimensional screening is ignored and $< |V(q)|^2 >$ is defined to be

$$< |V(q)|^2 > \simeq \left(\frac{\hbar^2}{m^* Z^3}\right)^2 W(q) \tag{5.20}$$

for the gas confined to the lowest radial subband where $W(q) = \Delta^2 d^2$ at $k_F d \ll 1$. Setting $Z = R$ in region G and $Z = D_0$ in Region D, we arrive at the mobilities given by Eqs. (5.17) and (5.18).

We see in Fig. 1.6 that Region G is located at small R and small η, and extends until the line $R = d$. Beyond this point, the characteristic size of the islands d becomes larger than the radius of the wire R and the model of isotropically distributed islands on the wire surface breaks down.

So far we have dealt with the mobility of quantum wires that are cylindrically symmetric. A stripe-like wire along the x-axis can be made out of a narrow single subband GaAs/AlGaAs quantum well by the etching or split-gate techniques [155]. The mobility of such a modulation-doped stripe of 2DEG was calculated [71] for $k_F d \ll 1$ under the assumption that all scattering happens on the one-dimensional rough $y = 0$, R edges of the stripe and that the stripe has many y-direction subbands filled. Although our undoped wires studied in regions H and I are different from wires of Ref. [71], they share an important feature with them, i.e., the conduction is determined by the lowest subband. This can be easily understood quasiclassically, as the lowest subband electrons have most of its kinetic energy in the x-direction and run approximately parallel to the surfaces or edges, and thus get rarely scattered.

5.6 Ballistic-Diffusive Boundary and the Conductance of a Wire with Length $\mathcal{L}$

In the Introduction we explained that due to the 1D nature of the wire the transport properties differ greatly across the different regions of Fig. 1.6. Specifically, in the multisubband regions the wire of characteristic size R undergoes a transition between a ballistic conductor and a diffusive metal as a function of concentration. We will now explain why such a transition occurs, and calculate the conductance G within these regions.

Let us first review what we know about the Drude conductance and show where it fails. In Tab. 1.1 we give the Drude mobility for the various regions of Fig. 1.6. Using these formulas one can calculate the dimensionless Drude conductance $G_D = (h/e)\eta\mu/\mathcal{L}$ per spin for a wire with length $\mathcal{L}$ and linear concentration η. One can then define the metal-insulator transition by the condition $G_D = 1$. For example, in region H we find that $G_D = R^{14/3}/(\eta^{1/3} R_c(\mathcal{L})^5)$, where $R_c(\mathcal{L}) = (\Delta^2 d^2 \mathcal{L})^{1/5}$ is defined in the Introduction. Using the requirement $G_D = 1$, we find the MIT border within Region H to be $R_{MI}(\eta) = \eta^{1/14} R_c(\mathcal{L})^{15/14}$. Similar calculations for regions G, E, and B lead to the $R_{MI}(\eta)$ in Tab. 5.2.

The dimensionless Drude conductance is valid in all regions where $G_D > 1$, but the mean free path $l < \mathcal{L}$. In Region G where there is a single subband occupied,

Table 5.2: Metal-insulator border $R_{MI}(\eta)$, ballistic-diffusive border $R_{BD}(\eta)$, and the total number of subbands K_{max} for regions G, H, E, and B of Fig. 1.6

Region	$R_{MI}(\eta)$	$R_{BD}(\eta)$	K_{max}
G	$\eta^{-2/7}R_c(\mathcal{L})^{5/7}$	-	1
H	$\eta^{1/14}R_c(\mathcal{L})^{15/14}$	$\eta^{2/13}R_c(\mathcal{L})^{15/13}$	$(\eta R)^{2/3}$
E	$a_B^{-3/22}\eta^{5/22}R_c(\mathcal{L})^{15/11}$	$a_B^{-3/7}\eta^{5/7}R_c(\mathcal{L})^{15/7}$	$(\eta R)^{2/3}$
B	$a_B^{-8/11}\eta^{6/11}R_c(\mathcal{L})^{25/11}$	$a_B^{-7/9}\eta R_c(\mathcal{L})^{25/9}$	$\eta^{3/5}R^{2/5}a_B^{1/5}$

$G_D = 1$ and $l = \mathcal{L}$ are the same as long as $\eta a_B > 0.5$ where we can safely ignore electron-electron interactions. However in the multisubband regions B, H, and E the conditions are different. This can be understood by realizing that the condition $G_D = 1$ is equivalent to $\zeta = \mathcal{L}$, where ζ is the localization length. When multiple subbands are occupied, ζ grows larger than l, so in the multisubband region we can satisfy the conditions $l \ll \mathcal{L} \ll \zeta$ required for diffusive transport.

Let us begin with the simplest Region B where all subbands have the same l. We define the mean free path as $l = v_F\tau$, where τ is the relaxation time and $v_F = \hbar k_F/m^*$ is the Fermi velocity. The relaxation time τ can be calculated from the mobility in Tab. 1.1 and we find that in Region B

$$l = \frac{a_B^{7/5}R^{9/5}}{\Delta^2 d^2 \eta^{9/5}}, \tag{5.21}$$

The border equation is defined by the condition $l = \mathcal{L}$ and is found to be

$$R_{BD}(\eta) = \frac{\eta R_c(\mathcal{L})^{25/9}}{a_B^{7/9}} \tag{5.22}$$

as shown in Tab. 5.2.

In regions E and H there are radial subbands which are geometrically confined. As we showed in Sec. 5.3, subbands that are geometrically confined will have different relaxation times, with higher subbands having smaller relaxation times. As a result G_D

in these regions is determined by the lowest radial subbands where τ and l are largest. In Region E the bottom M radial subbands are confined electrostatically, while the higher subbands are confined geometrically. Similar to Region B the subbands that are electrostatically confined have the same mean free path

$$l_{1-M} = \frac{a_B R^{7/3}}{\Delta^2 d^2 \eta^{5/3}}. \tag{5.23}$$

These are the lowest subbands that determine G_D and thus setting $l_{1-M} = \mathcal{L}$ leads to $R_{BD}(\eta)$ in Tab. 5.2.

Finally, in Region H all radial subbands are geometrically confined and therefore have different mean free paths. The mean free path of the Nth subband l_N is given by

$$l_N = \frac{R^{13/3}}{\Delta^2 d^2 \eta^{2/3} N^2}. \tag{5.24}$$

We see that $l_N \propto N^{-2}$ and the conductance is determined by the lowest radial subband where $N = 1$. We can define the diffusive border by the condition that $l_1 = \mathcal{L}$, leading to the border equation in Tab. 5.2.

Let us now use these results to determine the number K of ballistic subbands at the border. Recall that in the ballistic regions, the dimensionless conductance of the wire is $G_B = K$. At the border $G_B = G_D$, and so using our results of the Drude conductance we can self consistently find the number of ballistic subbands. In Region H, we find $K = k_F R$, in Region E we find that $K = M k_F R$, and in Region B we find that $K = k_F^2 R D$, where D is given by Eq. (5.5) with $n = \eta/R$. These results can be easily understood. For each radial subband there are $k_F R$ azimuthal subbands that contribute equally to the conductance. Then we can generically set $K = (k_F R) K_r$ where K_r will be the number of ballistic radial subbands at the border. In Region H only one radial subband is ballistic, in Region E there are M ballistic radial subbands, and finally in Region B there are $k_F D$ radial subbands which are ballistic. Beyond the border K_r increases as $(l_1/L)^{1/2}$ until K reaches the total number of subbands given in Tab. 5.2, where l_1 is given by Eq. (5.24) for $N = 1$. The condition $K_r = k_F R$ defines a final border

$$R(\eta) = \eta^{4/11} R_c(\mathcal{L})^{15/11} \tag{5.25}$$

in regions H and E, beyond which all subbands are ballistic.

5.7 Variable Radius Model of a Nanowire

Previously, we have considered a model of the surface roughness as flat islands of size $d \ll R$ and height Δ randomly distributed over the surface of the crystal. For the case of the nanowire however, one can imagine another model of roughness in which the radius of the wire varies along its length, but is independent of the azimuthal direction. We may consider these variations as ring like steps of typical length d and thickness Δ. The step-like nature of the roughness means that we can describe this new model from our old one by restricting the spatial correlator given in Eq. (5.3) to variations in the x-direction. The corresponding Fourier transform of the correlator is then given by

$$W(q_x, q_y) = 2\sqrt{2}\pi\Delta^2 d(1 + q_x^2 d^2/2)^{-1}\delta(q_y) \tag{5.26}$$

where q_x is the momentum along the wire's length and q_y is the momentum in the azimuthal direction. We call this model the Variable Radius Model (VRM).

The new phase diagram for the VRM is shown in Fig. 5.3. It should not be surprising that most of the regions and borders are identical to those in Fig. 1.6, as these are set either by the number of subbands occupied, the type of confinement, or comparison between the island size d and the wavelength k_F^{-1}. As none of these properties depend on the details of the correlator, the regions and borders remain the same as Fig. 5.3. However, there is a new region J' that emerges in Fig. 5.3 that did not appear in Fig. 1.6. This region is the geometrically confined 1DEG under the condition $k_F d \gg 1$. We see that this region occurs in the limit $R \ll d$, which was forbidden for the previous model of roughness. No such restriction is necessary for the VRM, and so the new region emerges.

The mobility of these regions are given in Tab. 5.3. We notice immediately that the mobility expressions in regions C′, F′, and I′ are identical to the same lettered regions in Fig. 1.6. The reason is that in these regions, $k_F d \gg 1$, and the scattering is dominated by large angle scattering at the edge of a single island, rather than an effect averaged over many islands. The lack of averaging eliminates the differences between the two models in this region, and so the mobility expressions are the same. When $k_F d \ll 1$, the electrons feel instead an averaged effect, and so we see differences emerge between the two models. The effect of averaging results in a reduction of the scattering rate by the number of scattering centers which are typically seen. In the model considered

previously, the variations are two-dimensional and so the electrons average along both the x-direction and the azimuthal direction. This leads to an average number of islands that contribute to scattering given by the factor $1/(k_F d)^2$ in the 2DEG and 3DEG regions, and $R/(k_F d^2)$ in the 1DEG limit. In the VRM the variations only occur in the x-direction and so we do not average in the azimuthal direction. This reduces the number of islands averaged over to be $1/(k_F d)$ in all regions. Knowing this, we may easily obtain the new mobilities of most regions by multiplying the expressions in Tab.1.1 by the ratio of the new number of islands to the old number of islands. This ratio is $k_F d$ in the 2DEG and 3DEG and d/R in the 1DEG. The results are shown in Tab. 5.3.

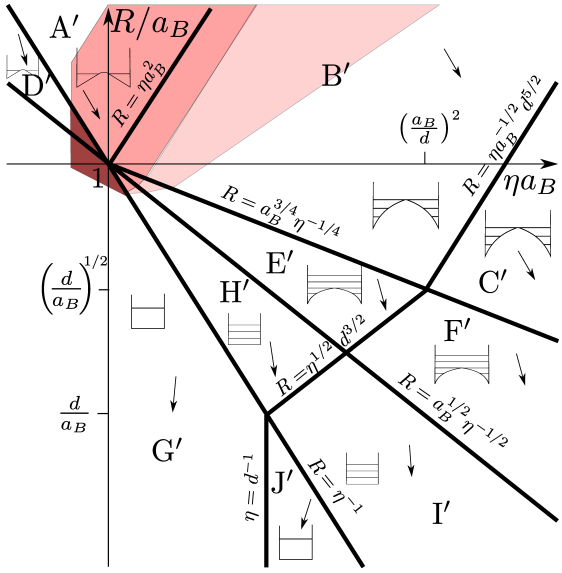

Figure 5.3: The scaling "phase diagram" of roughness limited electron mobility of a quantum wire for the Variable Radius Model (VRM) plotted as a function of radius R and linear electron concentration η for $d < a_B$ in the log-log scale. Different "phases" or regions are denoted by capital letters. Mobility expressions corresponding to these regions are given in Table 5.3. Region boundaries are given by the equations next to them. The schematic self-consistent electron potential energy profile along the the wire diameter and subbands occupied by electrons are shown for each region. All regions and the borders have the same definitions as Fig. 1.6, with the exception of a new region J′ that was previously forbidden.

While we can understand the changes in mobility in the VRM as due to a difference

Table 5.3: Mobility μ in units of $(e/\hbar)\left(d^4/\Delta^2\right)$ as a function of the linear electron concentration η at $d < a_B$ for different regions of Fig. 5.3.

A′	B′	C′
$a_B^2 R^{3/2}/\eta^{3/2} d^5$	$a_B^{7/5} R^{9/5}/d^5 \eta^{9/5}$	$a_B R/\eta d^3$
D′	E′	F′
$a_B^2 R^2/\eta d^5$	$a_B^{1/2} R^3/\eta^{3/2} d^5$	$a_B^{1/2} R^{5/3}/\eta^{5/6} d^3$
G′	H′	I′
$R^6 \eta/d^5$	$R^4/\eta d^5$	$R^{8/3}/\eta^{1/3} d^3$
—	—	J′
—	—	$\eta^3 R^6/d^3$

in averaging, we may also derive these changes from the correlator in Eq. (5.26). All the differences between the two models occur in the regions where $k_F d \ll 1$, where the correlator is simply $\sqrt{2}\Delta^2 d\delta(q_y)$. We see that the major difference from Eq. (5.3) is that $d^2 \to d\ \delta(q_y)$, and so it must be true that this difference is what is responsible for the change in the mobility between the two models. Indeed, when calculating the scattering rate, we integrate the correlator over the possible final states k', so that it appears in the scattering rate as a factor $\int d^2k' W(q)$. In our previous model this provided to the scattering rate an overall factor of $k_F^2 \Delta^2 d^2$ for the 2DEG and 3DEG regions, and $k_F \Delta^2 d^2/R$ in the 1DEG. In the VRM the presence of a delta-function for the azimuthal momentum means that these factors change to $k_F \Delta^2 d$ in all regions. From here it is clear that the change in the correlator leads to a difference in the mobility between the two models by a factor of $k_F d$ in 2DEG and 3DEG regions and d/R in the 1DEG regions as we described above.

We have shown that all regions in Fig. 5.3 can be obtained from Fig. 1.6 except for the region J′. In this region $k_F d \gg 1$, where the scattering rate is determined by large

angle scattering. As was discussed in Sec. 5.3, the large angle scattering reduces the correlator, and thus the scattering rate, by a factor of $(k_F d)^3$ in the denominator. This allowed us to obtain the mobility for $k_F d \gg 1$ from the corresponding region with $k_F d \ll 1$ by multiplying the expression by the factor $(k_F d)^3$. The same logic may be applied in the VRM, but with a small change. The correlator for the VRM has a different power in the denominator than the previous model. The large angle scattering then reduces the correlator by a factor of $(k_F d)^2$ in the denominator, rather than $(k_F d)^3$. This means that we may obtain the mobility of J′ from that of G′ by multiplying by the factor $(k_F d)^2 = (\eta d)^2$, and this value is shown in Tab. 5.3.

The results presented in Sec. 5.6 about the conductance and ballistic-diffusive border can easily be generalized to the VRM model. As the results are quite similar, we do not repeat the discussion here.

5.8 Discussion

Here we would like to estimate the critical value $R_c(\mathcal{L})$ in which the metallic window opens for InAs and InSb nanowires. In order to obtain an accurate estimate of $R_c(\mathcal{L})$, we first need the proper numerical coefficient beyond the scaling approach. Fortunately, the simple single subband structure of regions G and G′ allows this number to be determined analytically if we ignore electron-electron interactions. We have calculated these coefficients for a cylindrical wire in Appendix A and found that the mobility in Region G of the isotropic model is

$$\mu = 0.047 \frac{e}{\hbar} \frac{\eta R^7}{\Delta^2 d^2}, \tag{5.27}$$

while for Region G′ of the VRM we find the mobility to be

$$\mu = 0.017 \frac{e}{\hbar} \frac{\eta R^6}{\Delta^2 d}. \tag{5.28}$$

$R_c(\mathcal{L})$ is defined to be the radius in which the dimensionless conductance $G = 1$. Using Eqs. (5.27) and (5.28), and assuming we are on the border $\eta R = 1$ between regions G and H (or G′ and H′), we find the value of $R_c(\mathcal{L})$ in the isotropic roughness model to be

$$R_c(\mathcal{L}) = 1.8(\Delta^2 d^2 \mathcal{L})^{1/5}, \tag{5.29}$$

while for the VRM we find

$$R_c(\mathcal{L}) = 2.8(\Delta^2 d\mathcal{L})^{1/4}. \tag{5.30}$$

Now let us see what our theory predicts for a wire with $\mathcal{L} = 1$ μm. If we assume that $\Delta = 1$ nm and $d = 10$ nm, then using Eq. (5.29) we find that $R_c(\mathcal{L}) = 18$ nm for the isotropic model, while using Eq. (5.30) for the VRM we find $R_c(\mathcal{L}) = 28$ nm. We see that $R_c(\mathcal{L}) < a_B$ in both InAs ($a_B \approx 34$ nm)[67] and in InSb ($a_B = 64$ nm)[156], so that the ballistic single subband region exists. Recent experiments[56] have demonstrated ballistic transport in InSb nanowires with $\mathcal{L} \leq 1$ μm and R in the range of $40 - 50$ nm. These R satisfy the condition $R_c(\mathcal{L}) < R < a_B$ from our estimates, and thus our theory is consistent with their observation of ballistic transport.

In the above estimate we used the condition $G = 1$ so that the conductance per spin was e^2/h. One could use a different condition in which $R_c(\mathcal{L})$ is defined to be the R such that $l = \mathcal{L}$. This different definition alters $R_c(\mathcal{L})$ by a factor 1.1 in the isotropic model and 1.2 in the VRM, and so our prediction for $R_c(\mathcal{L})$ is only slightly different between the two definitions.

5.9 Coefficients of Mobility for Geometrically Confined 1DEG in Cylindrical Nanowires in Region G and G′

In the Discussion, we have used the coefficient of the mobility and thus the mean free path of electrons in narrow nanowires of cylindrical cross-sections at low electron concentrations (Region G of Fig. 1.6 and G′ of Fig. 5.3). In this appendix, we derive this coefficient.

For a narrow nanowire at low electron concentrations, electrons occupy only the first subband in the wire cross-section forming a 1DEG which is geometrically confined. If we ignore correlation effects, the wavefunction of the lowest subband in a cylindrical nanowire of radius R is

$$\xi(r, \phi, x) = \frac{J_0(\nu_0 r/R)e^{ikx}}{\sqrt{\pi} R J_1(\nu_0)} \tag{5.31}$$

where x is directed along the wire axis, r is the distance from the wire center, ϕ is the azimuthal angle in the cross section of the wire, J_0 and J_1 are the zeroth and first order Bessel functions of the first kind, and $\nu_0 \approx 2.4$ is the first zero of J_0.

It can be easily derived that for a 1DEG, the scattering rate is

$$\frac{1}{\tau} = \frac{2\pi}{\hbar}|V|^2\rho(1-\cos\theta) \tag{5.32}$$

where $|V|$ is the scattering matrix element due to roughness, $\theta = \pi$ is the angle between initial and final electron momenta, $\rho = m^*/2\pi\hbar^2 k_F$ is the density of states into which the backscattering can happen, and k_F is the Fermi wavenumber of the 1DEG. For 1D scattering, only backscattering can cause momentum relaxation, and so the angle between the initial and final momenta is π.

Similar to Eq. (5.7), according to Ref. [1], one can obtain the scattering potential in the cylindrical geometry to be

$$V(\phi, z) = \frac{\hbar^2}{2m^*}\Delta(\phi, z)\left.\frac{\partial\xi}{\partial r}\frac{\partial\xi'}{\partial r}\right|_{r=R} \tag{5.33}$$

and the scattering matrix element for $R \gg d$ is

$$< |V(q)|^2 >= \frac{\nu_0}{2\pi}\frac{\hbar^4}{m^{*2}R^7}W(q) \tag{5.34}$$

where $q = 2k_F$ is the transferred momentum along the wire axis for backscattering of electrons at the Fermi level.

If we combine Eqs. (5.32) and (5.34), set $k_F = (\pi/2)\eta$ for a 1D gas, and use $k_F d \ll 1$ for the correlator given in Eq. (5.3), we find the mobility $\mu = e\tau/m^*$ to be

$$\mu = \frac{\pi}{2\nu_0^4}\frac{e}{\hbar}\frac{\eta R^7}{\Delta^2 d^2}. \tag{5.35}$$

If instead we consider the VRM model described in Sec. 5.7, then we use the correlator given in Eq. (5.26) instead. As a result, the mobility in Region G$'$ in the VRM is

$$\mu = \frac{\pi}{4\sqrt{2}\nu_0^4}\frac{e}{\hbar}\frac{\eta R^6}{\Delta^2 d}. \tag{5.36}$$

Chapter 6

Attraction of Interlayer Excitons in Van der Waals Heterostructures with Three Semiconducting Layers

6.1 Introduction

The contents of this chapter are a reproduction of Ref. [92]. In a standard parallel-plate capacitor, the capacitance C is equal to the "geometric capacitance" $C_g = \kappa S/4\pi d$ (in Gaussian units), where κ is the dielectric constant of the medium separating the two plates, S is the area of each plate, and d is the distance between them. The expression $C = C_g$ is correct when both electrodes are made from a "perfect" metal, which by definition screens the electric field with a vanishing screening radius. This condition fails if both sides of the capacitor are made of a layer of an intrinsic semiconductor and the applied voltage generates in them an equal small density n of a two-dimensional electron (2DEG) and hole (2DHG) gas. For example, one can think about two separately contacted monolayers of intrinsic $MoSe_2$ separated by a few hexagonal boron nitride (hBN) layers with total width d. If in both the 2DEG and the 2DHG $na_B^2 \ll 1$, where $a_B = \kappa\hbar^2/m^*e^2$ is the effective Bohr radius and m^* is its effective mass, electrons and

holes created in opposite $MoSe_2$ layers can be treated as classical point like particles. It was shown [142] that if in addition $nd^2 \ll 1$, the capacitor charge $Q = enS$ grows with V as $Q(V) \propto (V - V_1)^{2/3}$, where

$$eV_1 = E_g - E_{ex}, \tag{6.1}$$

is the critical voltage required to create a single isolated electron-hole pair in an intrinsic semiconductor, E_g is the bandgap of the semiconductor, and E_{ex} is the binding energy of the electron-hole pair. The differential capacitance $C(n) \equiv dQ/dV$ becomes much larger than C_g and grows as $0.37C_g/(nd^2)^{1/2}$ with decreasing n. As a function of V the capacitance $C(V) \propto (V - V_1)^{-1/3}$.

This anomalous capacitance growth near V_1 is due to the fact that each electron in the 2DEG is bound to a hole in the 2DHG of the other layer, forming an interlayer exciton with a dipole moment ed. At $nd^2 \ll 1$, parallel dipoles are separated from each other by a large distance. Therefore, their repulsion is weak and provides a weak resistance to further capacitor charging leading to a diverging capacitance as $V \to V_1$ from above. A similar anomalously large capacitance was predicted when one layer is replaced by a metallic plane[142]. A capacitance 40% larger than the geometrical value, which may be a result of this phenomena, was reported in YBCO/LAO/STO nanostructures[157]. A similar effect was predicted in graphene-metal capacitors placed in a strong perpendicular magnetic field which localizes carriers[158]. A capacitance that is 20% larger than the geometrical one was observed in this case[159].

The strong capacitance anomaly in the two-layer device is due to the discreteness of charge and their strong correlations at small densities n. In this paper we explore similar correlation physics in three-layer devices with a symmetry plane. For example, we may think about three monolayers of intrinsic $MoSe_2$ each of width w, separated by the same number of hBN layers of total width d_0 on each side, so that the structure is symmetric with respect to the central layer midplane. The symmetry is not only geometrical, but also includes the voltage contacts: if the central layer is contacted by the negative electrode, both external layers are contacted by the positive electrode. Correspondingly, an equal number of voltage induced interlayer excitons, each with a dipole moment $ed = e(d_0 + w)$, are directed from the central plane to the top and to the bottom (see Fig. 1.8a). At large distances along the plane, two antiparallel dipoles

attract each other, while at distances smaller than d they repel each other. It is natural to assume that as a result the dipoles form a two-dimensional antiferroelectric square lattice. This lattice is similar to NaCl, where Na-like and Cl-like sites are occupied by up and down pointing dipoles, i.e. all nearest neighbor dipoles are antiparallel (see Fig. 1.8b) . Electrons of the central plane form a square lattice with the lattice constant $n^{-1/2}$.

We show below that at low temperatures when the applied voltage V grows, the attraction between interlayer excitons in the three-layer device causes a first order phase transition (see Fig. 1.9). While at small V there are no dipoles and the capacitor remains uncharged, at some critical value $V = V_c < V_1$ the whole lattice of alternating dipoles emerges. This means that a macroscopic charge $Q_c = eSn_c$, where $n_c = 0.13d^{-2}$ and S is the device area, enters this capacitor. Thus, the differential capacitance C has a δ-peak at $V = V_c$. At $V > V_c$, as n continues to grow the capacitance slowly approaches its normal geometric value $2C_g$. The giant δ-peak of the capacitance at $V = V_c$ can be thought of as an enhanced version of the anomaly $C(V) \propto (V - V_1)^{-1/3}$ near $V = V_1$ predicted for a two-layer capacitor.[142] A similar δ-peak capacitance was predicted in a 3D nanocrystal film gated by an ionic liquid in which the ions penetrate between nanocrystals[160].

6.2 Capacitance of a Three Layer System

For a quantitative description of the three-layer capacitor we assume the density is such that $na_B^2 \ll 1$ so that we may treat all charges classically. The differential capacitance of such a device can be determined from the total electrostatic energy E of the system of classical charges

$$E = enSV_1 + nSU, \tag{6.2}$$

where V_1 is the voltage necessary to create a single isolated electron-hole pair and is given by Eq. (6.1), while U is the interaction energy per electron-hole pair in the system. We can further separate the interaction energy as $U = U_e + U_h$, where U_e is the contribution to U from the electrons interacting with all other charges, while U_h is the contribution to U from the holes interacting with all other charges. It should be clarified that in U_e and U_h we neglect the interaction between electrons and holes of the same pair. Assuming

the electrons and holes can be treated classically, the binding energy E_{ex} in Eq. (6.1) is given by $e^2/(\kappa d)$. Here and below we use the Coulomb potential with an effective dielectric constant $\kappa \simeq 5$ which is close to the dielectric constant of hBN. This effective medium potential was used in previous studies of electron-hole interactions in bilayer TMD heterostructures separated by several layers of hBN,[90] and is in contrast with the Rytova-Keldysh potential used for a single TMD layer in air. Its use for our system can be justified because the distance between neighboring dipoles $n_c^{-1/2}$ is much larger than the distance $2w$ at which the electric field lines spread over the entire structure. Here the factor 2 comes from the ratio of the dielectric constant of $MoSe_2$ and hBN, and w is the thickness of a monolayer of $MoSe_2$.

Each hole in an external plane pairs with an electron in the central plane in such a way that the orientation of the dipoles alternates between nearest neighbor sites of the electrons in the central plane square lattice, as shown in Fig. 1.8(b). Let us consider the electron-hole pair located at the central white site in Fig. 1.8(b). For the electron at the origin, we can write

$$U_e = \frac{1}{2}\sum_{\alpha\neq 0}\left(\frac{e^2}{\kappa r_\alpha} - \frac{e^2}{\kappa\sqrt{r_\alpha^2+d^2}}\right), \tag{6.3}$$

where α is an index labeling the electron lattice sites, $\alpha = 0$ is defined as the origin, and r_α is the distance between site α and the origin. The factor $1/2$ accounts for the double counting when computing the interaction energy U. For the hole that is also located at the origin, we can use the fact that the electron and hole form a dipole with a particular orientation (in this case upwards) to separate U_h as $U_h = U_{h1} + U_{h2}$. Here

$$U_{h1} = \frac{1}{2}\sum_{\alpha\neq 0}^{\circ}\left(\frac{e^2}{\kappa r_\alpha} - \frac{e^2}{\kappa\sqrt{r_\alpha^2+d^2}}\right), \tag{6.4}$$

is the contribution from the interaction of the hole with dipoles with the same orientation as the origin dipole (white sites), while

$$U_{h2} = \frac{1}{2}\sum_{\alpha\neq 0}^{\bullet}\left(\frac{e^2}{\kappa\sqrt{r_\alpha^2+4d^2}} - \frac{e^2}{\kappa\sqrt{r_\alpha^2+d^2}}\right), \tag{6.5}$$

is the contribution from the interaction of the hole with dipoles of the opposite orientation(black sites). The symbols next to the summation indicate that the sums are

restricted to the corresponding sublattice shown in Fig. 1.8(b). Upon inspection, it is clear that Eqs. (6.3) and (6.4) are similar so that we can write U as

$$U = \frac{e^2 n^{1/2}}{2\kappa}\left(g(nd^2) + \frac{1}{\sqrt{2}}g(nd^2/2) + h(nd^2)\right), \tag{6.6}$$

where

$$g(x) = 4\sum_{i=1}^{\infty}\sum_{j=0}^{\infty}\left(\frac{1}{\sqrt{i^2+j^2}} - \frac{1}{\sqrt{i^2+j^2+x}}\right), \tag{6.7}$$

and

$$h(x) = 4\sum_{i=1}^{\infty}\sum_{j=0}^{\infty}{}^{\bullet}\left(\frac{1}{\sqrt{i^2+j^2+4x}} - \frac{1}{\sqrt{i^2+j^2+x}}\right), \tag{6.8}$$

and we have rewritten the site index α using the integers i and j of the electron lattice coordinates in units of $n^{-1/2}$. For the summation over the black sublattice in Eq. (6.8), we restrict ourselves to values of i and j such that $i + j$ is odd. Both summations are convergent for any x. The results of this summation are shown by the red curve in Fig. 6.1 as a plot of $U/e^2/(\kappa d)$ vs nd^2. We see that the interaction energy is negative for a finite range of densities due to the attraction between nearest neighbor dipoles with opposite orientation. At $n_c d^2 = 0.13$ it reaches a minimum value of $U = -0.018e^2/\kappa d$. In order to better understand this, we compare this result to the energy obtained from only the nearest neighbor sites of each sublattice, shown by the labeled U_{NN} curve (blue curve) in Fig. 6.1. We see that for small nd^2 the energy is almost completely determined by these nearest neighbors, with significant deviation only appearing beyond the minimum of U.

Once the energy E is found, we can find the voltage as

$$V = V_1 + \frac{1}{e}\frac{d(nU)}{dn}. \tag{6.9}$$

Our main results were presented in Fig. 1.9 as a plot of the density nd^2 as a function of the voltage $(V - V_1)/(e/\kappa d)$. The dashed curve is obtained from Eq. (6.9). Most noticeable is that there is a range in which there are three densities for each voltage: a lower branch along $n = 0$, a middle branch, and an upper branch. Within the middle branch, the capacitance defined by Eq. (1.15) is negative and this region is thermodynamically unstable and is inaccessible. Thus in experiment, we do not expect the density to change continuously along the dashed curve, but instead along the curve shown in red

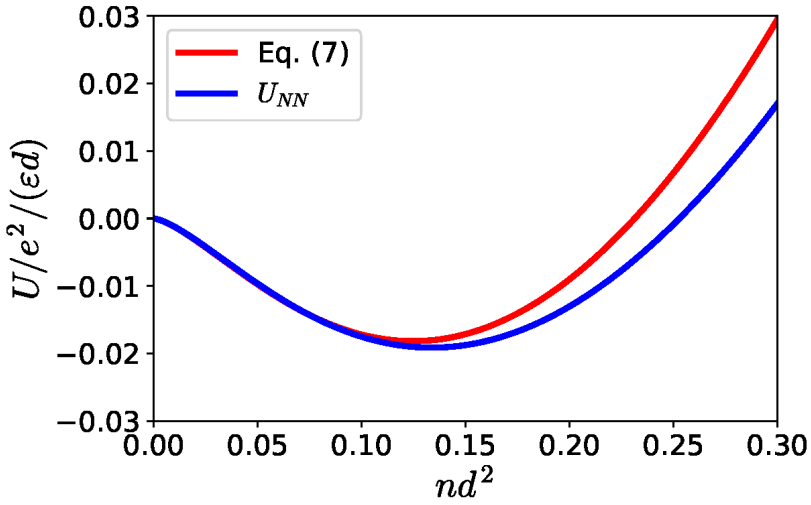

Figure 6.1: Dimensionless interaction energy $U/e^2/(\kappa d)$ vs the density nd^2. The red curve is obtained from Eq. (6.6), while the blue curve labeled U_{NN} is an approximation which only takes into account the nearest neighbor sites of each sublattice.

where the density jumps to a value $n_c = 0.13d^{-2}$ at a critical voltage $V_c = V_1 - 0.018\frac{e}{\kappa d}$. Here V_c is determined by Maxwell area rule[44]

$$\int_0^{n_c} n(V)dV = 0, \tag{6.10}$$

where the integral is taken along the dashed curve in Fig. 1.9. At $V = V_c$ the two regions lying between the vertical red line and the dashed curve have equal area. This rule is well known for the van der Waals liquid-gas pressure-volume isotherm. [1] It is worth noting that n_c obtained from Maxwell's area rule is the same n_c at which U reaches its minimum value. As the density abruptly jumps, there is a δ-peak in the capacitance at $V = V_c$. For $V \geq V_c$ we can write the capacitance as $C(V) = eSn_c\delta(V - V_c) + C_u(V)$, where the non-singular capacitance $C_u(V)$ is obtained by differentiating the upper branch of the $n(V)$ curve shown in Fig. 1.9 with respect to V and is shown in Fig. 6.2. As V approaches V_c from above, $C_u(V)$ grows as $(V - V_c + 0.01e/\kappa d)^{-1/2}$, and attains a very large maximum value $C_u(V_c) \simeq 30C_g$, where C_g is the geometrical capacitance of the capacitor formed by either the central and upper planes or the central and lower planes.

[1] In this analogy, n plays the role of volume while the voltage V plays the role of pressure.

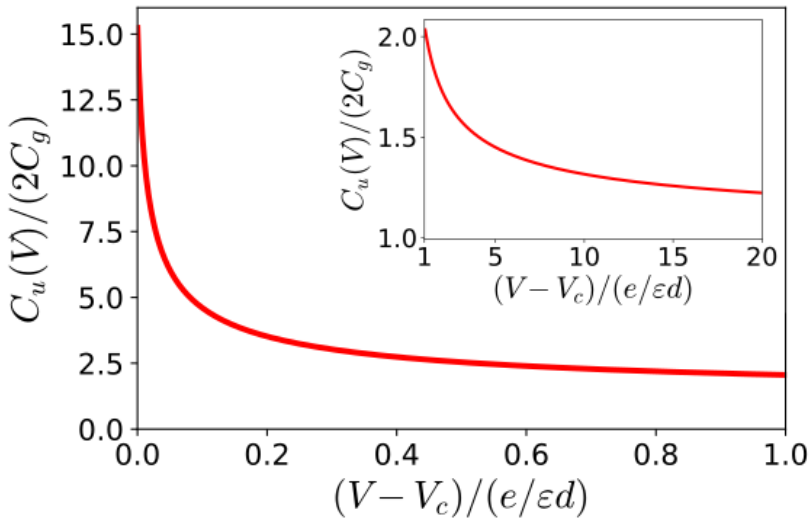

Figure 6.2: The dimensionless capacitance $C_u(V)/(2C_g)$ as a function of the dimensionless voltage $(V - V_c)/(e/\varepsilon d)$ corresponding to the upper branch of the red (solid) curve shown in Fig. 1.9. The inset shows $C_u(V)/(2C_g)$ over a 19 times larger range of $(V - V_c)/(e/\varepsilon d)$.

At larger voltages $V \gg e/\kappa d$ it approaches $2C_g$ corresponding to the geometric value of the three-layer system as shown in the inset of Fig. 6.2.

6.3 Discussion and Additional Examples

So far we have been dealing with very low temperatures and have ignored disorder. Temperature and disorder smear the δ-function as well as the low voltage peak of the non-singular large voltage tail of $C_u(V)$. When the width of the δ-function reaches $V_1 - V_c$, the two peaks in the capacitance merge to form a single peak. Because this happens at $C_u \simeq 30C_g$, a very large peak of the capacitance (much larger than in the case of two layers) survives in the presence of disorder or higher temperatures. It is easy to imagine that the measured capacitance peak is 5-10 times larger than the geometrical value. The reason for the early merging of the δ-function with the non-singular peak is that the optimal distance between electrons in the central plane $\sim n_c^{-1/2} \simeq 3d$ is relatively large and makes both the optimal energy and the voltage scale $(V_1 - V_c)$ of the dipole configuration in Fig. 1.9 relatively small. We can estimate the scale of

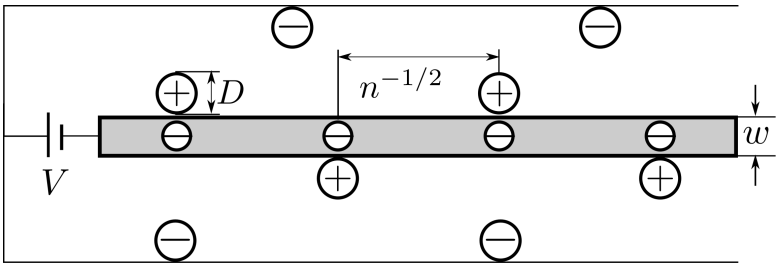

Figure 6.3: Schematic drawing of a TMD monolayer gated on both sides by an ionic liquid. A positive electrode immersed in the ionic liquid forces a concentration n of excessive positive ions to the surface of the TMD monolayer, while simultaneously attracting an equal concentration of excessive negative ions to the electrode surface (background ions of the net neutral ionic liquid are not shown). Each excessive positive ion binds an electron in the TMD, forming a dipole with arm length $(D + w)/2$. Similar to Fig. 1.8, the oppositely oriented dipoles attract each other and the electrons arrange in a square lattice of lattice constant $n^{-1/2}$.

temperature at which thermal fluctuations destroy the effect from the minimum in the interaction energy $U = -0.018e^2/\kappa d$ shown in Fig. 6.1. For $\kappa = 5$ and $d \simeq 1$ nm for a three layer thick hBN spacer, we find at $T \simeq 60$ K thermal fluctuations begin to dominate.

We have also ignored quantum effects. Typically the localization length ξ of electrons in the central plane can be comparable with d, so that quantum effects may modify the energy of the three-layer system at large enough n even at zero temperature and disorder. [90] However, even in such a case, at small n the energy of the electron-hole dipoles (excitons) is dominated by their dipole-dipole attraction and charging occurs by the first order transition. Quantum mechanics can still somewhat reduce n_c and $(V_1 - V_c)$. Quantum Monte-Carlo simulations similar to those in Refs. [161, 162, 163] are necessary to address these changes quantitatively.

Devices similar to those shown in Figs. 1.8 and 6.3 can be also made from graphene monolayers, however in this case the classical model leading to attraction between interlayer excitons becomes useful only in strong magnetic fields such that $nl_B^2 = n\hbar c/eB \ll 1$, where l_B is the magnetic length. In devices with $d \ll l_B$ this condition may substantially reduce n_c.

Three-layer devices made of $MoSe_2$ can face difficulties in making separate contacts to all three layers. Therefore, a similar device made of a single $MoSe_2$ monolayer gated

from both sides by an ionic liquid can be more attractive. In this case the dipoles are formed by electrons of the $MoSe_2$ monolayer bound to excessive positive ions, which stick to the monolayer in alternating positions above and below it (see Fig. 6.3). At small electron densities such a device is quantitatively similar to the three layer device described with a dipole moment $e(D + w)/2$, where D is the ionic diameter.

Above we talked about the capacitance of three-layer devices. Three-layer devices can be also used for optical studies of spatially indirect interacting excitons. It has been shown[88, 89] that in bilayer $MoSe_2/WSe_2$ structures, the type II band alignment of the $MoSe_2$ and WSe_2 monolayers allows the formation of interlayer excitons, in which an electron in $MoSe_2$ binds to a hole in WSe_2 (see Fig.1.10a). Because of the weak overlap of the electron and hole wavefunctions, these excitons decay slowly enough to form the ground state which minimizes their repulsion. In the photoluminescence experiments on the $MoSe_2/WSe_2$ device of Ref. [88], it was observed that the interlayer exciton luminescence line blueshifts as the intensity of the laser increases due to the dipole-dipole repulsion of the interlayer excitons. In a trilayer device,[164, 165] such as $WSe_2/MoSe_2/WSe_2$ (and similar devices with symmetric hBN spacers), we instead predict an attractive interaction between interlayer excitons formed from opposite WSe_2 layers (see Fig. 1.10b). At low illumination intensities these excitons condense into droplets of density n_c which do not interact with each other. These droplets are different from the exciton droplets in 3D semiconductors proposed by Keldysh and Kozlov[166]. Those droplets are formed by the van der Waals attraction between excitons and occurs when the excitons are at distances of order a. Our droplets are the result of the electrostatic dipole-dipole interaction and the excitons are separated by the larger than a distance $n_c^{-1/2}$ set by our classical theory. In such a device, the luminescence peak should be redshifted. [2] The luminescence line of excitons in these droplets should not change with the laser intensity until the intensity becomes so large that the droplets fill the entire sample.

[2] We can extrapolate the classical energy of a crystal of alternating dipoles to estimate the redshift as $0.02e^2/(\kappa d) \sim 6$ meV, where we have used $\kappa \simeq 7$ and $d = 7$ $\AA$ for monolayer TMDs[167]

Chapter 7

Conclusions and Discussion

In this thesis, we have examined the electronic properties of several different heterostructures. We have shown that even though all these structures support low dimensional electron gases, differences in geometry, heterostructure design, and material properties substantially alter the properties of this electron gas. The seemingly endless array of combinations one can create makes it crucial that we understand how individual material and design properties shape the electron gas, and it is the ultimate goal of this thesis to improve this understanding. We summarize the main results below.

In Ch. 2 we study the mobility and quantum mobility of modern AlGaAs/GaAs heterostructures. We find that the charged impurities in the sample are strongly screened by the excess electrons in the remote doping layers, a phenomena we refer to as excess electron screening. We derive analytical results for the mobilities, summarized in Eqs. (2.15), (2.16), and (2.31). This screening is responsible for the high mobility of these devices. Still, we find that the quantum mobility is substantially lower than ideal theoretical estimates, which may be due to significant disorder in the donor layers as shown by Fig. 1.2, or by the background impurities in the sample. Thus one should take care to make sure that the donor layers are as clean as possible, and then focus on the background impurities.

In Chs. 3 and 4, we study the accumulation layers in STO based heterostructures. We find that the properties of these accumulation layers are substantially altered due to the large dielectric constant in STO at liquid helium temperatures. In Ch. 3 we show that the nonlinear dielectric response results in a divergence of the magnetization and

specific heat of the accumulation layer. We study the truncation of these quantities (see Eqs. (1.8) and (3.16)) by the sample width, the dielectric constant, or back gate voltage, and show that these quantities can be enhanced by over an order of magnitude above their values in a uniform accumulation layer of size d. In Ch. 4 we study accumulation layers with a linear dielectric response in an ultrastrong magnetic field. The large dielectric constant of STO makes it easy to reach a quasi-one-dimensional state known as the extreme quantum limit (EQL) in which all electrons occupy the lowest Landau level. We find a phase diagram (see Fig. 1.4) for the accumulation layer which consists of a quasiclassical metallic phase, a metallic EQL phase, and an insulating Wigner crystal phase whose structure depends on the direction of the magnetic field (see Figs. 1.5 and 4.3). These effects can be measured through quantum capacitance measurements of the STO accumulation layer as shown by Fig. 4.4.

In Ch. 5, we study the roughness limited Drude mobility of quantum wires. We find the Drude conductance of the wire as a function of the linear concentration η has a sharp peak. The height of this peak grows as a large power of the wire radius R, so that at large R the conductance G_{max} exceeds e^2/h and a window of concentrations with delocalized states (which we call the metallic window) opens around the peak (see Fig. 1.7). We show that the scaling expression of the Drude mobility depends on the number of subbands occupied as well as the nature of the confinement (see Fig. 5.2), resulting in a complex phase diagram shown in Fig. 1.6. Results are also given for a quantum well, where it was previously shown that there is no metallic window.

The final Ch. 6 studies a capacitor made of three monolayers of transition metal dichalcogenide (TMD) separated by hexagonal Boron Nitride (hBN). We assume that the structure is symmetric with respect to the central layer plane. The symmetry includes the contacts: if the central layer is contacted by the negative electrode, both external layers are contacted by the positive one. As a result a strong enough voltage V induces electron-hole dipoles (indirect excitons) pointing towards one of the external layers. The attraction of antiparallel dipoles drives a first order transition, and we show that if V_1 is the critical voltage required to create a single electron-hole pair and charge this capacitor by e, the macroscopic charge $Q_c = eSn_c$ (S is the device area) enters the three-layer capacitor at a smaller critical voltage $V_c < V_1$ (see Fig. 1.9). We calculate n_c (see Eq. (1.17)) and V_c (see Eq. 1.18). The first order transition results

in a differential capacitance $C(V)$ that is infinite at $V = V_c$. We also show that in a contact-less three-layer device, where the chemically different central layer has lower conduction and valence bands, optical excitation creates indirect excitons which attract each other, and therefore form antiferroelectric exciton droplets. Thus, the indirect exciton luminescence is red shifted compared to a two-layer device.

References

[1] Tsuneya Ando, Alan B Fowler, and Frank Stern. Electronic properties of two-dimensional systems. *Rev. Mod. Phys.*, 54(2):437, 1982.

[2] L. Pfeiffer, K. W. West, H. L. Stormer, and K. W. Baldwin. *Appl. Phys. Lett.*, 55:1888, 1989.

[3] V. Umansky, R. de Picciotto, and M. Heiblum. Extremely high-mobility two-dimensional electron gas: Evaluation of scattering mechanisms. *Appl. Phys. Lett.*, 71:683, 1997.

[4] L. Pfeiffer and K. W. West. *Physica E*, 20:57, 2003.

[5] V Umansky, M Heiblum, Y Levinson, J Smet, J Nübler, and M Dolev. Mbe growth of ultra-low disorder 2deg with mobility exceeding $35\times\ 10^6$ cm^2/vs. *J. Crys. Growth*, 311(7):1658–1661, 2009.

[6] V Umansky and M Heiblum. Mbe growth of high-mobility 2deg. In *Molecular Beam Epitaxy*, pages 121–137. Elsevier, 2013.

[7] Michael J Manfra. Molecular beam epitaxy of ultra-high-quality algaas/gaas heterostructures: enabling physics in low-dimensional electronic systems. *Annu. Rev. Condens. Matter Phys.*, 5(1):347–373, 2014.

[8] Christian Reichl, Jun Chen, Stephan Baer, Clemens Rössler, Thomas Ihn, Klaus Ensslin, Werner Dietsche, and Werner Wegscheider. Increasing the $\nu= 5/2$ gap energy: an analysis of mbe growth parameters. *New Journal of Physics*, 16(2):023014, 2014.

[9] Geoffrey C Gardner, Saeed Fallahi, John D Watson, and Michael J Manfra. Modified mbe hardware and techniques and role of gallium purity for attainment of two dimensional electron gas mobility$> 35\times 10^6$ cm^2/v s in algaas/gaas quantum wells grown by mbe. *J. Cryst. Growth*, 441:71–77, 2016.

[10] D. C. Tsui, H. L. Stormer, and A. C. Gossard. Two-dimensional magnetotransport in the extreme quantum limit. *Phys. Rev. Lett.*, 48:1559, 1982.

[11] R. Willett, J. P. Eisenstein, H. L. Störmer, D. C. Tsui, A. C. Gossard, and J. H. English. Observation of an even-denominator quantum number in the fractional quantum hall effect. *Phys. Rev. Lett.*, 59:1776–1779, Oct 1987.

[12] A. A. Koulakov, M. M. Fogler, and B. I. Shklovskii. Charge density wave in two-dimensional electron liquid in weak magnetic field. *Phys. Rev. Lett.*, 76:499, 1996.

[13] M. P. Lilly, K. B. Cooper, J. P. Eisenstein, L. N. Pfeiffer, and K. W. West. Evidence for an anisotropic state of two-dimensional electrons in high landau levels. *Phys. Rev. Lett.*, 82:394, 1999.

[14] R. R. Du, D. C. Tsui, H. L. Stormer, L. N. Pfeiffer, K. W. Baldwin, and K. W. West. Strongly anisotropic transport in higher two-dimensional landau levels. *Solid State Commun.*, 109:389, 1999.

[15] Q. Shi, S. A. Studenikin, M. A. Zudov, K. W. Baldwin, L. N. Pfeiffer, and K. W. West. Microwave photoresistance in an ultra-high-quality gaas quantum well. *Phys. Rev. B*, 93:121305(R), Mar 2016.

[16] Q. Shi, M. A. Zudov, I. A. Dmitriev, K. W. Baldwin, L. N. Pfeiffer, and K. W. West. Fine structure of high-power microwave-induced resistance oscillations. *Phys. Rev. B*, 95:041403(R), Jan 2017.

[17] Q. Qian, J. Nakamura, S. Fallahi, G. C. Gardner, J. D. Watson, S. Lüscher, J. A. Folk, G. A. Csáthy, and M. J. Manfra. Quantum lifetime in ultrahigh quality gaas quantum wells: Relationship to $\Delta_{5/2}$ and impact of density fluctuations. *Phys. Rev. B*, 96:035309, Jul 2017.

[18] L. Shubnikov and W.J. de Haas. *Leiden Commun.*, 207a, 1930.

[19] M. A. Zudov, R. R. Du, J. A. Simmons, and J. L. Reno. Shubnikov–de haas-like oscillations in millimeterwave photoconductivity in a high-mobility two-dimensional electron gas. *Phys. Rev. B*, 64:201311(R), 2001.

[20] M. A. Zudov, I. V. Ponomarev, A. L. Efros, R. R. Du, J. A. Simmons, and J. L. Reno. New class of magnetoresistance oscillations: Interaction of a two-dimensional electron gas with leaky interface phonons. *Phys. Rev. Lett.*, 86:3614, 2001.

[21] C. L. Yang, J. Zhang, R. R. Du, J. A. Simmons, and J. L. Reno. Zener tunneling between landau orbits in a high-mobility two-dimensional electron gas. *Phys. Rev. Lett.*, 89:076801, 2002.

[22] K. J. Friedland, R Hey, H Kostial, R Klann, and K Ploog. New concept for the reduction of impurity scattering in remotely doped gaas quantum wells. *Phys. Rev. Lett.*, 77(22):4616, 1996.

[23] M. Sammon, M. A. Zudov, and B. I. Shklovskii. Mobility and quantum mobility of modern gaas/algaas heterostructures. *Phys. Rev. Materials*, 2:064604, Jun 2018. [ArXiv e-prints (2018), 1804.06936].

[24] A. L. Efros, F. G. Pikus, and G. G. Samsonidze. Maximum low-temperature mobility of two-dimensional electrons in heterojunctions with a thick spacer layer. *Phys. Rev. B*, 41(12):8295, 1990.

[25] R Grill and G. H. Döhler. Effect of charged donor correlation and wigner liquid formation on the transport properties of a two-dimensional electron gas in modulation δ-doped heterojunctions. *Phys. Rev. B*, 59(16):10769, 1999.

[26] S Das Sarma, E. H. Hwang, S Kodiyalam, L. N. Pfeiffer, and K. W. West. Transport in two-dimensional modulation-doped semiconductor structures. *Phys. Rev. B*, 91(20):205304, 2015.

[27] M Sammon, Tianran Chen, and B. I. Shklovskii. Excess electron screening of remote donors and mobility in modern gaas/algaas heterostructures. *Phys. Rev. Materials*, 2(10):104001, 2018.

[28] James A. Noland. Optical absorption of single-crystal strontium titanate. *Phys. Rev.*, 94:724–724, May 1954.

[29] A. Ohtomo and H. Y. Hwang. A high-mobility electron gas at the LaAlO3/SrTiO3 heterointerface. *Nature*, 427(6973):423–426, jan 2004.

[30] Yanwu Xie, Christopher Bell, Yasuyuki Hikita, Satoshi Harashima, and Harold Y. Hwang. Enhancing electron mobility at the laalo3/srtio3 interface by surface control. *Advanced Materials*, 25(34):4735–4738, 2013.

[31] Pouya Moetakef, Tyler A. Cain, Daniel G. Ouellette, Jack Y. Zhang, Dmitri O. Klenov, Anderson Janotti, Chris G. Van de Walle, Siddharth Rajan, S. James Allen, and Susanne Stemmer. Electrostatic carrier doping of gdtio3/srtio3 interfaces. *Applied Physics Letters*, 99(23):232116, 2011.

[32] Susanne Stemmer and S. James Allen. Two-dimensional electron gases at complex oxide interfaces. *Annual Review of Materials Research*, 44(1):151, 2014.

[33] C. He, T. D. Sanders, M. T. Gray, F. J. Wong, V. V. Mehta, and Y. Suzuki. Metal-insulator transitions in epitaxial $lavo_3$ and $latio_3$ films. *Phys. Rev. B*, 86:081401, Aug 2012.

[34] A. Annadi, A. Putra, Z. Q. Liu, X. Wang, K. Gopinadhan, Z. Huang, S. Dhar, T. Venkatesan, and Ariando. Electronic correlation and strain effects at the interfaces between polar and nonpolar complex oxides. *Phys. Rev. B*, 86:085450, Aug 2012.

[35] P. Perna, D. Maccariello, M. Radovic, U. Scotti di Uccio, I. Pallecchi, M. Codda, D. Marré, C. Cantoni, J. Gazquez, M. Varela, S. J. Pennycook, and F. Miletto Granozio. Conducting interfaces between band insulating oxides: The lagao3/srtio3 heterostructure. *Applied Physics Letters*, 97(15):152111, 2010.

[36] R. Ohtsuka, M. Matvejeff, K. Nishio, R. Takahashi, and M. Lippmaa. Transport properties of latio3/srtio3 heterostructures. *Applied Physics Letters*, 96(19):192111, 2010.

[37] S. Thiel, G. Hammerl, A. Schmehl, C. W. Schneider, and J. Mannhart. Tunable quasi-two-dimensional electron gases in oxide heterostructures. *Science*, 313(5795):1942–1945, 2006.

[38] Masayuki Hosoda, Christopher Bell, Yasuyuki Hikita, and Harold Y. Hwang. Compositional and gate tuning of the interfacial conductivity in laalo3/latio3/srtio3 heterostructures. *Applied Physics Letters*, 102(9):–, 2013.

[39] M. Boucherit, O. Shoron, C. A. Jackson, T. A. Cain, M. L. C. Buffon, C. Polchinski, S. Stemmer, and S. Rajan. Modulation of over 10^14 $cm^{-}2$ electrons in srtio3/gdtio3 heterostructures. *Applied Physics Letters*, 104(18):182904, 2014.

[40] K. Ueno, S. Nakamura, H. Shimotani, A. Ohtomo, N. Kimura, T. Nojima, H. Aoki, Y. Iwasa, and M. Kawasaki. Electric-field-induced superconductivity in an insulator. *Nat Mater*, 7(11):855–858, nov 2008.

[41] Patrick Gallagher, Menyoung Lee, James R. Williams, and David Goldhaber-Gordon. Gate-tunable superconducting weak link and quantum point contact spectroscopy on a strontium titanate surface. *Nature Physics*, 10(10):748–752, aug 2014.

[42] K. V. Reich, M. Schecter, and B. I. Shklovskii. Accumulation, inversion, and depletion layers in $srtio_3$. *Phys. Rev. B*, 91:115303, 2015.

[43] V.L. Ginzburg. On the dielectric properties of ferroelectric crystals and barium titanate. *J. Phys. USSR*, 10:107, 1946.

[44] L. D. Landau and E. M. Lifshitz. *Statistical Physics (Part 1)*, volume 5 of *Course of Theoretical Physics*. Butterworth-Heinemann, Kidlington, Oxford, 1980.

[45] L. H. Thomas. The calculation of atomic fields. *Mathematical Proceedings of the Cambridge Philosophical Society*, 23:542–548, 1 1927.

[46] Han Fu, KV Reich, and BI Shklovskii. Anomalous conductivity, hall factor, magnetoresistance, and thermopower of accumulation layer in srtio 3. *Physical Review B*, 94(4):045310, 2016.

[47] Michael Sammon, Han Fu, and B. I. Shklovskii. Anomalous thermodynamic properties of the electron accumulation layer in srtio 3. *Phys. Rev. B*, 96(15):155203, 2017.

[48] M Sammon, Han Fu, and B. I. Shklovskii. Electron accumulation layer in ultrastrong magnetic field. *Low Temperature Physics*, 43(2):232–238, 2017.

[49] J Frenkel. Über die elektrische oberflächenschicht der metalle. *Zeitschrift für Physik*, 51(3-4):232–238, 1928.

[50] Charles M Lieber. Nanoscale science and technology: building a big future from small things. *MRS bulletin*, 28(07):486–491, 2003.

[51] Peidong Yang. The chemistry and physics of semiconductor nanowires. *MRS bulletin*, 30(02):85–91, 2005.

[52] RM Lutchyn, EPAM Bakkers, Leo P Kouwenhoven, P Krogstrup, CM Marcus, and Y Oreg. Majorana zero modes in superconductor–semiconductor heterostructures. *Nature Reviews Materials*, 3(5):52, 2018.

[53] L. Hofstetter, S. Csonka, J. Nygard, and C. Schonenberger. Cooper pair splitter realized in a two-quantum-dot y-junction. *Nature*, 461:960–963, 2009.

[54] Yong-Joo Doh, Jorden A. van Dam, Aarnoud L. Roest, Erik P. A. M. Bakkers, Leo P. Kouwenhoven, and Silvano De Franceschi. Tunable supercurrent through semiconductor nanowires. *Science*, 309(5732):272–275, 2005.

[55] S. Nadj-Perge, S. M. Frolov, E. P. A. M. Bakkers, and L. P. Kouwenhoven. Spin-orbit qubit in a semiconductor nanowire. *Nature*, 468:1084, 2010.

[56] Elham MT Fadaly, Hao Zhang, Sonia Conesa-Boj, Diana Car, Önder Gül, Sébastien R Plissard, Roy LM Veld, Sebastian Kölling, Leo P Kouwenhoven, and Erik PAM Bakkers. Observation of conductance quantization in insb nanowire networks. *Nano letters*, 17(11):6511–6515, 2017.

[57] Roman M. Lutchyn, Jay D. Sau, and S. Das Sarma. Majorana fermions and a topological phase transition in semiconductor-superconductor heterostructures. *Phys. Rev. Lett.*, 105:077001, Aug 2010.

[58] Yuval Oreg, Gil Refael, and Felix von Oppen. Helical liquids and majorana bound states in quantum wires. *Phys. Rev. Lett.*, 105:177002, Oct 2010.

[59] Ettore Majorana. Teoria simmetrica dell'elettrone e del positrone. *Il Nuovo Cimento (1924-1942)*, 14(4):171, 2008.

[60] V. Mourik, K. Zuo, S. M. Frolov, S. R. Plissard, E. P. A. M. Bakkers, and L. P. Kouwenhoven. Signatures of majorana fermions in hybrid superconductor-semiconductor nanowire devices. *Science*, 336(6084):1003–1007, 2012.

[61] M. T. Deng, C. L. Yu, G. Y. Huang, M. Larsson, P. Caroff, and H. Q. Xu. Anomalous zero-bias conductance peak in a nb-insb nanowire-nb hybrid device. *Nano Letters*, 12(12):6414–6419, 2012.

[62] H. O. H. Churchill, V. Fatemi, K. Grove-Rasmussen, M. T. Deng, P. Caroff, H. Q. Xu, and C. M. Marcus. Superconductor-nanowire devices from tunneling to the multichannel regime: Zero-bias oscillations and magnetoconductance crossover. *Phys. Rev. B*, 87:241401, Jun 2013.

[63] Jay D. Sau, Sumanta Tewari, and S. Das Sarma. Experimental and materials considerations for the topological superconducting state in electron- and hole-doped semiconductors: Searching for non-abelian majorana modes in 1d nanowires and 2d heterostructures. *Phys. Rev. B*, 85:064512, Feb 2012.

[64] Önder Gül et al. Towards high mobility insb nanowire devices. *Nanotechnology*, 26(21):215202, 2015.

[65] Marc Scheffler, Stevan Nadj-Perge, Leo P. Kouwenhoven, Magnus T. Borgström, and Erik P. A. M. Bakkers. Diameter-dependent conductance of inas nanowires. *Journal of Applied Physics*, 106(12):124303, 2009.

[66] Jared J. Hou, Fengyun Wang, Ning Han, Haoshen Zhu, KitWa Fok, WaiChak Lam, SenPo Yip, TakFu Hung, Joshua E.-Y. Lee, and Johnny C. Ho. Diameter

dependence of electron mobility in ingaas nanowires. *Applied Physics Letters*, 102(9):093112, 2013.

[67] Alexandra C. Ford, Johnny C. Ho, Yu-Lun Chueh, Yu-Chih Tseng, Zhiyong Fan, Jing Guo, Jeffrey Bokor, and Ali Javey. Diameter-dependent electron mobility of inas nanowires. *Nano Letters*, 9(1):360–365, 2009.

[68] S. Poli, M. G. Pala, T. Poiroux, S. Deleonibus, and G. Baccarani. Size dependence of surface-roughness-limited mobility in silicon-nanowire fets. *IEEE Transactions on Electron Devices*, 55(11):2968–2976, Nov 2008.

[69] Jiezhi Chen, Takuya Saraya, Kousuke Miyaji, Ken Shimizu, and Toshiro Hiramoto. Experimental study of mobility in [110]- and [100]-directed multiple silicon nanowire gaa mosfets on (100) soi. In *2008 Symposium on VLSI Technology*, pages 32–33, June 2008.

[70] Fengyun Wang, SenPo Yip, Ning Han, KitWa Fok, Hao Lin, Jared J Hou, Guofa Dong, TakFu Hung, K S Chan, and Johnny C Ho. Surface roughness induced electron mobility degradation in inas nanowires. *Nanotechnology*, 24(37):375202, 2013.

[71] H. Akera and T. Ando. Magnetoresistance in quantum wires: Boundary-roughness scattering. *Phys. Rev. B*, 43:11676–11685, May 1991.

[72] Seonghoon Jin, Massimo V. Fischetti, and Ting wei Tang. Modeling of electron mobility in gated silicon nanowires at room temperature: Surface roughness scattering, dielectric screening, and band nonparabolicity. *Journal of Applied Physics*, 102(8):083715, 2007.

[73] J. Motohisa and H. Sakaki. Interface roughness scattering and electron mobility in quantum wires. *Applied Physics Letters*, 60(11):1315–1317, 1992.

[74] Han Fu, M. Sammon, and B. I. Shklovskii. Roughness scattering induced insulator-metal-insulator transition in a quantum wire. *Phys. Rev. B*, 97:035304, Jan 2018.

[75] Han Fu, K. V. Reich, and B. I. Shklovskii. Surface roughness scattering in multi-subband accumulation layers. *Phys. Rev. B*, 93:235312, Jun 2016.

[76] S Das Sarma and E. H. Hwang. Universal density scaling of disorder-limited low-temperature conductivity in high-mobility two-dimensional systems. *Phys. Rev. B*, 88(3):035439, 2013.

[77] CL Kane and Matthew PA Fisher. Transport in a one-channel luttinger liquid. *Physical Review Letters*, 68(8):1220, 1992.

[78] Matthew PA Fisher and Leonid I Glazman. Transport in a one-dimensional luttinger liquid. In *Mesoscopic Electron Transport*, pages 331–373. Springer, 1997.

[79] K. S. Novoselov, A. K. Geim, S. V. Morozov, D. Jiang, Y. Zhang, S. V. Dubonos, I. V. Grigorieva, and A. A. Firsov. Electric field effect in atomically thin carbon films. *Science*, 306(5696):666–669, 2004, https://science.sciencemag.org/content/306/5696/666.full.pdf.

[80] Kin Fai Mak, Changgu Lee, James Hone, Jie Shan, and Tony F Heinz. Atomically thin mos_2: a new direct-gap semiconductor. *Phys. Rev, Lett.*, 105(13):136805, 2010.

[81] Kin Fai Mak, Keliang He, Changgu Lee, Gwan Hyoung Lee, James Hone, Tony F Heinz, and Jie Shan. Tightly bound trions in monolayer mos_2. *Nature materials*, 12(3):207, 2013.

[82] Kin Fai Mak, Kathryn L McGill, Jiwoong Park, and Paul L McEuen. The valley hall effect in mos_2 transistors. *Science*, 344(6191):1489–1492, 2014.

[83] Pasqual Rivera, Kyle L Seyler, Hongyi Yu, John R Schaibley, Jiaqiang Yan, David G Mandrus, Wang Yao, and Xiaodong Xu. Valley-polarized exciton dynamics in a 2d semiconductor heterostructure. *Science*, 351(6274):688–691, 2016.

[84] Sajedeh Manzeli, Dmitry Ovchinnikov, Diego Pasquier, Oleg V Yazyev, and Andras Kis. 2d transition metal dichalcogenides. *Nature Reviews Materials*, 2(8):17033, 2017.

[85] Manish Chhowalla, Zhongfan Liu, and Hua Zhang. Two-dimensional transition metal dichalcogenide (tmd) nanosheets. *Chemical Society Reviews*, 44(9):2584–2586, 2015.

[86] Maurizia Palummo, Marco Bernardi, and Jeffrey C Grossman. Exciton radiative lifetimes in two-dimensional transition metal dichalcogenides. *Nano letters*, 15(5):2794–2800, 2015.

[87] Gang Wang, Alexey Chernikov, Mikhail M Glazov, Tony F Heinz, Xavier Marie, Thierry Amand, and Bernhard Urbaszek. Colloquium: Excitons in atomically thin transition metal dichalcogenides. *Rev. Mod. Phys.*, 90(2):021001, 2018.

[88] Pasqual Rivera, John R Schaibley, Aaron M Jones, Jason S Ross, Sanfeng Wu, Grant Aivazian, Philip Klement, Kyle Seyler, Genevieve Clark, Nirmal J Ghimire, Jiaqiang Yan, D. G. Mandrus, and Xiaodong Xu. Observation of long-lived interlayer excitons in monolayer $mose_2$–wse_2 heterostructures. *Nat. Comm.*, 6:6242, 2015.

[89] E. V. Calman, L. H. Fowler-Gerace, L. V. Butov, D. E. Nikonov, I. A. Young, S. Hu, A. Mischenko, and A. K. Geim. Localized bright luminescence of indirect excitons and trions in $mose_2/wse_2$ van der waals heterostructure. *arXiv e-prints*, page arXiv:1901.08664, January 2019.

[90] M. M. Fogler, L. V. Butov, and K. S. Novoselov. High-temperature superfluidity with indirect excitons in van der waals heterostructures. *Nat. Comm.*, 5:4555, 2014.

[91] Jason S Ross, Sanfeng Wu, Hongyi Yu, Nirmal J Ghimire, Aaron M Jones, Grant Aivazian, Jiaqiang Yan, David G Mandrus, Di Xiao, Wang Yao, et al. Electrical control of neutral and charged excitons in a monolayer semiconductor. *Nature communications*, 4:1474, 2013.

[92] M. Sammon and B. I. Shklovskii. Attraction of indirect excitons in van der waals heterostructures with three semiconducting layers. *Phys. Rev. B*, 99:165403, Apr 2019.

[93] Toshio Baba, Takashi Mizutani, and Masaki Ogawa. Elimination of persistent photoconductivity and improvement in si activation coefficient by al spatial separation from ga and si in al–ga–as: Si solid system–a novel short period alas/n-gaas superlattice–. *Jpn. J. Appl. Phys.*, 22(10A):L627, 1983.

[94] K. B. Cooper, M. P. Lilly, J. P. Eisenstein, T. Jungwirth, L. N. Pfeiffer, and K. W. West. An investigation of orientational symmetry-breaking mechanisms in high landau levels. *Solid State Commun.*, 119:89, 2001.

[95] J. P. Eisenstein, K. B. Cooper, L. N. Pfeiffer, and K. W. West. Insulating and fractional quantum hall states in the first excited landau level. *Phys. Rev. Lett.*, 88:076801, Jan 2002.

[96] R. R. Du, H. L. Stormer, D. C. Tsui, L. N. Pfeiffer, and K. W. West. Experimental evidence for new particles in the fractional quantum hall effect. *Phys. Rev. Lett.*, 70:2944–2947, May 1993.

[97] L. N. Pfeiffer, private communication (2018).

[98] J Ihm. Effects of the layer thickness on the electronic character in gaas-alas superlattices. *Appl. Phys. Lett.*, 50(16):1068–1070, 1987.

[99] A. R. Khisameeva, A. V. Shchepetilnikov, V. M. Muravev, S. I. Gubarev, D. D. Frolov, Yu. A. Nefyodov, I. V. Kukushkin, C. Reichl, L. Tiemann, W. Dietsche, and W. Wegsheider. Direct observation of a γ- x energy spectrum transition in narrow alas quantum wells. *Physical Review B*, 97(11):115308, 2018.

[100] I Vurgaftman, J. R. Meyer, and L. R. Ram-Mohan. Band parameters for iii–v compound semiconductors and their alloys. *J. Appl. Phys.*, 89(11):5815–5875, 2001.

[101] A. B. Fowler and A. Hartstein. Impurity bands in inversion layers. *Philos. Mag. B*, 42(6):949–959, 1980.

[102] S. I. Dorozhkin, D. V. Sychev, and A. A. Kapustin. Bolometric detection of magnetoplasma resonances in microwave absorption by two-dimensional electron systems based on doping layer conductivity measurements in gaas/algaas heterostructures. *J. Appl. Phys.*, 116(20):203702, 2014.

[103] S. I. Dorozhkin, V. Umansky, K. von Klitzing, and J. H. Smet. Dynamics of spontaneous electric field domains in a two-dimensional electron system irradiated

by microwaves and the conductance of a donor layer. *JETP Lett.*, 107(1):61–65, Jan 2018.

[104] M. S. Bello, E. I. Levin, B. I. Shklovskii, and A. L. Efros. Density of localized states in the surface impurity band of a metal–insulator–semiconductor structure. *Zh. Eksp. Teor. Fiz,*, 80:1596, 1981. [Sov. Phys. JETP **53**, 822 (1981)].

[105] Q. Shi, M. A. Zudov, I. A. Dmitriev, K. W. Baldwin, L. N. Pfeiffer, and K. W. West. Fine structure of high-power microwave-induced resistance oscillations. *Phys. Rev. B*, 95:041403, Jan 2017.

[106] S. J. MacLeod, K Chan, T. P. Martin, A. R. Hamilton, A See, A. P. Micolich, M Aagesen, and P. E. Lindelof. Role of background impurities in the single-particle relaxation lifetime of a two-dimensional electron gas. *Phys. Rev. B*, 80(3):035310, 2009.

[107] A Gold. Scattering time and single-particle relaxation time in a disordered two-dimensional electron gas. *Phys. Rev. B*, 38(15):10798, 1988.

[108] I. A. Dmitriev, A. D. Mirlin, D. G. Polyakov, and M. A. Zudov. Nonequilibrium phenomena in high landau levels. *Rev. Mod. Phys.*, 84:1709, Nov 2012.

[109] M. A. Zudov, I. A. Dmitriev, B Friess, Q Shi, V Umansky, K Von Klitzing, and J Smet. Hall field-induced resistance oscillations in a tunable-density gaas quantum well. *Phys. Rev. B*, 96(12):121301, 2017.

[110] A Gold. Electronic transport properties of a two-dimensional electron gas in a silicon quantum-well structure at low temperature. *Phys. Rev. B*, 35(2):723, 1987.

[111] J. Nuebler, V. Umansky, R. Morf, M. Heiblum, K. von Klitzing, and J. Smet. Density dependence of the $\nu = \frac{5}{2}$ energy gap: Experiment and theory. *Phys. Rev. B*, 81:035316, Jan 2010.

[112] N d'Ambrumenil, B. I. Halperin, and R. H. Morf. Model for dissipative conductance in fractional quantum hall states. *Phys. Rev. Lett.*, 106(12):126804, 2011.

[113] D. G. Polyakov and B. I. Shklovskii. Universal prefactor of activated conductivity in the quantum hall effect. *Phys. Rev. Letters*, 74(1):150, 1995.

[114] A. L. Efros. Non-linear screening and the background density of 2deg states in magnetic field. *Solid State Commun.*, 67(11):1019–1022, 1988.

[115] F. G. Pikus and A. L. Efros. Distribution of electron density and magnetocapacitance in the regime of the fractional quantum hall effect. *Phys. Rev. B*, 47:16395–16403, Jun 1993.

[116] Han Fu, KV Reich, and BI Shklovskii. Electron gas induced in srtio3. *Journal of Experimental and Theoretical Physics*, 122(3):456–471, 2016.

[117] Lu Li, C Richter, S Paetel, T Kopp, J Mannhart, and RC Ashoori. Very large capacitance enhancement in a two-dimensional electron system. *Science*, 332(6031):825–828, 2011.

[118] V Tinkl, M Breitschaft, C Richter, and J Mannhart. Large negative electronic compressibility of laalo 3-srtio 3 interfaces with ultrathin laalo 3 layers. *Physical Review B*, 86(7):075116, 2012.

[119] D. van der Marel, J. van Mechelen, and I. Mazin. Common fermi-liquid origin of T^2 resistivity and superconductivity in n-type $srtio_3$. *Phys. Rev. B*, 84:205111, Nov 2011.

[120] AD Caviglia, M Gabay, Stefano Gariglio, Nicolas Reyren, Claudia Cancellieri, and J-M Triscone. Tunable rashba spin-orbit interaction at oxide interfaces. *Physical review letters*, 104(12):126803, 2010.

[121] A Spinelli, MA Torija, C Liu, C Jan, and C Leighton. Electronic transport in doped srtio 3: Conduction mechanisms and potential applications. *Physical Review B*, 81(15):155110, 2010.

[122] V. Celli and N. David Mermin. Ground state of an electron gas in a magnetic field. *Phys. Rev.*, 140:A839–A853, Nov 1965.

[123] J. I. Kaplan and M. L. Glasser. Electron gas in superstrong magnetic fields: Wigner transition. *Phys. Rev. Lett.*, 28:1077–1079, Apr 1972.

[124] W G Kleppmann and R J Elliott. The wigner transition in a magnetic field. *Journal of Physics C: Solid State Physics*, 8(17):2729, 1975.

[125] Bertrand I Halperin. Possible states for a three-dimensional electron gas in a strong magnetic field. *Japanese Journal of Applied Physics*, 26(S3-3):1913, 1987.

[126] R A Cowley. Lattice dynamics and phase transitions of strontium titanate. *Physical Review*, 134(4A):A981, 1964.

[127] John H Barrett. Dielectric constant in perovskite type crystals. *Physical Review*, 86(1):118, 1952.

[128] Junwoo Son, Pouya Moetakef, Bharat Jalan, Oliver Bierwagen, Nicholas J Wright, Roman Engel-Herbert, and Susanne Stemmer. Epitaxial srtio3 films with electron mobilities exceeding 30,000 $cm^2v^{-1}s^{-1}$. *Nature materials*, 9(6):482–484, 2010.

[129] S James Allen, Bharat Jalan, SungBin Lee, Daniel G Ouellette, Guru Khalsa, Jan Jaroszynski, Susanne Stemmer, and Allan H MacDonald. Conduction-band edge and shubnikov–de haas effect in low-electron-density srtio 3. *Physical Review B*, 88(4):045114, 2013.

[130] Y Kozuka, T Susaki, and H Y Hwang. Vanishing hall coefficient in the extreme quantum limit in photocarrier-doped srtio 3. *Physical review letters*, 101(9):096601, 2008.

[131] Anand Bhattacharya, Brian Skinner, Guru Khalsa, and Alexey V Suslov. Spatially inhomogeneous electron state deep in the extreme quantum limit of strontium titanate. *Nature communications*, 7:12974, 2016.

[132] K Ueno, S Nakamura, H Shimotani, A Ohtomo, N Kimura, T Nojima, H Aoki, Y Iwasa, and M Kawasaki. Electric-field-induced superconductivity in an insulator. *Nature materials*, 7(11):855–858, 2008.

[133] Bharat Jalan, Susanne Stemmer, Shawn Mack, and S James Allen. Two-dimensional electron gas in δ-doped srtio 3. *Physical Review B*, 82(8):081103, 2010.

[134] Felix Trier, Guenevere E. D. K. Prawiroatmodjo, Zhicheng Zhong, Dennis Valbjørn Christensen, Merlin von Soosten, Arghya Bhowmik, Juan Maria García Lastra, Yunzhong Chen, Thomas Sand Jespersen, and Nini Pryds.

Quantization of hall resistance at the metallic interface between an oxide insulator and srtio$_3$. *Phys. Rev. Lett.*, 117:096804, Aug 2016.

[135] Y Matsubara, K S Takahashi, M S Bahramy, Y Kozuka, D Maryenko, J Falson, A Tsukazaki, Y Tokura, and M Kawasaki. Observation of the quantum hall effect in [delta]-doped srtio3. *Nature communications*, 7, 2016.

[136] Frank Stern and W E Howard. Properties of semiconductor surface inversion layers in the electric quantum limit. *Physical Review*, 163(3):816, 1967.

[137] Frank Stern. Self-consistent results for n-type si inversion layers. *Physical Review B*, 5(12):4891, 1972.

[138] Norman J Horing. Quantum theory of static shielding of an impurity charge by an electron gas plasma in a magnetic field. *Annals of Physics*, 54(3):405–429, 1969.

[139] B I Shklovskii and A L Efros. The electron localization in magnetic fields. *Sov. Phys, JETP*, 64:2222–2231, 1973.

[140] V V Kosarev, N A Red'Ko, and I Belitskii. Electron localization by a strong magnetic field in n-insb. *Sov. Phys, JETP*, 73:270, 1991.

[141] S S Murzin, A G M Jansen, and E G Haanappel. Quasi-one-dimensional transport in the extreme quantum limit of heavily doped n- insb. *Physical Review B*, 62(24):16645, 2000.

[142] Brian Skinner and B. I. Shklovskii. Anomalously large capacitance of a plane capacitor with a two-dimensional electron gas. *Phys. Rev. B*, 82(15):155111, 2010.

[143] Mikhail A Liberman and B Johansson. Properties of matter in ultrahigh magnetic fields and the structure of the surface of neutron stars. *Physics-Uspekhi*, 38(2):117, 1995.

[144] Finley R Shapiro and David Adler. Equilibrium transport in amorphous semiconductors. *Journal of non-crystalline solids*, 74(2-3):189–194, 1985.

[145] B B Kadomtsev. Heavy atom in an ultrastrong magnetic field. *Zh. Eksp. Teor. Fiz.*, 58:1765–1769, 1970.

[146] B B Kadomtsev and V S Kudryavtsev. Atoms in a superstrong magnetic field. *JETP Lett.*, 13:42–44, 1971.

[147] H Sakaki, T Noda, K Hirakawa, M Tanaka, and T Matsusue. Interface roughness scattering in gaas/alas quantum wells. *Appl. Phys. Lett.*, 51(23):1934–1936, 1987.

[148] E. M. Baskin and M. V. Entin. *Fiz. Tekh, Poluprovodn.*, 8:64, 1974.

[149] M.V. Krylov and R.A. Suris. Mobility of carriers in inversion layers in semiconductors. *JETP*, 56(6):1316, 1982.

[150] S. M. Goodnick, D. K. Ferry, C. W. Wilmsen, Z. Liliental, D. Fathy, and O. L. Krivanek. Surface roughness at the si(100)-sio$_2$ interface. *Phys. Rev. B*, 32:8171–8186, Dec 1985.

[151] R. M. Feenstra, D. A. Collins, D. Z. Y. Ting, M. W. Wang, and T. C. McGill. Interface roughness and asymmetry in inas/gasb superlattices studied by scanning tunneling microscopy. *Phys. Rev. Lett.*, 72:2749–2752, Apr 1994.

[152] LI Glazman, IM Ruzin, and BI Shklovskii. Quantum transport and pinning of a one-dimensional wigner crystal. *Physical Review B*, 45(15):8454, 1992.

[153] K. V. Reich, M. Schecter, and B. I. Shklovskii. Accumulation, inversion, and depletion layers in srtio$_3$. *Phys. Rev. B*, 91:115303, Mar 2015.

[154] Eric D. Siggia and P. C. Kwok. Properties of electrons in semiconductor inversion layers with many occupied electric subbands. i. screening and impurity scattering. *Phys. Rev. B*, 2:1024–1036, Aug 1970.

[155] Henri J. Suominen et al. Scalable majorana devices. *arXiv:1703.03699*, 2017.

[156] Sneha G Pandya and Martin E Kordesch. Characterization of insb nanoparticles synthesized using inert gas condensation. *Nanoscale research letters*, 10(1):258, 2015.

[157] Lu Li, Christoph Richter, S Paetel, Thilo Kopp, Jochen Mannhart, and R. C. Ashoori. Very large capacitance enhancement in a two-dimensional electron system. *Science*, 332(6031):825–828, 2011.

[158] Brian Skinner and B. I. Shklovskii. Giant capacitance of a plane capacitor with a two-dimensional electron gas in a magnetic field. *Phys. Rev. B*, 87(3):035409, 2013.

[159] Brian Skinner, G. L. Yu, A. V. Kretinin, A. K. Geim, K. S. Novoselov, and B. I. Shklovskii. Effect of dielectric response on the quantum capacitance of graphene in a strong magnetic field. *Phys. Rev. B*, 88:155417, Oct 2013.

[160] Tianran Chen, Brian Skinner, and B. I. Shklovskii. Cooperative charging in a nanocrystal assembly gated by ionic liquid. *Phys. Rev. B*, 84:245304, Dec 2011.

[161] S De Palo, F Rapisarda, and Gaetano Senatore. Excitonic condensation in a symmetric electron-hole bilayer. *Phys. Rev. Lett.*, 88(20):206401, 2002.

[162] Jens Schleede, Alexey Filinov, Michael Bonitz, and Holger Fehske. Phase diagram of bilayer electron-hole plasmas. *Contributions to Plasma Physics*, 52(10):819–826, 2012.

[163] Ryo Maezono, Pablo López Ríos, Tetsuo Ogawa, and Richard J. Needs. Excitons and biexcitons in symmetric electron-hole bilayers. *Phys. Rev. Lett.*, 110:216407, May 2013.

[164] Michal Baranowski, Alessandro Surrente, L Klopotowski, J. M. Urban, Nan Zhang, Duncan K Maude, Kamil Wiwatowski, Sebastian Mackowski, Yen-Cheng Kung, Dumitru Dumcenco, A. Kis, and P. Plochocka. Probing the interlayer exciton physics in a mos2/mose2/mos2 van der waals heterostructure. *Nano letters*, 17(10):6360–6365, 2017.

[165] Chanyeol Choi, Jiahui Huang, Hung-Chieh Cheng, Hyunseok Kim, Abhinav Kumar Vinod, Sang-Hoon Bae, V Ongun Özçelik, Roberto Grassi, Jongjae Chae, Shu-Wei Huang, et al. Enhanced interlayer neutral excitons and trions in trilayer van der waals heterostructures. *npj 2D Mater. Appl.*, 2(1):30, 2018.

[166] L. V. Keldysh and A. N. Kozlov. Collective properties of excitons in semiconductors. *Sov. Phys. JETP*, 27(3):521, 1968.

[167] Akash Laturia, Maarten L Van de Put, and William G Vandenberghe. Dielectric properties of hexagonal boron nitride and transition metal dichalcogenides: from monolayer to bulk. *npj 2D Mater. Appl.*, 2(1):6, 2018.

Appendix A

Acronyms

This appendix provides a summary of the most common acronyms that are used in the thesis.

A.1 Acronyms

Table A.1: Acronyms

Acronym	Meaning
1D	One-Dimensional
1DEG	One-Dimensional Electron Gas
2D	Two-Dimensional
2DEG	Two-Dimensional Electron Gas
3D	Three-Dimensional
BI	Background Impurities
DFR	Distribution Function Ratio
EE	Excess Electrons
EES	Excess Electron Screening
EQL	Extreme Quantum Limit
GTO	$GdTiO_3$

Continued on next page

Table A.1 – continued from previous page

Acronym	Meaning
hBN	Hexagonal Boron Nitride
LSAT	$(LaAlO_3)_{0.3}(Sr_2AlTaO_6)_{0.7}$
M	Quasi-Classical Metal
MIT	Metal-Insulator Transition
RAT	Run-away Tail
RI	Remote Impurities
RPA	Random Phase Approximation
SPSL	Short-Period Superlattice
STO	$SrTiO_3$
TF	Thomas-Fermi
TMD	Transition Metal Dichalcogenide
VRM	Variable Radius Model
WC	Wigner Crystal